Heterogeneous Integration of Colloidal Quantum Dots with Silicon Nitride Nanophotonics

David Sharp

A dissertation

submitted in partial fulfillment of

requirements for the degree of

Doctor of Philosophy

University of Washington

2025

Reading Committee:

Arka Majumdar, Chair

Xiaodong Xu

Igor Novosselov

Program Authorized to Offer Degree:
Physics

University of Washington

Abstract

Heterogeneous Integration of Colloidal Quantum Dots with Silicon Nitride Nanophotonics

David Sharp

Chair of the Supervisory Committee:

Arka Majumdar

Departments of Physics and Electrical & Computer Engineering

Integrated photonics is a promising platform for next-generation technologies ranging from the classical to the quantum. Conventional photonic integrated circuits are fabricated from silicon and silicon compounds that, while excellent for passive components, are ill-suited for most active applications. A solution to this problem is the heterogeneous integration of novel materials with existing photonic devices fabricated from conventional photonic materials. In this thesis, I specifically focus on the heterogeneous integration of colloidal quantum dots with silicon nitride nanophotonics including techniques thereof. I will discuss my collaborative work on integration techniques such as inkjet printing of colloidal quantum dot ensembles and singles as well as template assisted self-assembly of single colloidal quantum dot arrays. I will also cover my work on on-chip nanolasers using colloidal quantum wells, in addition to cavity-enhanced second-harmonic generation from colloidal quantum dots. Lastly, I will discuss my work on near-visible topological edge states in silicon nitride, which paves the way for integration with colloidal

quantum dots. This thesis is a step forward in the work of functionalizing passive photonic devices with colloidal quantum dots.

Acknowledgements

To start, I would like to extend my deepest thanks to Arka Majumdar. His tenacity and optimism that experiments would work, results were publishable, and there is always a path forward (despite my usual pessimism) were huge sources of motivation for me. He has been a wonderful mentor and facilitated my growth as a scientist, and I am proud of his consistent desire to improve as an investigator and teacher. Of course, my PhD would be nothing without the support of my fellow NOISE Lab researchers. Johannes Fröch, Jie Fang, Abhinav Kala, and Minho Choi were all amazing postdocs who taught me many skills and how to approach research intelligently. Chris Munley, Hannah Rarick, Arnab Manna, Abhi Saxena, David Rosser, Andrew Tang, and Aurelia Brook were there to commiserate in the PhD struggles (and solve crosswords at lunch), keeping me sane during the bleak middle years of the PhD. To my other friends in the Physics PhD program Heather, Sam, Mia, Robert, and Tharindu: I am so grateful that I met all of you, and I look forward to lifelong friendships with each of you. I would also like to thank my family for always supporting me throughout my education and fostering my curiosity. Lastly, I give my love to my partner Emma, who supported me through the entirety of this journey and has been an unwavering pillar of support. She has been very patient with me complaining about research, and her advice has been invaluable. I would not be where I am today without her.

Table of Contents

Table of Figures iii

Chapter 1 Introduction 1

1.1 Motivation 1

1.2 Colloidal Quantum Dots 2

1.3 Nanobeam Photonic Crystal Cavities 3

1.4 The Purcell Effect 5

1.5 Thesis Outline 7

Chapter 2 Deterministic Positioning of Colloidal Quantum Dots 9

2.1 Inkjet Printing Colloidal Quantum Dot Ensembles on Monolithic Nanobeam Cavities 9

2.2 Inkjet Printing Colloidal Quantum Dot Ensembles on Suspended Nanobeam Cavities 16

2.3 Template-Assisted Self-Assembly of Single Colloidal Quantum Dot Arrays 22

2.4 Inkjet Printing Single Colloidal Quantum Dots on Nanobeam Cavities 30

Chapter 3 On-Chip Nanolasers Using Colloidal Emitters 38

3.1 Visible Nanolaser Using Deterministically Integrated Colloidal Quantum Wells 38

3.2 Continuous-wave Infrared Nanolaser Using PbS QDs on a Silicon Nanobeam 47

Chapter 4 Nanocavity-Enhanced Colloidal Quantum Dot Second-Harmonic Generation 56

Chapter 5 Near-Visible Topological Edge States in a Silicon Nitride Platform 62

Chapter 6 Outlook 73

Bibliography 74

Table of Figures

Figure 1.1 (a) Scanning electron micrograph (SEM) of a typical nanobeam cavity. (b) Finite-difference time-domain simulation of a typical cavity mode. The scale bar is 1 μm. (c) Calculation of a typical nanobeam band structure including that for the inner and outer unit cells. 4

Figure 2.1 (a) Scheme describing the EHDIJ printing setup. A computer-controlled AC source creates an alternating voltage profile between the print nozzle and the printer bed via a small electrode embedded in the print nozzle. This voltage generates an electric field between the print nozzle and the print substrate that drives printing. Inset: diagram showing the effect of an electric field on the meniscus at the tip of an EHDIJ print nozzle. Partial polarization of the NC ink overcomes the ink's surface energy and draws a convex Taylor cone out of the EHDIJ nozzle to produce small droplets that form the final print pattern. PL microscope images of printed $CsPbBr_3$ NCs on a fluorinated SAM-treated silicon substrate with (b) 2 μm feature spacing and (c) 20 μm feature spacing 12

Figure 2.2 (a) Normalized PL spectra of $CsPbBr_3$ NCs drop-cast from hexanes solvent and EHDIJ printed on a silicon substrate. Inset: photograph of printed patterns on a glass substrate, under 450 nm illumination. The 1 mm^2 print patterns visible here have different brightnesses because they were printed with different parameters and different numbers of print passes. AFM images of NCs printed with 20 μm feature spacing and bump hold times of (b) 40 ms and (c) 70 ms. (d) AFM image of NCs printed with 2 μm feature spacing. (e) Height profiles from the color-coded lines in the AFM images in panels (b)–(d) showing controllable, sub-micrometer NC feature sizes. 13

Figure 2.3 (a) PL microscope image of EHDIJ printed CsPbBr3 NCs on an array of prefabricated monolithic Si3N4 nanobeam cavities. NC features were printed with 50 μm spacing, and several off-target features are present. Visible PL can be seen emanating from the grating couplers at the top and bottom of each cavity. (b) PL spectra collected through a nanobeam cavity grating coupler. In addition to broad background CsPbBr3 NC emission, a sharp peak is observed at ∼517 nm, associated with NC PL coupled to the nanobeam cavity mode (Q ~ 1000). Inset: PL microscope image of the nanobeam cavity characterized in (b). The scale bar is 10 μm. 15

Figure 2.4 (a) Normalized absorption and PL spectra of CdSe/CdS quantum dots. Inset: Image comparison of the colloidal QD ink under ambient and ultra-violet (UV) lighting conditions. (b) PL characterization of 500 nm separated suspended Si_3N_4 cavity. Inset: SEM imagery of the respective fabricated device. The presence of a single mode peak at ∼625 nm indicates no coupling at this distance.

(c) PL characterization of 100 nm separated suspended Si_3N_4 cavity. The two peaks between 620 nm and 630 are assigned to two cavity supermodes, which indicates that these cavities are strongly coupled at this distance. Inset: SEM micrographs of the respective fabricated devices. 17

Figure 2.5 Schematic of the electrohydrodynamic inkjet printing setup used in this work. The inset image shows PL microscopy with 450 nm excitation of CdSe/CdS quantum dots printed with 2 μm pitch. 18

Figure 2.6 SEM imagery of suspended cavity beam pairs post-EHDIJ printing. The micrographs show an aggregation of CdSe/CdS printed on a single beam for each pair. (a) 500 nm beam separation. i. Device overview image. ii. Cavity print site image. (b) 200 nm beam separation. i. Device overview image. ii. Cavity print site image. (c) 100 nm beam separation. i. Device overview image. ii. Cavity print site image. 19

Figure 2.7 PL microscopy and characterization of asymmetrically printed QD-coupled suspended cavity pairs. (a) PL spectra of 500 nm separated suspended nanobeam cavities. Inset: PL imagery of the respective cavity. (b) PL spectra of 200 nm separated suspended cavities. Inset: PL imagery of the respective cavities. (c) PL spectra of 100 nm separated suspended cavities. Inset: PL imagery of the respective cavities. (d) PL lifetime measurements of QDs printed on the cavity site and outside of the cavity. The QD's dashed blue line represents the best-fit bi-exponential to the mean of the raw data (black) for the external QDs, accompanied by a shaded curve (gray) to represent the standard deviation of the fit. The cavity's dashed red line represents the fitted biexponential curve of the data (black) for the cavity-coupled QDs. 20

Figure 2.8 Characterization of the synthesized QDs including (a) photoluminescence (solid curves) and UV–visible absorption spectra (dotted curves), (b) TEM images of CdSe/CdS QDs, and (c) $CdSe/CdS/SiO_2$ QDs. 25

Figure 2.9 Schematic process of the template-assisted self-assembly method to deterministically place silica (light blue sphere)-shelled QDs (red sphere) in an array using a PMMA template (yellow) on a Si/SiO_2 substrate (light blue)..... 26

Figure 2.10 (a) Schematic construction of one 9 × 24 array showing the assembly yield. (b) Plot showing the frequency of traps containing multiple, one, or no QDs as a function of trap diameter. SEM images of (c) sub arrays of QDs, (d) a single QD in a trap before the PMMA liftoff step, (e) a single QD in a templated position after the PMMA liftoff step, and (f) multiple QDs in a templated position after the

PMMA liftoff step. The contrast of the SEM images was adjusted after imaging to optimize visibility of particles and the array. 28

Figure 2.11 (a) Schematic construction of one 9 × 24 array showing the assembly yield. (b) Plot showing the frequency of traps containing multiple, one, or no QDs as a function of trap diameter. SEM images of (c) sub arrays of QDs, (d) a single QD in a trap before the PMMA liftoff step, (e) a single QD in a templated position after the PMMA liftoff step, and (f) multiple QDs in a templated position after the PMMA liftoff step. The contrast of the SEM images was adjusted after imaging to optimize visibility of particles and the array. 29

Figure 2.12 (a) Reported droplet sizes using conventional mechanical inkjet and EHDIJ printing over the past 35 years, along with the results of this work. (b) Schematic diagram of the EHDIJ printing setup used here. Top inset: fluorescence (FL) microscopy of EHDIJ printhead. Bottom inset: SEM of single EHDIJ-printed QD. (c) Graphic representation of CdSe QD cores (orange) with tunable range of hexagonal diamond CdS shell (yellow) diameters. (d) and (e), Bisected illustrations of EHDIJ printheads dielectrophoretically overcoming (d) surface tension to print droplets of particle ensembles and (e) interfacial forces to print singular particles..... 32

Figure 2.13 (a) Effect of drive amplitude on FL detected print yield as a heatmap of number of prints detected out of a 10 x 10 array of print attempt sites, per parameter configuration. (b) Histogram plot of QDs counted per print site for a 10 x 10 array (900 V and 2 s parameter configuration) of attempt sites, as determined by SEM and FL. Estimated QDs indicate QDs not detected via SEM but were positively-indicated by the FL microscopy (inset). The distribution of estimated QDs is based on the non-zero statistical prevalence QDs per print, per bin. (c) SEM image of 2 x 2 array of EHDIJ-printed single QDs. White circles indicate single QD positions. Inset: SEM image of single QD. (d) Plot of single QD emission spectrum (black) and Lorentzian fit (red). (e) Second-order time correlation plot (blue) and fit (red) of EHDIJ-printed QD showing single-photon emission, measured at room temperature, with 10 μW excitation (d and e). (f) Histogram plot of $g^{(2)}(0)$ measurements on EHD-printed single QDs (n = 11). ... 34

Figure 2.14 (a) Fluorescent microscopy of horseshoe-shaped cavity with single EHD-printed QD. (b) SEM image of the cavity region containing single QD. (c) Spectrum plot of cavity integrated QD, at 70 K, excited and measured from the top. Inset: Magnified spectrum (shaded) around the cavity mode. (d) Spectrum of the pure QD-coupled cavity mode PL to the grating (black) and Lorentzian fit (red) when exciting from the top, measured at room temperature with 10 μW excitation (C and D). (e) Power-dependent spectra of QD-coupled cavity at 8 K with the cavity mode region shaded (614 nm), excited and

measured from the top. (f), Power dependence of 597 nm (yellow), 617 nm (red), and 627 nm (blue) peak intensities at 8 K, with power-law fits (dashed lines). (g) Second-order time correlation plot (blue) and fit (red) of cavity-coupled QD, excited (10 μW) and measured from the top at room temperature. 36

Figure 3.1 (a) Absorption and PL spectra of CdSe/CdS cQWs. (b) Transmission electron micrograph of CdSe/CdS cQWs. The scale bar is 50 nm. (c) Scanning electron micrograph of an example SiN nanobeam cavity. The cavity region coupled to cQWs and the grating couplers for collecting cavity-coupled cQW photoluminescence are highlighted in green and yellow, respectively. The scale bar is 10 μm. 39

Figure 3.2 (a) The profile of the cavity mode electric field E_y from FDTD simulation. The scale bar is 500 nm. (b) Scanning electron micrograph of the nanobeam cavity defect region. The PMMA window is highlighted in green. The scale bar is 500 nm. (c) Nanobeam cavity transmission spectrum as measured by sending a broadband laser through the grating couplers without cQWs coupled to the cavity. The lowest order TE cavity mode is evidenced by a Lorentzian peak with quality factor ~ 2,400. 42

Figure 3.3 (a) The cavity-PL spectrum as measured by optically pumping the cQW PL and collecting through a grating coupler. The same cavity mode is presented. (b) Time-resolved PL data for both uncoupled and cavity-coupled cQWs. The solid lines represent biexponential decay fits to each data set. 43

Figure 3.4 (a) Pumping power-dependent cavity-PL spectra. The solid lines represent Lorentzian fittings to the cavity modes at each pumping power. The cavity mode peak emerges as the pumping power surpasses the amplified spontaneous emission threshold near 2.9 μW. (b) The dependence of the area under the cavity mode peak as a function of pumping power plotted on a log-log scale. The curve has a soft kink at the pumping power threshold, which is indicative of high-β lasing. Plots of the solution to the laser rate equation with other values for β and experimental data for core only cQWs coupled to a similar nanobeam cavity are both shown. (c) The linewidth of the cavity mode peak as a function of pumping power from fitting to a Lorentzian lineshape plotted on a linear-log scale. Above the threshold, the linewidth decreases as a function of pumping power. The error bars represent the curve fitting error. (d) The same data shown in (b) but plotted on a linear-linear scale. 45

Figure 3.5 (a) Schematic of a deterministic positioning of PbS QDs on top of the nanobeam cavity mode using PMMA window and the emission propagation through the grating coupler. (b) Lateral and vertical mode profiles of the nanobeam cavity from the simulation. Shaded background structures represent the buried silicon nanobeam cavity in a glass. (c), (d) SEM images of the nanobeam cavity and orthogonal grating couplers before (c) and after (d) the PbS QDs integration, respectively. (e) (f) Transmission and

PL spectra of the nanobeam cavity extracted from a grating coupler before (e) and after (f) the PbS QDs integration, respectively. 50

Figure 3.6 (a) Excitation power-dependent cavity-coupled PL spectra. (b) Normalized PL spectra of the PbS QDs coupled nanobeam cavity at six different excitation powers, i.e., 0.3, 1.0, 1.6, 2.3, 3.0, 3.6 μW. (c) Excitation power-dependent linewidth. (d) Excitation power-dependent PL peak intensity. The dotted lines indicate the calculation with respect to the different β values, 0.15, 0.22, 0.40, and 1.0. Black dots indicate the excitation power-dependent spontaneous emission for the PbS QDs uncoupled to the cavity. € Excitation power-dependent ratio between stimulated and spontaneous emission, η..... 52

Figure 3.7 (a) Excitation power-dependent PL peak intensity and plot with different β values, 0.15, 0.40, and 1.0, for three different nanolaser devices coupled with PbS QDs. (b) PL spectra of three different nanolaser devices at lasing mode. 54

Figure 4.1 (a) SEM of a nanobeam cavity. Inset: magnified SEM of the cavity region. (b) Finite-difference time-domain simulation of the nanobeam cavity mode electric field intensity, $|E|^2$. (c) Transmission electron micrograph of the colossal CdSe/CdS QDs used in this work. 58

Figure 4.2 (a) Transmission spectrum of the nanobeam cavity as measured by shining the pump laser on a grating coupler and measuring the scattered light from the top. The fundamental mode has a resonant wavelength of 808.2 nm and linewidth 0.18 nm as determined by fitting to a Lorentzian lineshape. (b) Spectrum of the ultrafast pump laser centered at 808.7 nm with a Gaussian lineshape. (c) SHG spectrum of uncoupled QDs with 30 mW pump power centered at 404.4 nm. The central wavelength, linewidth, and Gaussian lineshape are consistent with SHG. 59

Figure 4.3 (a) Representative QD-cavity SHG spectrum. The spectrum is fitted to the sum of Gaussian and Lorentzian lineshapes to account for the background uncoupled SHG and cavity-coupled SHG, respectively. The cavity mode is centered at 404.1 nm. The Lorentzian lineshape and central wavelength confirm this signal originates from the fundamental cavity mode. (b) Plot of the QD-cavity SHG spectrum and fit with different intracavity powers. (c) Power series of the QD-cavity SHG intensity versus intracavity power as measured by integrating the Lorentzian portion of the spectral fitting at each pump power. Error bars were obtained from one standard deviation error of each Lorentzian fit. The power series follows a quadratic trend. 60

Figure 5.1 (a) Schematic of a single plaquette where the site resonators and link resonators are denoted in purple and orange, respectively. The black arrows trace the path of light launched from the input

waveguide and traveling clockwise around the lattice. A photon traveling in a complete clockwise loop around the plaquette accumulates a phase shift $2\pi\alpha$. Each column across the lattice is increasingly horizontally translated by ζ such that the total path length difference gives a phase shift of $\pi/2$. (b) Scanning electron micrograph (SEM) of an example 10x10 ring-resonator array. Light is coupled to and from the lattice using waveguides coupled to four separate apodized grating couplers. Inset: zoomed-in micrograph of an apodized grating coupler. The scale bars for the full-size image and the inset are 100 μm and 10 μm, respectively. (c) SEM of a site-ring situated in a larger array. The scale bar is 10 μm. (d) Schematic of the experimental set-up. A tunable laser launches light into the chip, and the transmission spectrum is measured by a photoreceiver (PR). The spatial distribution of photons is monitored by a 10x objective lens and visible camera. (e-f) Transmission drop (e) and through (f) spectra for a single representative site resonator used in the array. 64

Figure 5.2 (a) Measured transmission spectrum of the 8x8 ring-resonator array with CW input. The purple and orange regions highlight the approximate spectral regions of the short and long edge states, respectively. (b, c) Optical images of the spatial distribution of light scattered in the lattice at 777.720 nm (b) and 777.961 nm (c). Here, the short and long edges are defined with respect to the location of the input waveguide. (b-c) The white arrows indicate the locations of the inputs..... 68

Figure 5.3 (a) Measured transmission spectrum of the 8x8 ring-resonator array with CCW input. The orange and purple regions highlight the approximate spectral regions of the long and short edge states, respectively. (b, c) Optical images of the spatial distribution of light scattered in the lattice at 777.739 nm (b) and 777.982 nm (c). (b-c) The white arrows indicate the locations of the inputs. 70

Figure 5.4 (a) Scanning electron micrograph of the 8×8 ring-resonator array with an intentionally removed site resonator. The white arrow indicates the location of the missing resonator. The scale bar is 100 μm. (b-d) Optical images of the spatial distribution of light scattered in the lattice at 777.643 nm (b), 777.677 nm (c), and 777.714 nm (d). The light in the short edge state tightly rounds around the defect with minimal scattering into the bulk. (b-d) The white arrows indicate the locations of the inputs..... 71

Chapter 1 Introduction

1.1 Motivation

Photonics has widespread applications across a variety of domains including sensing, quantum information processing, and optical signal processing.[1–3] In order to make a realistic technology using photonics, one must make an inherently scalable platform that takes advantage of the existing semiconductor fabrication infrastructure. The shorthand for this notion is that the photonics must be "CMOS-compatible," which is to say, composed of materials that are compatible with a typical semiconductor fabrication facility. In essence, this means that most photonic integrated circuits are composed of silicon and silicon compounds such as silicon dioxide and silicon nitride. While such materials have been well-documented as excellent platforms for low loss passive photonic components,[4] they lack crucial properties such as nonlinearity, which is essential for extending the application range of photonics[5] or the ability to emit light, due to the indirect band gap.

This technological gap has motivated much research into heterogeneous integration of CMOS-compatible photonic devices with other materials.[6] For example, heterogeneous integration of lithium niobate[7] and gallium arsenide lasers[8] has been demonstrated with silicon nitride photonics using wafer bonding and transfer printing. The downside of these approaches is the large cost and imposition they impose on the materials involved.

Low-dimensional semiconductor materials, including two-dimensional transition metal dichalcogenides (TMDs) and zero-dimensional quantum dots (QDs), have emerged as an alternative. These materials offer simpler integration strategies whether by dry-transfer of TMD stamps[9] or spin-coating/drop-casting of colloidal QDs. The focus of this thesis is on colloidal QDs, which have been demonstrated to be efficient light emitters for displays and light emitting

diodes, as well as detectors,[10,11] covering key gaps in the capabilities of CMOS-compatible materials. The heterogeneous integration of colloidal QDs with photonic devices is still an emerging research field and, as will be discussed below, holds promise for applications such as on-chip light sources[12] and quantum information processing.[6]

1.2 Colloidal Quantum Dots

Since the early 20th century, it has been apparent that sufficiently small bits of matter will have pronounced quantum effects.[13] The intuition behind this is the typical introductory quantum mechanics pedagogical example: particle in a box. In the limit where the particle's de Broglie wavelength approaches the box's side length, the particle's energy levels depend strongly on the side length.[14] This implies that length scale and dimensionality are powerful tuning knobs for the properties of novel materials. Early work in low-dimensional materials consisted of the discovery of the quantum Hall effect in two-dimensional electron gases,[15] but complete confinement came with the demonstration of size-dependent colors in copper chloride nanoparticles embedded in glass.[16]

In the intervening years, semiconductor colloidal QDs have emerged as an attractive low-dimensional material owing to advances in synthesis,[17] the ability to tune bandgap by controlling the size,[18] and the enhanced density of states from reduced dimensionality.[19] These days, colloidal QDs are a highly commercialized technology, and the colloidal QD display market is expected to reach US $23.9 billion by 2029.[20] In the context of exploratory research, colloidal QDs are still a relevant, active research topic.[21] The majority of colloidal QD research focuses on II-VI semiconductor QDs, especially CdSe and CdS compositions where a CdSe core is surrounded by a CdS shell.[22] This has developed into research of colloidal QDs for single-photon sources,[23,24] optical gain material,[25] and optical nonlinearity.[26] In all of these applications, the

intrinsic colloidal QD properties would benefit from heterogeneous integration with a nanophotonic cavity to, for example, form purer single-photon sources,[27] nanolasers with lower gain thresholds,[28] and enhanced optical nonlinearity.[29] Furthermore, colloidal QDs benefit from straightforward integration with photonic devices, which promises scalability for heterogeneous devices with conventional CMOS-compatible photonics.

1.3 Nanobeam Photonic Crystal Cavities

Photonic crystals are nanophotonic devices formed by periodically structuring the permittivity of a dielectric material. In analogy to periodic solid-state materials, photonic crystals inherit similar properties such as Bloch states and Brillouin zones.[30] Early work in photonic crystals for heterogeneous integration with quantum emitters such as epitaxial QDs focused on L3 two-dimensional photonic crystal cavities.[31] However, one-dimensional nanobeam cavities have emerged as a contender to traditional L3 cavities owing to their much smaller mode volumes, which strengthens the light-matter coupling strength.[32,33] Therefore this thesis focuses on coupling colloidal QDs with such nanobeam cavities.

An exemplary nanobeam cavity is depicted in Figure 1.1a. The cavity consists of a waveguide with a one-dimensional array of elliptical holes punched into it. The outer region, also known as the Bragg region, consists of elliptical holes that form a frequency-dependent Bragg mirror centered around the cavity resonance. To form the cavity, the spacing between the holes is adiabatically tapered to the center region, also known as the defect region (Figure 1.1a inset). This forms a cavity mode where the light is trapped in a small region for a long time. A finite-difference time-domain (FDTD) simulation of the cavity mode is shown in Figure 1.1b.

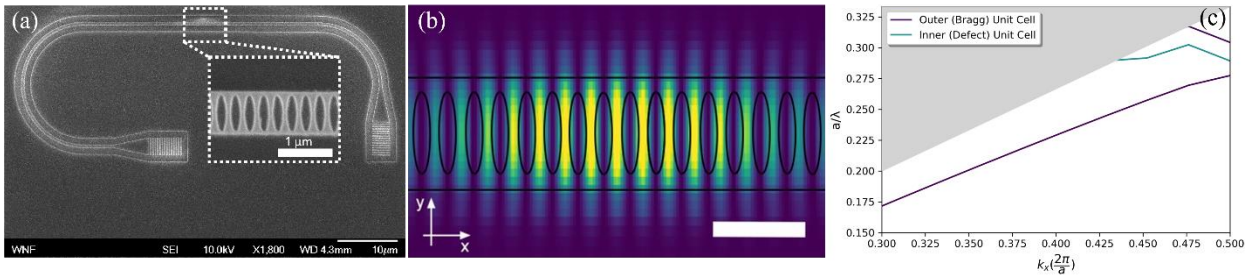

Figure 1.1 (a) Scanning electron micrograph (SEM) of a typical nanobeam cavity. (b) Finite-difference time-domain simulation of a typical cavity mode. The scale bar is 1 μm. (c) Calculation of a typical nanobeam band structure including that for the inner and outer unit cells.

One can understand the origin of this cavity mode using photonic crystal theory.[30] Essentially, in a photonic crystal consisting entirely of the outer/Bragg unit cell, a band gap will form at the edge of the Brillouin zone, as shown in Figure 1.1c (purple lines). In the absence of any defects, such a photonic crystal would act as a drop-filter by reflecting light in a frequency range corresponding to the band gap. The cavity is created by introducing a defect in this photonic crystal. The defect is specifically designed to support a mode at the edge of the Brillouin zone in the center of the band gap at the target resonant frequency (Figure 1.1c, teal line). This is done by adjusting one or more physical parameters of the outer region. Given that Maxwell's equations are scale-invariant in the absence of charges and currents[34], as is a given in most situations in nanophotonics, the resonant wavelength scales directly with physical cavity parameters such as elliptical hole size and spacing. It has been found in this group that adjusting the elliptical spacing is the most effective way to form the cavity.[35] Therefore, the inner region consists of identical elliptical holes to the outer region except the spacing is longer. This effectively "pulls down" the lower frequency band of the hypothetical photonic crystal band structure formed by the inner region into the center of the band gap.

The figures of merit for a cavity are primarily the quality-factor, Q, and the mode volume. If we define the intrinsic cavity decay rate as κ and the resonant wavelength as ω, the quality factor is defined as[36]:

$$Q = \frac{w}{2\kappa} \tag{1.1}$$

The mode volume is further defined as:

$$V = \frac{\int dV\, \varepsilon(\boldsymbol{r})|E(\boldsymbol{r})^2|}{\varepsilon(\boldsymbol{r}_{max})|E(\boldsymbol{r}_{max})|^2} \tag{1.2}$$

Where $\boldsymbol{r}_{max}$ is the location of the maximum electric-field strength. The quality factor is the approximate number of oscillations of the electromagnetic field before the cavity mode has fully decayed and the mode volume measure confinement of the cavity mode. For a nanobeam cavity, the typical Q ~ 1,000 – 10,000 and $V \sim (\lambda/n)^3$.[37,38]

1.4 The Purcell Effect

New phenomena emerge when an emitter is coupled to a cavity. The emitter's intrinsic decay rate is denoted as γ and the light-matter coupling strength is denoted as g. There typically exist two regimes, depending on the coupling strength. If g is stronger than both the decay rates γ and κ, then the system enters the strong coupling regime.[39] In this regime, the cavity and exciton modes hybridize into so-called exciton-polaritons. This has been widely explored in the context of colloidal QDs[40–42]; however, the strong coupling will not be the focus of this thesis as nanobeam cavities typically have insufficient coupling strength to overcome the large colloidal QD decay rate.[43]

Instead, this thesis will focus on the more common situation: the so-called weak coupling regime. In this regime, the predominant cavity contribution is the Purcell Effect, which is the enhancement (or suppression) of the spontaneous emission rate of an emitter, by a factor of F_P, in the presence of a cavity.[44] The origin of this effect is in Fermi's Golden Rule, which states that the transition rate between two quantum states is proportional to the final state's density of states.[45] This derivation has been mathematically derived in several places,[46,47] and the interested

reader is invited to check those references for a mathematical treatment. In words, the role of the cavity is to provide a density of states that is significantly higher than free-space, therefore enhancing the spontaneous emission rate of a cavity-coupled emitter at the cavity resonance. This has been demonstrated with colloidal QDs several times both in this thesis and in the literature.[48–50]

Colloidal QDs exist in a regime where the emitter decay rate is significantly faster than the cavity decay rate. This is known as the "good-cavity" regime (or "bad-emitter" regime, depending on your level of optimism). Importantly, the Purcell enhancement expression takes a different form in this regime:[51]

$$F_P = 1 + \frac{3\lambda^3}{4\pi^2 n^3}\frac{Q_{QD}}{V}\psi(\boldsymbol{r}) \tag{1.3}$$

Here Q_{QD} is the QD quality factor and $\psi(\boldsymbol{r})$ is the ratio of the electric-field intensity at the emitter's location to the global maximum. This expression is significantly different from the usual one. F_P no longer depends on the cavity quality factor and instead depends on the emitter linewidth. The cavity mode volume, V, is still crucial obtaining a high Purcell enhancement. This is why nanobeam cavities, with their ultrasmall mode volumes, are relevant for colloidal QD-cavity coupling, especially in the context of nanolasers, as will be discussed later in this thesis.

The Purcell Effect is also important for colloidal QD single photon sources. It is necessary for single photon source to emit photons that are highly indistinguishable from one another;[52] however, colloidal QDs suffer from huge dephasing rates that render the photons distinguishable.[53] In terms of the radiative QD lifetime, T_1, and the optical coherence time (inverse of the total dephasing rate), T_2, the indistinguishability, $I = \frac{T_2}{2T_1}$. The record I measured so far has been perovskite QDs with relatively long $T_2 \sim 80$ ps and short lifetime $T_1 \sim 210$ ps,

resulting in $I \sim 0.19$[23], which still falls far short of the target $I \sim 1$. Therefore, even modest Purcell enhancement would result in a brighter and more indistinguishable single photon source.

1.5 Thesis Outline

The focus of this thesis is on cavity-coupling of colloidal QDs. In Chapter 2, I discuss the deterministic positioning work done in collaboration primarily with Theodore Cohen,[54] Hao Nguyen,[55,56] and Greg Guymon.[57,58] I will present several stages of the technology development starting with inkjet printing of perovskite colloidal QD ensembles on cavities, showing the suitability of inkjet printing for scalable colloidal QD heterogeneous integration. This is followed by a demonstration of inkjet printing of CdSe/CdS colloidal QDs on suspended cavities, expanding the library of devices compatible with inkjet printing. In parallel, we demonstrated deterministic placement of "giant" silica-shelled CdSe/CdS colloidal QDs on a planar substrate using template-assisted self-assembly to create an array of quantum light emitters, which shows a scalable technique for single particle placement. These works culminated in the first demonstration of single colloidal QD printing on a photonic device due to advances in "colossal" QD synthesis and electrohydrodynamic inkjet printing. This paves the way for scalable heterogeneous integration of colloidal QD quantum light emitters with nanocavities.

In Chapters 3 and 4, I cover my work on on-chip light sources, including nanolasers and second-harmonic generation, using colloidal QDs integrated with nanobeam cavities. First, we demonstrated a visible-wavelength nanolaser using colloidal quantum wells deterministically positioned on an on-substrate nanobeam. This shows the ability of deterministic positioning to enable scalable, monolithic nanolasers. Next, in collaboration with Minho Choi,[59] we demonstrated the first continuous-wave, room temperature telecom nanolaser using PbS colloidal QDs. This was enabled by integration of the PbS colloidal QDs with the low mode-volume

nanobeam cavity and resonant pumping of the QDs. Last, I demonstrated the first instance of second-harmonic generation using CdSe/CdS colloidal QDs integrated with a dielectric nanocavity. Compared to previous reports using solid-state QDs and plasmonic cavities, this is expected to be a more scalable platform for nonlinear optics.

In Chapter 5, I discuss my work in topological photonics. We demonstrated near-infrared topological edge states in a two-dimensional lattice of coupled silicon nitride racetrack resonators. This is the first demonstration of such edge states outside of the telecom wavelength range, which is relevant for enabling coupling to colloidal QDs. In addition to effectively simulating the integer quantum Hall Hamiltonian, this platform could be extended to nonlinear topological Hamiltonians by introducing colloidal QDs.

Chapter 2 Deterministic Positioning of Colloidal Quantum Dots

The following chapter is based on works written primarily by Theodore Cohen,[57] Greg Guymon,[57,58] and Hao Nguyen[55] in collaboration with me.

2.1 Inkjet Printing Colloidal Quantum Dot Ensembles on Monolithic Nanobeam Cavities

Nanoscale patterning of materials has been critical for the rapid advancement of electronic information processing technologies.[60,61] The patterning of luminescent materials attracted early research interest,[62] and this capability has become critical for many emerging photonic device platforms where the precise heterointegration of emitters and other materials on nano-photonic structures is needed.[63,64] Inkjet printing has emerged as a promising method for patterning photoactive nanocrystals (NCs) because it is a rapid, mask-free method of placing on-demand droplets of a material into any arbitrary pattern with almost no material waste.[65–67] Typical inkjet printing resolutions are limited to tens of micrometers, which is less precise than is needed for integrated photonics. Smaller printed features can be generated with electrohydrodynamic inkjet printing (EHDIJ), a process that uses an electric field applied from the print nozzle to overcome surface energetics and viscous kinetics that limit mechanical droplet formation to generate droplets far smaller than those obtained with traditional inkjet printing.[68,69]

EHDIJ printing of luminescent NCs has been used to manufacture light-emitting diodes,[70,71] photodetectors,[10] and chip-integrated plasmonic lasers.[72,73] Additionally, EHDIJ printing has been investigated as a potential method for patterning luminescent materials on integrated photonic circuits because it is compatible with numerous substrate types and ink compositions. Early work in this area focused on integrating CdSe NCs with plasmonic

structures,[74,75] and it was shown that in some cases, CdSe NCs could be placed on gold plasmonic wedge waveguides at the single-emitter level.[76] Organic dye molecules have also been coupled to photonic crystal cavities with EHDIJ printing,[72] and a recent report demonstrated that quantum emitter behavior could be obtained from EHDIJ printed terrylene dye molecules.[77] Since then, perovskite NCs have emerged as promising materials for quantum photonics due to their impressive lasing properties,[48,78] superior single-photon emission,[23,79] lifetime-limited excited-state spin coherence,[80] and intriguing collective emission properties.[81,82] These NCs have been patterned with subtractive optical lithography,[83–85] lower-resolution inkjet printing,[86,87] and EHDIJ printing for LEDs[88] and radiative lifetime-encoded security tags,[89] but EHDIJ printing has not been used to deterministically place perovskite NCs on nanophotonic cavities, an advancement that is necessary to develop next-generation chip-integrated quantum photonic devices. Furthermore, given the many documented structural instabilities of individual perovskite NCs[90] and self-assembled arrays of these NCs,[91] a thorough analysis of these materials after EHDIJ printing is necessary to evaluate whether the high voltages used during processing are compatible with these notoriously unstable materials.

In this work, we use EHDIJ printing to deterministically position $CsPbBr_3$ NCs on nanophotonic structures. Atomic force microscopy (AFM) images and photoluminescence (PL) studies of the printed NCs show that tunable NC features with diameters of 500 nm and heights of 50 nm could be reproducibly fabricated without compromising the NCs' PL properties. Additionally, we use SiN membrane transmission electron microscopy (TEM) grids to collect the first-high resolution TEM images of EHDIJ printed NCs to date. These images show that, in some cases, 200 nm printed features containing <200 individual NCs can be fabricated with EHDIJ printing. Finally, we demonstrate that this printing method can be used to

deterministically place these NCs onto SiN nanobeam cavities[50] with NC emission being successfully coupled to the cavity modes. These results show that perovskite NCs can be effectively processed with EHDIJ printing with high precision and at scale for photonic device integration.

$CsPbBr_3$ NCs were synthesized and the original ligands were replaced with didodecyldimethylammonium bromide according to methods reported previously.[90,92] This synthesis yields orthorhombic perovskite NCs with an average edge length of 9.7 ± 2.1 nm and narrow ~520 nm PL with a PL quantum yield of ~80%. The NCs were then dispersed in a 1:1 mixture of octane and hexadecane at a NC concentration of $\sim 10^{-7}$ M for the formulation of a stable EHDIJ printing ink dispersion. Figure 2.1a shows a schematic of the EHDIJ printing setup used in this work. Printing is performed by applying a voltage between the electrode within the print nozzle and the substrate ground plane. This voltage polarizes the printing solution, creating an electric field that overcomes the intrinsic surface energy controlling the meniscus curvature of the EHDIJ ink at the nozzle orifice, i.e. creating a Taylor cone at the tip of the print nozzle, as illustrated in the inset of Figure 2.1a. Computer control of the voltage parameters associated with this electric field allows droplet formation and acceleration toward the substrate, and the controlled movement of the substrate stage enables the printing of very high resolution patterns.. This approach allows fine and arbitrary tuning of the NC drop spacing in any desired pattern.

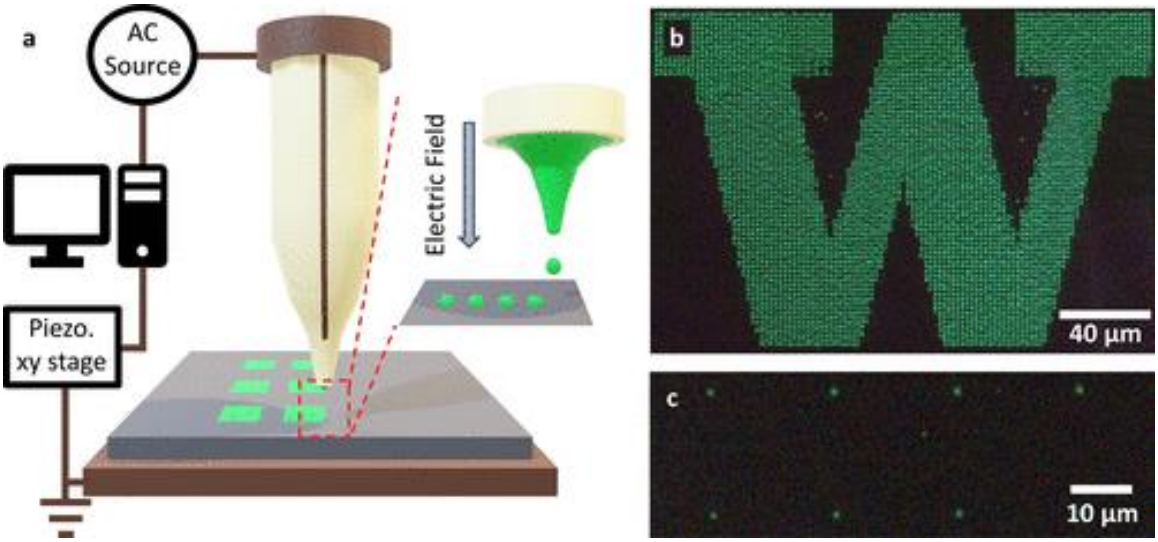

Figure 2.1 (a) Scheme describing the EHDIJ printing setup. A computer-controlled AC source creates an alternating voltage profile between the print nozzle and the printer bed via a small electrode embedded in the print nozzle. This voltage generates an electric field between the print nozzle and the print substrate that drives printing. Inset: diagram showing the effect of an electric field on the meniscus at the tip of an EHDIJ print nozzle. Partial polarization of the NC ink overcomes the ink's surface energy and draws a convex Taylor cone out of the EHDIJ nozzle to produce small droplets that form the final print pattern. PL microscope images of printed $CsPbBr_3$ NCs on a fluorinated SAM-treated silicon substrate with (b) 2 µm feature spacing and (c) 20 µm feature spacing

Figure 2.1b, c shows PL microscope images of EHDIJ printed $CsPbBr_3$ NCs under 450 nm excitation. The 210 µm print pattern in Figure 2.1b consists of 2 µm spaced NC features printed with a 70 ms hold time. Figure 2.1c shows a section of a 500 µm pattern composed of 20 µm spaced features printed with a 40 ms hold time. The hold times were selected based on an optimization to maximize the ratio of on-target to off-target printed features. Green PL is observed from each printed NC feature, and the 2 and 20 µm grid patterns are well maintained across the entire printed pattern with few defects. To test whether EHDIJ printing affects the optoelectronic properties of the $CsPbBr_3$ NCs, steady-state PL studies of NCs before and after printing were conducted. Figure 2.2a shows PL spectra of a printed NC feature and an ensemble of the same NCs drop-cast onto a silicon substrate. The PL spectrum of this large, printed feature is unchanged, but a minor blue shift is noted for smaller printed features. Furthermore, the inset of Figure 2.2a shows that, when NC print patterns are excited with 450 nm light, visible NC PL

can be observed with the eye and imaged with a cell phone camera. The NCs thus remain bright following the EHDIJ printing process.

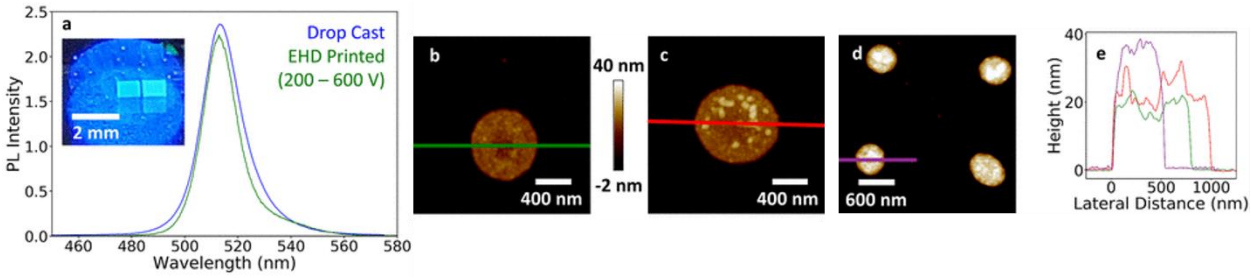

Figure 2.2 (a) Normalized PL spectra of $CsPbBr_3$ NCs drop-cast from hexanes solvent and EHDIJ printed on a silicon substrate. Inset: photograph of printed patterns on a glass substrate, under 450 nm illumination. The 1 mm^2 print patterns visible here have different brightnesses because they were printed with different parameters and different numbers of print passes. AFM images of NCs printed with 20 μm feature spacing and bump hold times of (b) 40 ms and (c) 70 ms. (d) AFM image of NCs printed with 2 μm feature spacing. (e) Height profiles from the color-coded lines in the AFM images in panels (b)–(d) showing controllable, sub-micrometer NC feature sizes.

Figure 2.2b–d shows AFM images of EHDIJ printed $CsPbBr_3$ NCs, and Figure 2.2e shows height profiles collected along the color-coded lines shown in Figure 2.2b–d. These printed features are less than 1 μm in diameter, which highlights the high-resolution patterning capability of EHDIJ printing. Figure 2.2d shows that remarkably consistent feature spacings of 2 μm can be readily achieved with this technique. The height profiles in Figure 2.2e further demonstrate that printed features can be reduced to diameters as small as 500 nm by optimizing print parameters. These liquid-ink-derived features show minimal "coffee ring" character and smaller final NC feature dimensions in comparison to features printed on untreated substrates. Finally, the step heights observed for the prints shown here are all multiples of the NC edge length of ~10 nm, demonstrating that these print features are likely composed of only two to four layers of $CsPbBr_3$ NCs.

To print NCs onto prefabricated SiN nanobeam cavities, we used an EHDIJ printing alignment process to ensure that printed droplets were placed directly on the centers of the nanobeam cavities. Aligned print patterns were then coated with poly (methyl methacrylate)

(PMMA) to encapsulate the NCs against environmental degradation during optical characterization and to preserve the inversion symmetry of the refractive index surrounding the cavity without affecting the NC PL. The nanobeam cavities are designed to maintain a high quality factor even when they are encapsulated in a polymer.[35] Figure 2.4a shows a PL microscope image of EHDIJ printed NCs on a large array of nanobeam cavities. The inset of Figure 2.4b shows a magnified image of one individual nanobeam cavity. The green emission of the printed $CsPbBr_3$ NCs is clearly visible at the centers and at the grating couplers found at both ends of each nanobeam cavity waveguide. This result shows that the printed NC emission is successfully coupled into the nanobeam cavity and that EHDIJ printing successfully placed NCs onto all the devices. Figure 2.4b shows the spectrum of emission emanating from the grating coupler of the nanobeam cavity in the inset of Figure 2.4b. In addition to the broad background PL of non-cavity-coupled NCs, a sharp peak at ~517 nm is observed. This peak can be assigned to NC emission that is coupled to the cavity mode of this nanobeam cavity. Lorentzian fitting of this peak reveals a Q factor of ~1000 for this cavity-coupled emission, which is in good agreement with the expected Q factors for this nanobeam cavity structure. We also note an additional higher order cavity peak at ~503 nm. We attribute this mode to slight out-of-plane inversion symmetry breaking of the refractive index by the printed NCs.[93]

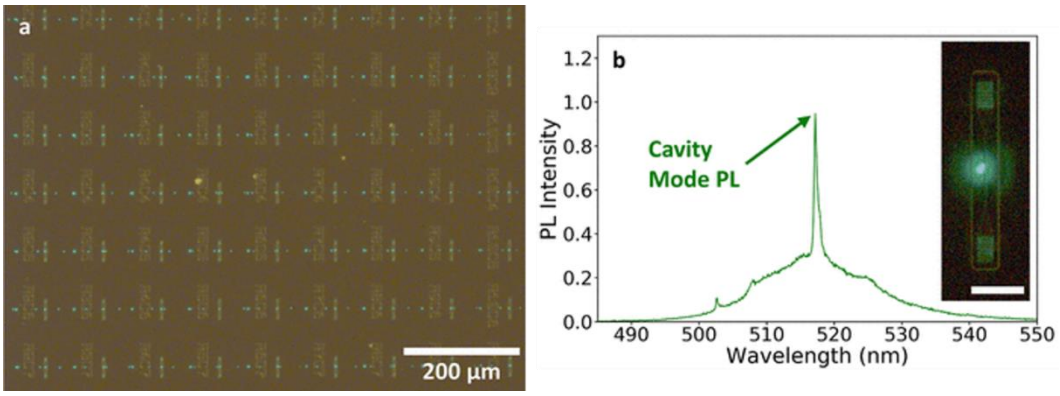

Figure 2.3 (a) PL microscope image of EHDIJ printed CsPbBr3 NCs on an array of prefabricated monolithic Si3N4 nanobeam cavities. NC features were printed with 50 µm spacing, and several off-target features are present. Visible PL can be seen emanating from the grating couplers at the top and bottom of each cavity. (b) PL spectra collected through a nanobeam cavity grating coupler. In addition to broad background CsPbBr3 NC emission, a sharp peak is observed at ~517 nm, associated with NC PL coupled to the nanobeam cavity mode (Q ~ 1000). Inset: PL microscope image of the nanobeam cavity characterized in (b). The scale bar is 10 µm.

There are several important advancements in this work that demonstrate the potential of EHDIJ printing for the integration of perovskite NCs with photonic devices. First, despite the promising structural characterization in prior reports of EHDIJ printed CdSe or perovskite NCs, the TEM data presented here provide unique and comprehensive evidence of NC structure preservation and self-assembly during the printing process. This result is particularly important for perovskites because of their well-documented environmental instability and the potential of both single-perovskite NCs as single-photon sources and self-assembled superlattices as superfluorescent correlated photon sources for chip-integrated quantum photonics. While CdSe NCs have been EHDIJ printed on plasmonic devices with near-micrometer precision, and reports of EHDIJ printed perovskite NCs demonstrate ink coalignment with a precision of ~10 µm, this report demonstrates sufficient feature alignment precision to place perovskites on a ~10 mm^2 array of dielectric photonic crystal cavities with unmatched, sub-micrometer precision. The coalignment imprecision here is greater than one micrometer but can be improved by using a more precise print stage and alignment setup. Similarly, the Q factor of ~1,000 demonstrated here can be improved through an improved cavity design.

2.2 Inkjet Printing Colloidal Quantum Dot Ensembles on Suspended Nanobeam Cavities

This EHDIJ technique was expanded to include deterministic printing of colloidal QDs on suspended nanobeam cavities. These cavities are chosen for their maximal index contrast, which results in smaller mode volumes and higher Q-factors and compatibility with strain tuning techniques.[28,32,49,94] However, traditional drop casting and spin coating techniques can put significant mechanical stresses on inherently fragile suspended nanophotonic structures due to capillary, kinetic, and thermal effects during the coating and drying stages of these processes.

Herein, we address the challenges of hybrid integration for high-performance suspended nanophotonic structures using contactless EHDIJ printing. We utilize robust CdSe/CdS core-shell QDs as photoactive materials, prepared in a cosolvent ink designed for the EHDIJ printing process. The materials are integrated into dielectric-mode SiN-suspended cavity pairs, designed to photonically couple with the peak emission wavelength of the QDs, at varying cavity separation distances. This work demonstrates the first, and only known, method for the deterministic positioning of quantum dots onto suspended photonic structures, with nanoscale precision.

CdSe quantum dots were synthesized via a modified hot injection colloidal synthetic approach.[95] To improve their photoluminescence quantum yield (PLQY), a CdS shell was grown over the core CdSe by slow-injection of cadmium oleate and octanethiol.[96] To prepare the synthesized core/shell QDs as a stable colloidal ink for printing, the particles were dispersed in a 1:1 octane:hexadecane mixture to a suitable concentration, indicated by the optical density of the first excitonic absorption peak. Figure 2.5a shows the normalized absorption and (PL) of the stabilized colloidal QD ink, with peak PL centered ~624 nm. The inset image in Figure 2.5a shows a colloidal QD ink under ambient light illumination (left) and UV illumination (right).

The lack of sub-bandgap scattering in the absorption spectrum and the lack of haziness in the left image showcase the high colloidal stability of the QD ink. The rich, scarlet fluorescence in the right image demonstrates the strong fluorescence of the QDs in this EHDIJ ink.

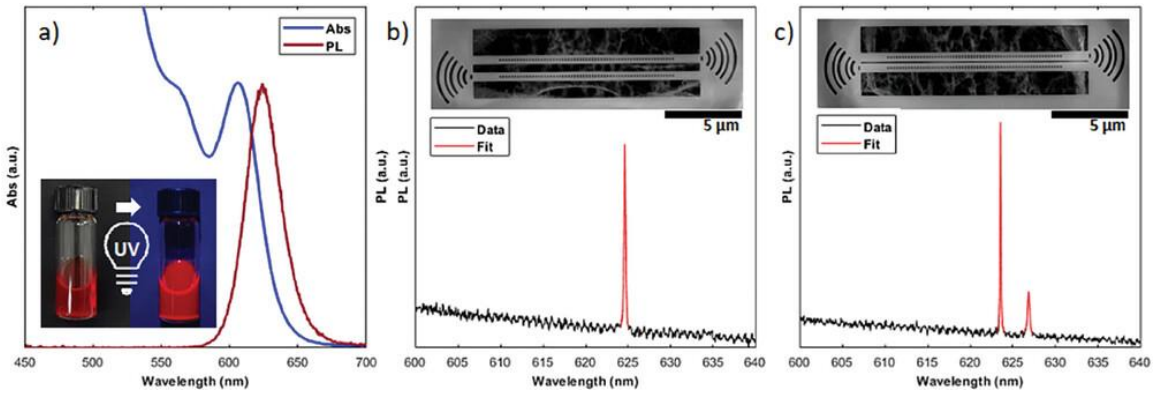

Figure 2.4 (a) Normalized absorption and PL spectra of CdSe/CdS quantum dots. Inset: Image comparison of the colloidal QD ink under ambient and ultra-violet (UV) lighting conditions. (b) PL characterization of 500 nm separated suspended Si_3N_4 cavity. Inset: SEM imagery of the respective fabricated device. The presence of a single mode peak at ~625 nm indicates no coupling at this distance. (c) PL characterization of 100 nm separated suspended Si_3N_4 cavity. The two peaks between 620 nm and 630 are assigned to two cavity supermodes, which indicates that these cavities are strongly coupled at this distance. Inset: SEM micrographs of the respective fabricated devices.

SiN nanobeams were fabricated using standard nanofabrication techniques based on SiN thin films on Si substrates. After lithography and etching, this process yields an array of SiN nanobeams that are air-surrounded (below, to the sides, and between the waveguides), except for connection of the beams to the substrate only at their fixed ends. Nanobeams were fabricated in pairs, with beam separation distances ranging from 100 to 500 nm. To determine the photoluminescent coupling and resonance of the QDs and the cavities, the devices were illuminated with 445 nm continuous wave excitation and measured via their intrinsic SiN PL spectrum. This also allowed characterization of the cavities' Q factors.

Figure 2.5b shows the PL spectrum of a nanobeam with 500 nm separation distance, fit with a Lorentzian curve, revealing a quality factor of ~ 3,400. Beams with a 500 nm separation distance can each be treated as completely isolated nanophotonic structures, demonstrated by the single sharp resonance peak at ~ 625 nm. However, reducing the separation distance of the

beams to 100 nm yields sufficient inter-cavity electric-field overlap to enter a strongly coupled regime, as seen by the two peaks in Figure 2.5c, with Q factors of ~5,400 and ~2,360 for supermodes 1 and 2, respectively. This result confirms the functionality of this device's architecture for investigating the spatial influence of photonic cavities, prior to the hetero-integration of photoactive materials. Inset images of Figures 2.5b, c highlight the cavity's suspended design, with a distinct trench etched from around and below the beams. Each device was fabricated with wedge-shaped concentric gratings to the right of the top waveguide and to the left of the bottom waveguide. These gratings diffuse light from either beam after hetero-integration and indicate the presence or absence of coupling. The web-like substance below the beams is a residual byproduct of the isotropic XeF_2 etching process.

The colloidal QDs were physically integrated with the nanophotonic cavities via high-resolution EHDIJ printing. Figure 2.6 shows a schematic of the EHDIJ tool used for this work. An example of the printing precision that can be achieved with this tool is demonstrated in the microscopy image of a printed CdSe/CdS QD array in Figure 2.6.

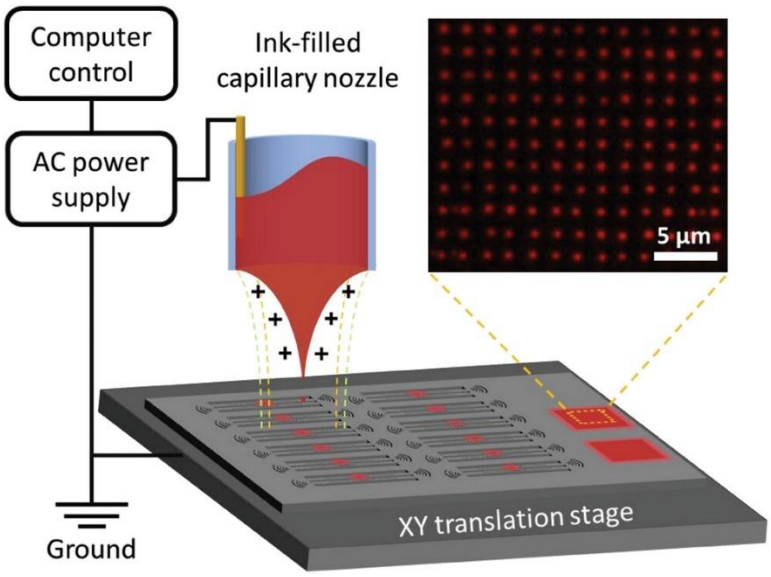

Figure 2.5 Schematic of the electrohydrodynamic inkjet printing setup used in this work. The inset image shows PL microscopy with 450 nm excitation of CdSe/CdS quantum dots printed with 2 µm pitch.

The SEM images in Figure 2.7 shows a series of dielectric-mode SiN cavities after alignment to structures on the device substrate and CdSe/CdS QD printing. Here, the presence of QDs solely on the upper beam indicates that the printed droplet only contacts and deposits QDs onto a single cavity from each pair down to cavity spacings as small as 100 nm.

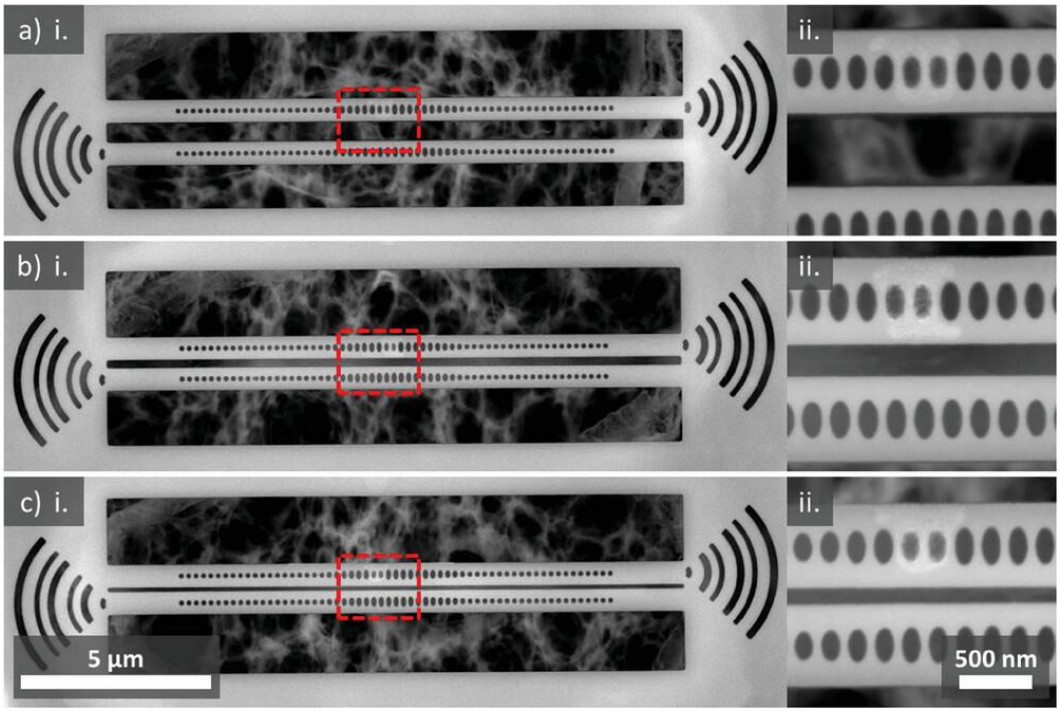

Figure 2.6 SEM imagery of suspended cavity beam pairs post-EHDIJ printing. The micrographs show an aggregation of CdSe/CdS printed on a single beam for each pair. (a) 500 nm beam separation. i. Device overview image. ii. Cavity print site image. (b) 200 nm beam separation. i. Device overview image. ii. Cavity print site image. (c) 100 nm beam separation. i. Device overview image. ii. Cavity print site image.

Following the EHDIJ printing of the QDs, the asymmetric QD-coupled nanobeam pair devices were inspected using a PL microscope under 450 nm excitation. The microscopy in Figures 2.8a-c shows suspended cavity pairs with waveguide spacings of 500, 200, and 100 nm, respectively. The emissions from the cavity and waveguide coupled to the gratings at the edge of each waveguide. These gratings were used purely for qualitative microscopy measurements because their design allowed photonic coupling to be gauged by their relative brightness. In Figure 2.8a, the emissions from the right grating indicate strong coupling between the cavity and

the quantum dots. The lack of emission from the left grating indicates no inter-cavity coupling for this waveguide's separation distance. The emission visible at the top of the left grating is due to its proximity to the top waveguide, which causes minor unintended grating coupling, but does not impact the performance of the device in any meaningful way. For the 200 nm separated cavity pair (Figure 2.8b), the brightness of the right grating indicates strong coupling between the QDs and the cavity, while the brightness of the left grating indicates detectable inter-coupling. The high light intensity at both gratings (Figure 2.8c) indicates that nanobeams separated by 100 nm show the strongest inter-cavity coupling.

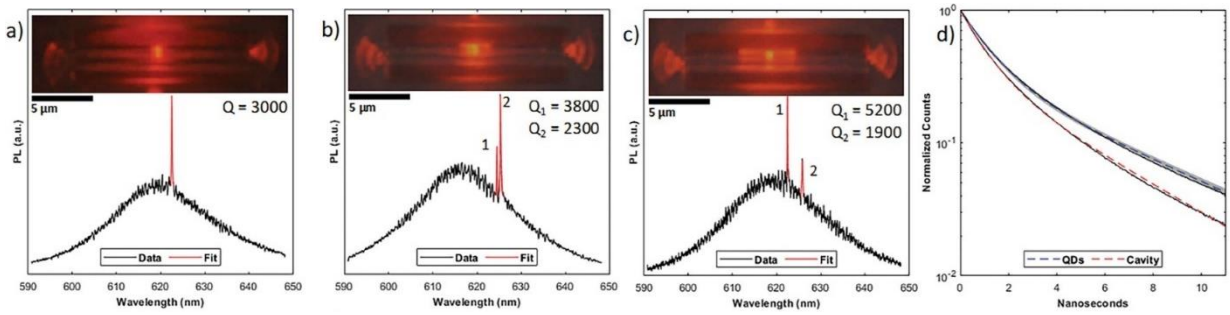

Figure 2.7 PL microscopy and characterization of asymmetrically printed QD-coupled suspended cavity pairs. (a) PL spectra of 500 nm separated suspended nanobeam cavities. Inset: PL imagery of the respective cavity. (b) PL spectra of 200 nm separated suspended cavities. Inset: PL imagery of the respective cavities. (c) PL spectra of 100 nm separated suspended cavities. Inset: PL imagery of the respective cavities. (d) PL lifetime measurements of QDs printed on the cavity site and outside of the cavity. The QD's dashed blue line represents the best-fit bi-exponential to the mean of the raw data (black) for the external QDs, accompanied by a shaded curve (gray) to represent the standard deviation of the fit. The cavity's dashed red line represents the fitted biexponential curve of the data (black) for the cavity-coupled QDs.

Having identified the photonic coupling types present and their respective strengths in each suspended cavity design through qualitative PL microscopy, we further characterized these devices through quantitative spectroscopy methods. Figure 2.8a shows PL spectra obtained by exciting the QDs with 532 nm light and collecting the resulting cavity emission from the right end of the top grating for asymmetrically printed QD-coupled nanobeam cavities separated by 500 nm. The broad peak is assigned to non-cavity coupled emission from the QDs, and the sharp peak at ~ 622 nm is assigned to QD PL that is coupled to the fundamental mode of a single

nanobeam cavity. We fit the sharp peak with a Lorentzian curve to obtain a quality factor of ~ 3,000, with no other statistically significant peaks that would indicate inter-cavity coupling. As the cavity spacing is reduced to 200 nm, two sharp peaks become visible in the PL spectra shown in Figure 2.8b with a peak spacing of ~ 0.2 Å. Figure 2.8c shows the spectroscopy of the as-printed inter-cavity coupled device with a cavity spacing of 100 nm. Here, the separation of the supermodes (Q_1 ~ 5,200, Q_2 ~ 1,900) is increased to 3.4 nm, which corresponds to a stronger coupling strength. This behavior is in good agreement with previous work using CdSe/CdS QDs and monolithic SiN nanobeam cavities.[93]

Figure 2.8d shows QD PL lifetime data collected from the upper cavity of Figure 2.8a compared to data collected for the same QDs that were printed away from the cavity. Because of the relatively large beam separation (500 nm), this system can be effectively treated as an isolated cavity for determining the Purcell enhancement of the hetero-integrated device. In both cases, the PL lifetimes were fitted to a biexponential decay. For the QDs that were not coupled to any cavities, the average fast and slow PL decay was 1.18 ± 0.07 and 5.31 ± 0.17 ns, respectively, whereas, for the cavity-coupled QDs, the fast and slow PL decay was 1.02 and 4.13 ns, respectively. This result corresponds to average Purcell factors of 1.15 and 1.29 for the fast and slow decay, respectively, which is in line with similar reports.[93] When compared to the maximum possible Purcell enhancement factor determined by FDTD simulation, the experimentally measured values were in good agreement with the simulated value of 1.34.

Colloidal quantum optical materials hetero-integrated with suspended photonic devices have been explored for their potential in next-generation optical devices, but no scalable, fully additive, and sustainable method exists to deterministically place these materials on such fragile nanostructures. By successfully combining CdSe/CdS core-shell QDs with these suspended SiN

nanobeam cavities in this work with EHDIJ printing, we convincingly demonstrate that this printing method has great potential to help elucidate the fundamental understanding of light-matter interactions and provide a viable path to manufacture fully integrated quantum photonic devices of unlimited scale and complexity. We show that the printing process has a minimal impact on emitter properties or cavity performance, and the patterning precision can reach length scales as small as 100 nm. To the best of our knowledge, this is the first demonstration of selective colloidal material positioning on suspended cavities at the length scales needed to demonstrate tunable inter-cavity coupling. Such fine patterning fidelity on these suspended structures could unlock the full potential of high gain nanomaterials,[78,97–99] magneto-optical nanoparticles,[100–102] and other narrow-linewidth emitters[55,103] with high Q-factor individual cavities,[104] cavity pairs,[38] and strain-tunable nanostructures.[94] These advanced hetero-integrated systems could be used to produce PT-symmetry lasers,[105,106] fully-integrated nanoscale optical networks,[107] and other unique device architectures that could not be fabricated without the methods described here. Furthermore, previous demonstrations of single emitter positioning with EHDIJ printing[77] and high-yield single-particle placement of individual silica-shelled CdSe/CdS QDs[55] suggest that this printing process could enable high-yield and high-precision patterning of individual emitters on nanophotonic devices to enable the manufacturing of single photon emitter-based integrated circuits.

2.3 Template-Assisted Self-Assembly of Single Colloidal Quantum Dot Arrays

Quantum nanophotonics holds great potential for several quantum technologies including quantum sensing, quantum computing, and quantum communication.[108,109] However, poor scalability is a critical hurdle that hinders progress in this field. A scalable nanophotonics platform requires replacing traditional bulky table-top optics with chip-scale photonics. One

necessary condition for such a scalable platform is the ability to deterministically position single-photon emitters in an array, and subsequent coupling to nanophotonic structures, such as resonators. Although large arrays of nanophotonic cavities have been demonstrated,[110] finding the ideal material for reliable generation of indistinguishable single photons and their scalable integration still remain outstanding challenges.

Dispersions of colloidal materials are compatible with various solution-phase integration techniques.[111–113,113,114] Straightforward integration methods, such as spin-coating, drop-casting, capillary assembly, and doctor blade coating, are often performed on patterned or templated substrates with nano- or microscale traps generated by electron beam lithography to enable precise positioning of isolated single QDs.[42,93,115–117] Deterministic and scalable positioning of one or a few QDs using these approaches can be realized when the QD size is maximized and/or the size of the predefined trap is minimized.[118,119] A different route for precise placement is to manipulate the location of a QD on a substrate with atomic force microscopy and/or SEM with a nanomanipulator;[120–122] however, this approach does not offer a feasible path to scaling. Most recently, EHDIJ has been demonstrated to deposit droplets of nanoparticles on an array of nanocavities.[54] For this technique, although the production of small ink droplets containing a few nanoparticles was achieved, targeting one particle per droplet remains difficult due to the small size of the nanoparticles and the constraints imposed by the nozzle diameter. Furthermore, implementing available techniques for large-scale patterning of QD single-photon emitters is problematic due to the QD's small size, surface chemistry, and/or poor stability in ambient conditions.[123] Overall, despite intense effort, deterministic positioning of QD single-photon emitters with high scalability remains a challenge.

Here, we demonstrate a bottom-up strategy *via* silica shelling of CdSe/CdS QDs combined with template-assisted self-assembly to deterministically position QD single photon emitters. Applications of silica-shelled QDs are ubiquitous in the biomedical field based on four major advantages: (1) optical transparency, (2) high colloidal, chemical, and optical stability of their dispersions, including in water at different pH values, (3) reduced toxicity of conventional QDs, and (4) versatility of surface modification.[124–129] In this study, we experimentally show that silica shells both increase the physical size of the CdSe/CdS QDs to facilitate device integration and stabilize the QDs to achieve room-temperature single-photon emission. We use the template-assisted self-assembly technique, recently reported for placement of nanoparticles,[130,131] to deterministically deposit single giant silica-shelled CdSe/CdS QDs in ordered arrays wherein they continue to exhibit bright single-photon emission. This synthetic approach provides a scalable and versatile strategy that could be combined with other large-scale placement methods for fabricating quantum nanophotonic devices.

For core–shell CdSe/CdS QDs, increasing the number of monolayers of the shelling material is a typical approach to achieve larger particle sizes. However, even with the laborious and time-intensive deposition of 19 monolayers of CdS, the QD size only reaches 20 nm in diameter, while a large amount of precursor material is consumed.[132] In addition, an excessively large CdS shell on a CdSe core leads to a reduction in PLQY due to the formation of interfacial defects caused by lattice strain.[133–135] The optimal PLQY is observed when 8–10 monolayers of CdS are applied to achieve QDs of 10–11 nm in total diameter.[96] Hence, we synthesized wurtzite CdSe/CdS core–shell QDs containing 9 monolayers of CdS with a total diameter of 11 ± 0.4 nm *via* the dual injection method (Figure 2.9b).[96,136] The synthesized QDs show PL centered around

640 nm with a narrow emission linewidth with a half-width-half-maximum of 27 nm and an 82% PLQY.

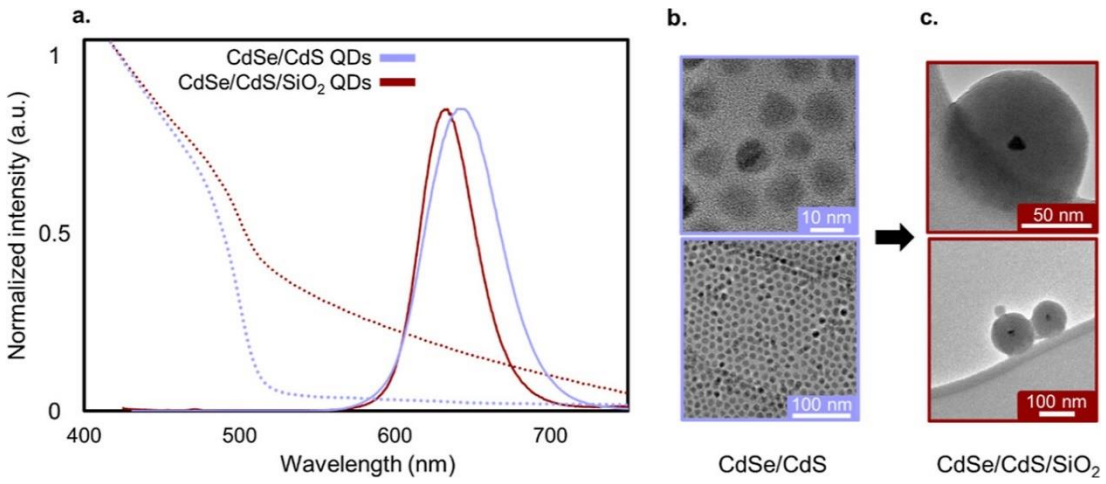

Figure 2.8 Characterization of the synthesized QDs including (a) photoluminescence (solid curves) and UV–visible absorption spectra (dotted curves), (b) TEM images of CdSe/CdS QDs, and (c) CdSe/CdS/SiO_2 QDs.

With the reverse microemulsion route, the CdSe/CdS QDs were efficiently encapsulated in silica shells with an average total diameter of 90 ± 18 nm, confirmed by transmission electron microscopy (TEM, Figure 2.9c). We also observed a small number of hollow silica particles and non-shelled QDs. After the silica shelling process, the PL of the QDs slightly blue-shifted, resulting in a peak maximum at 635 nm with an improved half-width-half-maximum of 20 nm, which are typical behaviors of silanization of QDs (Figure 2.9a).

To deterministically position the giant silica-coated QDs into arrays, we employed a template-assisted self-assembly technique that has been demonstrated to precisely arrange single nano-diamonds and gold nanoparticles with diameters as small as 40 nm across millimeter-scale areas. On a Si/SiO_2 substrate, electron beam lithography was used to define poly (methyl methacrylate) (PMMA) resist templates composed of 9 × 24 rectangular arrays of cylindrical traps with a 10 μm spacing and a depth of 157 nm, equal to the PMMA resist thickness. For every row, to optimize the capture of single 90 nm diameter silica-shelled QDs, the trap

diameters were designed to increase from 90 to 170 nm in 10 nm increments, although the actual trap sizes were measured from SEM images to be larger (likely due to overexposure or overdeveloping) and to range from 122 to 238 nm in diameter.

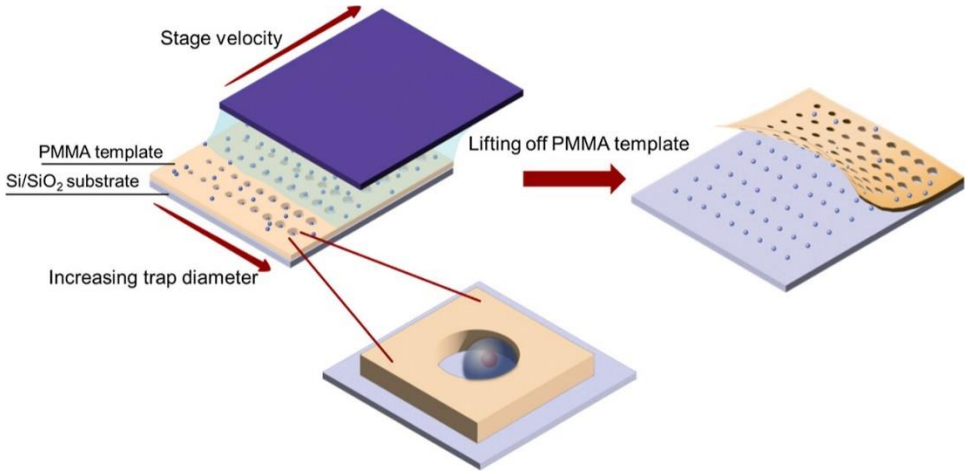

Figure 2.9 Schematic process of the template-assisted self-assembly method to deterministically place silica (light blue sphere)-shelled QDs (red sphere) in an array using a PMMA template (yellow) on a Si/SiO_2 substrate (light blue).

The assembly was performed in a home-built apparatus in which an aqueous dispersion of silica-coated QDs was deposited between a glass slide and the template surface. The QD dispersion was translated across the template surface at a speed of 2 μm/s by a motorized stage (Figure 2.10). A strong capillary force at the meniscus of the liquid rear edge drives the particles into the template traps.[137–139] During the assembly process, the environmental humidity (ambient dew point around −25 °C) and the substrate temperature (22 °C) were monitored and kept consistent as fluctuations of these factors can affect the assembly yield. Finally, a liftoff step through immersion of the samples in *N*-methyl-2-pyrrolidone for 1 min and acetone for 1 min was done to remove the PMMA layer and any non-specifically bound QDs outside of the traps.

To obtain the yield for the QD assembly into the patterned array, SEM was used to image all 216 positions of one 9 × 24 array. Positioning of QDs in the entire array was tracked by taking images of subarrays to construct the large array image (Figure 2.11a). Ordered subarrays

of QDs were clearly seen from the SEM images (Figure 2.11c), in which positions with a single QD (Figure 2.11d, e), multiple QDs (Figure 2.11f), and missing QDs could be clearly identified. Statistical characterization of the assembly showed that 75% of the traps were occupied by single QDs, 14% contained multiple QDs, and 11% were empty. Figure 2.11b shows that the optimal assembly yield for the silica-shelled QDs with an average diameter of 90 nm was achieved with a trap diameter of 160 nm, where only one position in the 24-member column was vacant. In addition, a smaller trap size (diameter < 150 nm) resulted in a higher frequency of missing QDs, and a larger trap size (diameter > 190 nm) exhibited a higher frequency of multiple QDs. From the SEM images of the array before the PMMA liftoff step (Figure 2.11d), we found that the single QDs tend to attach to the trap wall after assembling, indicating that the absolute position of single QDs from our technique is influenced heavily by the trap diameter. This leads to a trade-off between assembly yield and precise positioning, where larger traps result in better capturing of QDs, but less precision in the absolute position of the QDs.

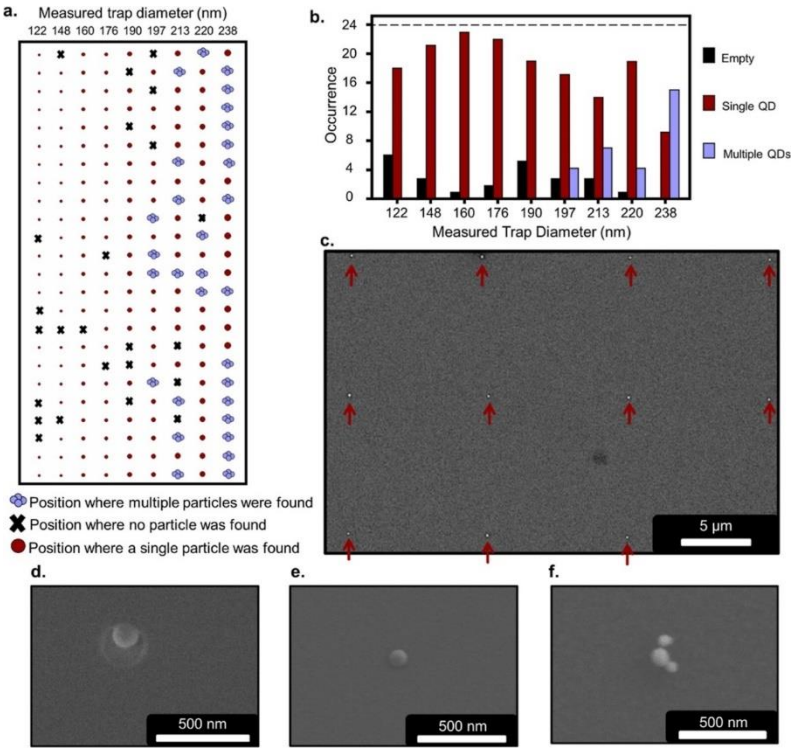

Figure 2.10 (a) Schematic construction of one 9 × 24 array showing the assembly yield. (b) Plot showing the frequency of traps containing multiple, one, or no QDs as a function of trap diameter. SEM images of (c) sub arrays of QDs, (d) a single QD in a trap before the PMMA liftoff step, (e) a single QD in a templated position after the PMMA liftoff step, and (f) multiple QDs in a templated position after the PMMA liftoff step. The contrast of the SEM images was adjusted after imaging to optimize visibility of particles and the array.

Finally, we studied the optical properties of the giant QDs in the 9 × 24 array to compare with the ones on the planar substrate. It should be noted that measurements of QDs on the planar substrate and QDs in the array were taken 6 months apart. Figure 2.12a shows the distribution of emission maxima for 34 single QDs in the array. Most of the emission peaks centered around 635 nm, consistent with the ensemble QD emission. To acquire the statistics for single-photon emission of the single giant QDs in the array, the second-order autocorrelation functions, $g^{(2)}(\tau)$, of 32 QDs were collected. Figure 2.12b displays the distribution of $g^{(2)}(0)$ values, where 16 QDs show photon antibunching behavior with $g^{(2)}(0) < 0.5$. The PL time traces of the measured QDs showed that emission bleaching occurred in less than 3.5 min for 11 QDs, between 3.5 and 10 min for 17 QDs, and after more than 10 min for 4 QDs. Additionally, blinking suppression was

observed for 10 QDs. Figure 2.12c displays the PL map of a subarray highlighting three representative QD single-photon emitters with low $g^{(2)}(0)$ values. The optical characterization of these three QDs is shown in Figure 2.12d–l, where blinking suppression was seen in QD5 and QD6 and the $g^{(2)}(0)$ value was as low as 0.14 for QD6. These results confirm that the silica-shelled QDs retained their photostability and single-photon emission through the assembly process and over a long period of time, making them suitable for photonic device operation at room temperature. This is an important advance since colloidal materials often become unstable within weeks after their synthesis when left under ambient conditions.

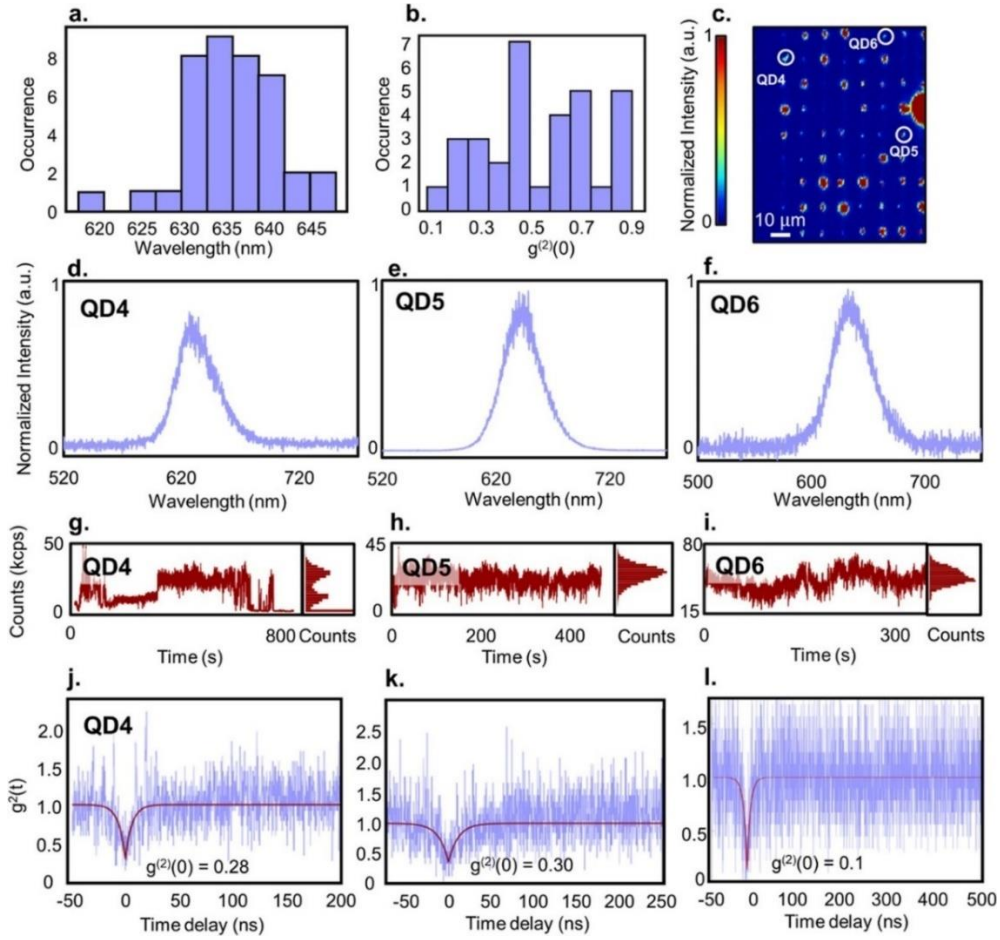

Figure 2.11 (a) Schematic construction of one 9 × 24 array showing the assembly yield. (b) Plot showing the frequency of traps containing multiple, one, or no QDs as a function of trap diameter. SEM images of (c) sub arrays of QDs, (d) a single QD in a trap before the PMMA liftoff step, (e) a single QD in a templated position after the PMMA liftoff step, and (f) multiple QDs in a templated position after the PMMA liftoff step. The contrast of the SEM images was adjusted after imaging to optimize visibility of particles and the array.

A practical nanophotonics platform using colloidal materials as quantum emitters requires scalable integration. Our work presents a combination of a synthesis design to increase colloidal QD size through silica shelling with a template-assisted self-assembly technique to deterministically position giant QD single-photon emitters in a large array, which directly demonstrates the scalability advantage of colloidal materials for photonic devices. We have shown that template-assisted self-assembly allows placement of QD single-photon emitters into a large array with high assembly yield. The giant QDs both in the array and on planar substrates showed clear antibunching, characteristic of single-photon generation. It can be expected that optimization of the silica shelling process will maintain the superior PLQY of the starting CdSe/CdS and related core/shell QDs and may mitigate photobleaching issues, thus even further improving the single-photon emission properties of these materials. We envision that the demonstrated method of silica shelling may be applicable to other highly emissive nanomaterials such as halide perovskites or semiconductor QDs emitting in the IR range, which increases their stability and will advance the use of solution processable materials in the field of quantum nanophotonics. Finally, giant silica-shelled QDs are also a flexible class of materials that may be compatible with other device fabrication techniques to achieve deterministic single-particle positioning in complex photonic platforms.

2.4 Inkjet Printing Single Colloidal Quantum Dots on Nanobeam Cavities

In the works discussed so far, we have either demonstrated scalable EHDIJ printing of colloidal QD ensembles on nanophotonic devices or less scalable template assisted self-assembly of giant silica-shelled QD ensembles on planar substrates. The missing link in these works is scalable EHDIJ printing of single colloidal QDs on nanophotonic devices, which was enabled by the recent synthesis of colossal CdSe/CdS colloidal QDs.[56] Here, we present a new EHDIJ model

that exploits nanoscale dielectrophoretics to precisely print single colloidal QDs with accuracies allowing fully-additive nanoscale photonics integration. Using colossal-shelled QDs solubilized in apolar solvents, this method overcomes continuum fluid surface energetics and stochastic imprecision that limited previous colloidal deposition strategies[140], achieving selective extraction and deposition of individual QDs at sub-zeptoliter volumes. Photoluminescence and autocorrelation function measurements confirm nanophotonic cavity-QD integration and the first single-photon emission from printed QDs. This additive, zero-waste nanomanufacturing process offers a scalable, sustainable pathway for the precise heterointegration of nanomaterials down to the single particle level, addressing key limitations in conventional nanofabrication techniques.

Recently, by leveraging dielectrophoretic (DEP) forces, EHDIJ printing has been shown to form and eject sub-attoliter liquid droplets carrying solids by polarizing the particles themselves in nonuniform electric fields[54,57]. This mechanism generates directional forces on the particles, driving solid-laden fluid along electric field gradients to allow the formation and acceleration of high surface energy small droplets towards a target substrate. Conventionally, the ink fluid has largely been considered as a continuum of liquid and solid constituents, relying on the reduction of printhead nozzle diameters to reduce droplet volumes and nanoparticle counts[141]. Here, we demonstrate a new regime of EHDIJ printing, acting on sub-zeptoliter, highly-polarizable, single particles dispersed in relatively non-polarizable solvents, to selectively extract and precisely print individual quantum dots (QDs)—a critical milestone for scalable integration of nanoscale materials. These semiconductor nanocrystals, known for their size-dependent properties, are desirable for next-generation technologies, including optical quantum devices[142,143], nano-transistors[144,145], sensors[146], light-emitting diodes[147,148], single-photon sources[123,140], and CMOS circuits[149]. For this study, we selected ligand-dispersed CdSe QDs with

colossal CdS shells (80 monolayers) due to their relatively large size (~70 nm in diameter) and high dielectric constant that result in large static electric dipole moments, good dispersion, and optoelectronic stability[56,132].

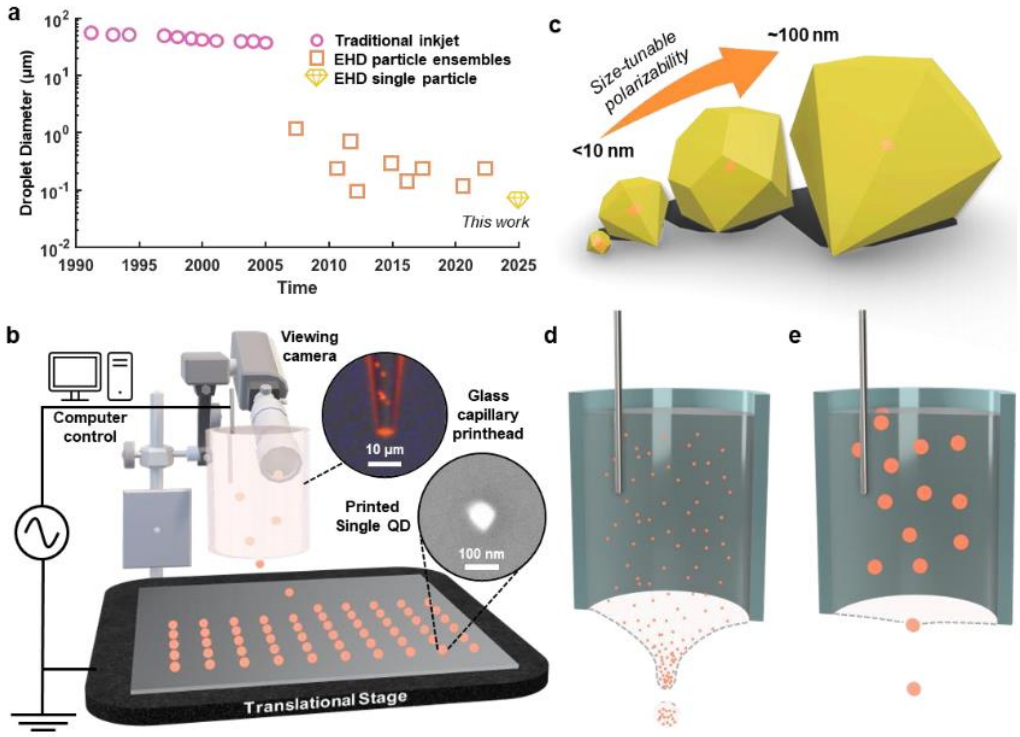

Figure 2.12 (a) Reported droplet sizes using conventional mechanical inkjet and EHDIJ printing over the past 35 years, along with the results of this work. (b) Schematic diagram of the EHDIJ printing setup used here. Top inset: fluorescence (FL) microscopy of EHDIJ printhead. Bottom inset: SEM of single EHDIJ-printed QD. (c) Graphic representation of CdSe QD cores (orange) with tunable range of hexagonal diamond CdS shell (yellow) diameters. (d) and (e), Bisected illustrations of EHDIJ printheads dielectrophoretically overcoming (d) surface tension to print droplets of particle ensembles and (e) interfacial forces to print singular particles.

Figure 2.13b schematically illustrates our EHDIJ printing setup for positioning single QD particles. Printing is initiated by applying a voltage between the electrode-integrated glass capillary printhead and the substrate. This creates an electric field that guides the QDs to the substrate. The top inset for Figure 2.13b shows a photoluminescence (PL) microscopy image of a capillary printhead loaded with dilute colossal QD suspension showing the presence of isolated emitters that include dispersed single QDs. By varying the printhead-to-substrate standoff height and applied voltage, the electric field intensity can be maximized at the tip interface. Colloidal

particles in an “ink” composed of oleic acid capped CdSe/CdS core/shell QDs suspended in an apolar solution mixture are then driven to the tip interface by the electric field. This particle mobility is achieved by utilizing a medium with a lower relative permittivity than that of the dispersed particles, which gives rise to a polarization disparity between the two that forces the particles towards regions of high electric field intensity. The QDs used in this work were synthesized via a volumetrically tunable strategy that enables the QD core to maintain its quantum-confined optoelectronic characteristics, while increasing the overall size and dipole moment of the particle in an applied field through the shell design (Figure 2.13c). The tunable polarization is crucial for generating the DEP forces needed to overcome the net interfacial energies of a single particle, especially when factors like electric field intensity and material properties have finite limits, as discussed in the following sections. The colossal core/shell synthesis yields slightly asymmetric, hexagonal, faceted particles that we approximate as spherical for later numerical and analytical estimations, due to their relatively isotropic morphology[150].

Conventional EHDIJ printing strategies focus on overcoming the energy of surface tension (Fig.1d) to generate higher area, reversed curvature liquid-gas interfaces in the form of convex Taylor cones and droplets. Alternatively, to separate a particle from a liquid-solid interface, our focus is on overcoming interfacial tension (Figure 2.13e). When the particle is more polarizable than its respective medium, like in the approach we propose here, the particle moves along the electric field gradients towards regions of high field strength, often referred to as positive DEP force, and displaces the less polarizable solvent medium.

To test this, we synthesized CdSe/CdS core/shell QDs with a calculated core radius of 1.8 nm and a designed total average radius of 36 ± 3.1 nm from 80 CdS shell monolayers (see

methods) and dispersed the particles in octane:hexadecane. Figure 2.14a shows the results of an EHDIJ printing trial matrix with this dispersion on ITO-coated SiO2 across a variety of print electrode voltage amplitudes (500-900 V) and hold times (0.5-2 s), with a fixed bias (1000 V) and frequency (1 kHz). Here, the hold time refers to the period that the amplitude voltage is applied over a position of interest. Afterwards, using machine vision to count the number of detectable prints, the heatmap shows a gradient of successful QD printing, as determined by fluorescent imaging, over this parameter space in 2D square arrays of one hundred attempts per parameter tested, with each attempt in the arrays spaced by 5 microns in both lateral dimensions on the substrate.

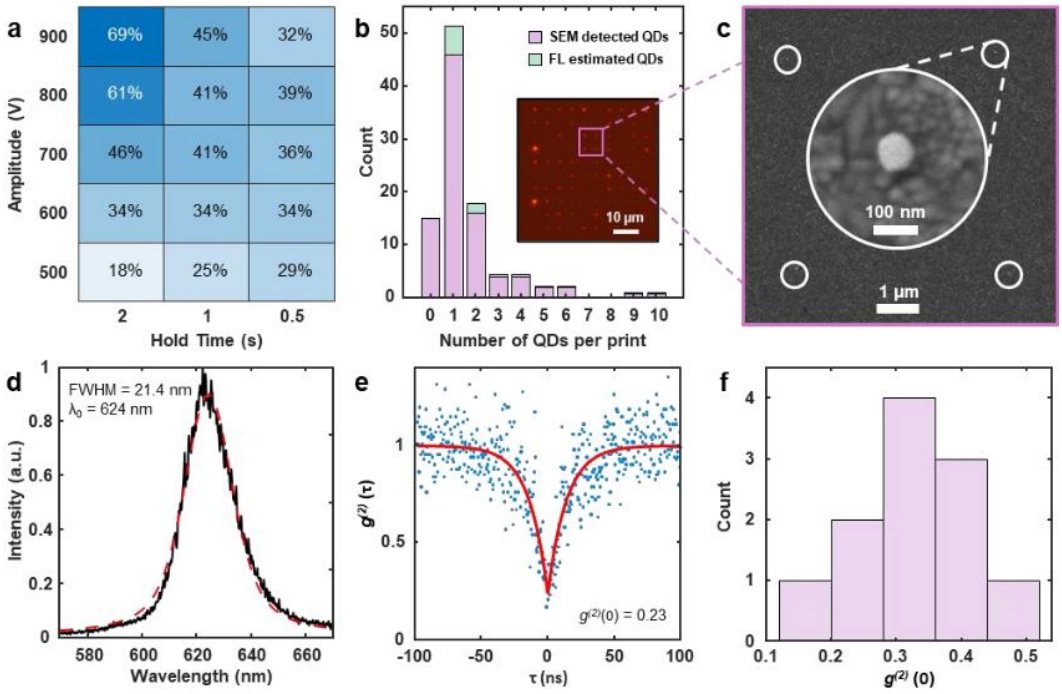

Figure 2.13 (a) Effect of drive amplitude on FL detected print yield as a heatmap of number of prints detected out of a 10 x 10 array of print attempt sites, per parameter configuration. (b) Histogram plot of QDs counted per print site for a 10 x 10 array (900 V and 2 s parameter configuration) of attempt sites, as determined by SEM and FL. Estimated QDs indicate QDs not detected via SEM but were positively-indicated by the FL microscopy (inset). The distribution of estimated QDs is based on the non-zero statistical prevalence QDs per print, per bin. (c) SEM image of 2 x 2 array of EHDIJ-printed single QDs. White circles indicate single QD positions. Inset: SEM image of single QD. (d) Plot of single QD emission spectrum (black) and Lorentzian fit (red). (e) Second-order time correlation plot (blue) and fit (red) of EHDIJ-printed QD showing single-photon emission, measured at room temperature, with 10 µW excitation (d and e). (f) Histogram plot of $g^{(2)}(0)$ measurements on EHD-printed single QDs (n = 11).

Examining the highest print yield array (900 V and 2 s) with SEM, Figure 2.14b summarizes the number of QDs detected per print via SEM and estimated via FL microscopy. Figure 2.14c shows a 2 x 2 subarray of single QDs from the larger array. The SEMs show the expected faceted structure consistent with the known morphology of these colossal QDs[56]. We performed experiments with thin-shelled[57] and smaller colossal- shelled CdSe/CdS QDs, and failed to achieve individual particle printing under similar parameters of the EHDIJ setup, again consistent with the proposed model.

Figure 2.14d shows the room temperature photoluminescence spectrum of a single printed QD with an emission peak at 624 nm, and a full-width half-maximum (FWHM) of ~21 nm, consistent with behavior of particles of this composition deposited by conventional drop-casting approaches and measured in solution. Second-order correlation ($g(2)$) measurements on the QDs confirm single-photon emission from printed QDs for the first time. Figure 2.14d shows an example of a QD maintaining its single-photon emissivity ($g^{(2)}(0) < 0.5$) after EHDIJ printing, a critical performance metric for utilizing these materials as single photon sources in quantum computing or networking technologies. Measuring a sample of the EHDIJ-printed single QDs (Figure 2.14f) shows a distribution of single-photon emitters, with a mean of $g^{(2)}(0) = 0.33 \pm 0.1$.

To demonstrate the utility of high-resolution single QD printing, we designed a horseshoe-shaped nanophotonic crystal cavity with a resonant frequency of ~614.5 nm. We fabricated the cavity with a monolithic waveguide structure that directs emission to rectangular gratings at each end of the horseshoe. Applying the printing strategy described above, we printed a single QD in the center of the cavity. Figure 2.15a shows a FL microscopy image of the emission from the single QD coupling to the waveguide and scattering from the gratings. SEM inspection of the print site (Fig.4b) confirms the presence of the single QD by identifying the

characteristic hexagonal diamond-shaped colossal QD in one of the cavities' central elliptical wells. We note that while the QD is not at the highest intensity point in the cavity, we still expect to observe significant coupling between the QD and the cavity.

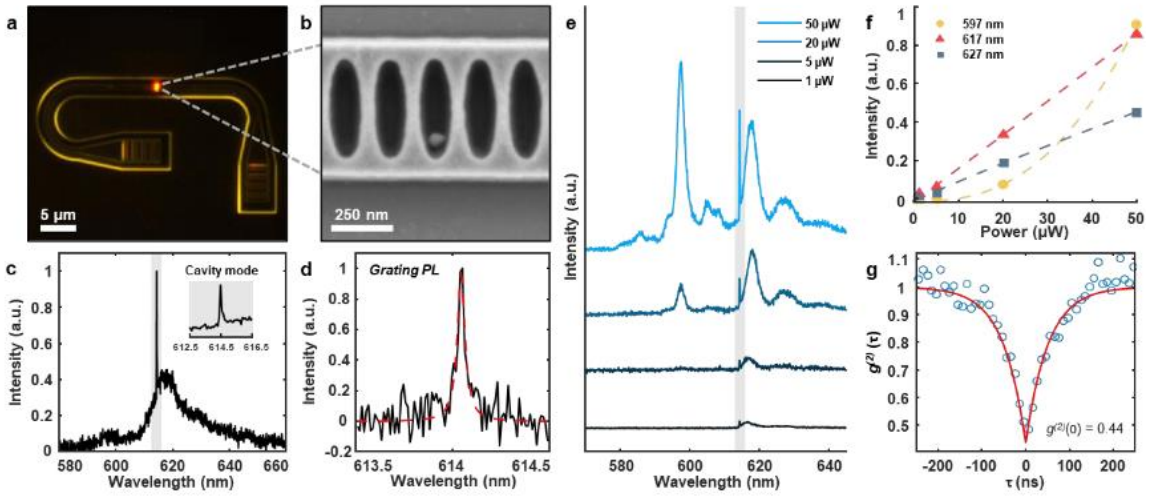

Figure 2.14 (a) Fluorescent microscopy of horseshoe-shaped cavity with single EHD-printed QD. (b) SEM image of the cavity region containing single QD. (c) Spectrum plot of cavity integrated QD, at 70 K, excited and measured from the top. Inset: Magnified spectrum (shaded) around the cavity mode. (d) Spectrum of the pure QD-coupled cavity mode PL to the grating (black) and Lorentzian fit (red) when exciting from the top, measured at room temperature with 10 μW excitation (C and D). (e) Power-dependent spectra of QD-coupled cavity at 8 K with the cavity mode region shaded (614 nm), excited and measured from the top. (f), Power dependence of 597 nm (yellow), 617 nm (red), and 627 nm (blue) peak intensities at 8 K, with power-law fits (dashed lines). (g) Second-order time correlation plot (blue) and fit (red) of cavity-coupled QD, excited (10 μW) and measured from the top at room temperature.

The photoluminescence spectrum from the cavity-integrated QD in Figure 2.15c reveals the coupling between the cavity's sharp resonant mode and a broad QD emission at 70 K, a condition chosen for its high emission intensity. Examining the narrow spectrum around the cavity mode (Figure 2.15c, inset) is consistent with a modest Fano interference, indicated by the characteristic Fano line shape[151], which is more apparent at room temperature. Measuring the room temperature photoluminescence from the cavity grating, at either end of the horseshoe, isolates emission coupled to the cavity mode. Figure 2.15d shows this sharp Lorentzian mode, with a quality factor of 12,500, measured from the Lorentzian fit linewidth over the center wavelength.

We measured the QD-cavity system at 8 K across multiple excitation powers (1-50 μW) to examine the broadened tail emission. Figure 2.15e shows the separation of the broader emission into an excitonic peak (617 nm) and its phonon sideband (627 nm). At higher power (>5 μW), we identify the emergence of a secondary high-energy peak (597 nm), which we attribute to a multi-excitonic transition, accompanied by its own phonon sideband (605 nm). The observed single excitonic and phonon sideband emission is consistent with non-cavity QDs and the 16 literature[152], at low temperature. As shown in Figure 2.15f, the exciton and phonon sideband scale nearly linearly with excitation power. The high-energy peak is highly non-linear, with an exponent of 2.5, suggesting a multi-excitonic origin. Lastly, a $g^{(2)}(\tau)$ measurement of the QD-cavity at room temperature (Figure 2.15f) shows the coupled system maintaining its single-photon emission.

Here, we have demonstrated the first additive nanomanufacturing strategy for deterministically positioning single QDs that exhibit single- photon emission. Not only does this approach allow high throughput printing of large arrays of dots at room temperature, without resorting to vacuum processing or lithography, but it also allows for the positioned deposition of dots into prefabricated nanophotonic elements such as high-Q cavities. While we used colossal (~70 nm) CdSe/CdS particles here, we estimate the method should be applicable to a range of other colloidal nanoparticles, from halide perovskites, to nanodiamonds, opening the door to a scalable, contactless, zero-wasted additive nanomanufacturing process that can be conducted at ambient conditions to enable the positioning of single discrete colloidal QDs. These results represent significant progress in realizing scalable photonic qubit platforms and the future development of quantum optoelectronics.

Chapter 3 On-Chip Nanolasers Using Colloidal Emitters

The following chapter is based on works primarily written by myself[153] *and Minho Choi, in collaboration with me.*[59]

3.1 Visible Nanolaser Using Deterministically Integrated Colloidal Quantum Wells

Hybrid integration of photonic devices with colloidal semiconductor nanocrystals is a compelling route towards large-scale active photonic devices that leverages the scalability of both CMOS-compatible photonic platforms and inexpensive colloidal nanocrystal synthesis techniques. In particular, on-chip nanolasers are an attractive application of hybrid integration that combines gain media with low-loss dielectric nanophotonic structures.[154] Colloidal semiconductor nanocrystals themselves have shown promise as a gain material in which a nanolaser is formed by self-assembly of the colloidal material into geometries such as whispering gallery mode resonators[155–157] and microdisks[158]. However, these self-assembled geometries are not appropriate for large scale applications due to their fabrication disorders and CMOS-incompatibility. Recent effort has instead turned to hybrid integration of colloidal semiconductor nanocrystals including II-VI colloidal QDs, perovskite colloidal QDs[50], and II-VI colloidal quantum wells (cQWs), also known as colloidal nanoplatelets,[28] with nanobeam photonic crystal cavities. As compared to hybrid integration efforts with other geometries such as distributed Bragg reflector cavities[159] and Fabry-Pérot cavities[40], nanobeam cavities have a small mode volume that tightly localizes the cavity mode and enhances the light-matter coupling strength.

CdSe/CdS cQWs are a promising candidate for colloidal nanocrystal gain material because their reduced Auger recombination rate, compared to II-VI cQDs, enables high gain[160,161] and lasing when integrated with a suspended silicon nitride (SiN) nanobeam cavity geometry[28]. On-substrate SiN nanobeam cavities have improved thermal and mechanical properties compared to their suspended counterparts and have been used successfully to create nanolasers with hybrid integration of perovskite cQDs[48]. Furthermore, this work employs deterministic positioning of cQWs on the cavity to offset the stochastic nature of colloidal emitter coupling and maximize overlap of the cQWs with the cavity. As an overview of the cQW-nanobeam cavity system used herein, Figures 3.1a and 3.1b depict the absorption/photoluminescence spectra and a representative transmission electron micrograph, respectively, of the cQWs used in this work, and Figure 3.1c depicts a scanning electron micrograph of a typical nanobeam cavity. By utilizing a hybrid integration scheme, we demonstrated a nanolaser with amplified spontaneous emission threshold of 2.9 μW under continuous wave pumping by hybrid integration of CdSe/CdS core/shell cQWs with an on-substrate SiN nanobeam photonic crystal cavity. We also found that cQW shelling is essential to maximizing gain.

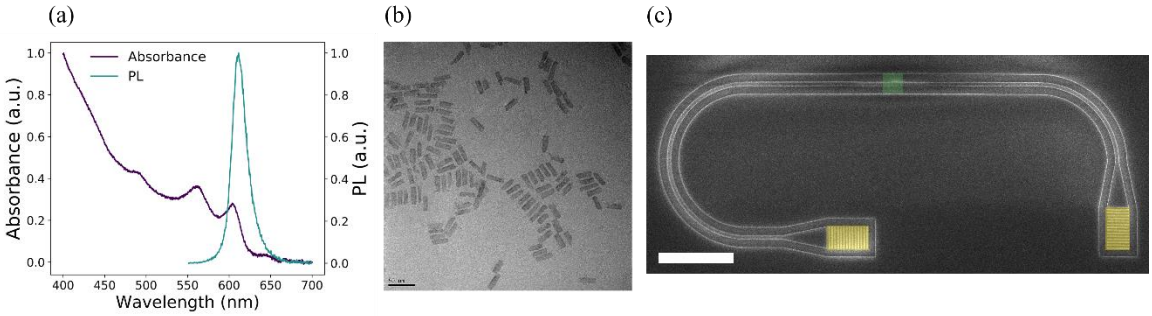

Figure 3.1 (a) Absorption and PL spectra of CdSe/CdS cQWs. (b) Transmission electron micrograph of CdSe/CdS cQWs. The scale bar is 50 nm. (c) Scanning electron micrograph of an example SiN nanobeam cavity. The cavity region coupled to cQWs and the grating couplers for collecting cavity-coupled cQW photoluminescence are highlighted in green and yellow, respectively. The scale bar is 10 μm.

4 ML CdSe cQWs were synthesized according to previous literature.[162] Briefly, 170 mg of cadmium myristate, 12 mg of selenium powder, 15 mL octadecene (ODE) were combined into a 50 mL three-neck flask and evacuated at room temperature for 1 h. Under nitrogen flow, the flask was heated to 240 °C. At 190 °C, 40 mg of finely ground cadmium acetate dihydrate was quickly added to the flask. The reaction temperature was maintained for 10 min after reaching 240 °C, then quickly cooled by air flow. At 100 °C, a solution of 2 mL oleic acid in 15 mL methylcyclohexane (MCH) was injected and the solution was stirred under nitrogen overnight. The cQWs were isolated by centrifugation at 11000 rpm for 10 minutes. The pellets were redispersed in MCH.

Subsequently, CdS shell growth were performed on 4 ML CdSe cQWs by colloidal atomic layer deposition (c-ALD) based on literature methods[163]. In a nitrogen-filled glovebox, core cQWs (~20 mg) were precipitated from the stock solution in MCH with ethanol. The cQWs were redispersed in 100 µL MCH and combined in a 4 mL vial with 500 µL ODE, 100 µL oleylamine, and 10 mg Li_2S with a glass stir bar. The mixture was stirred at 150 °C on a hot plate for 90 seconds. The S^{2-} capped cQWs were precipitated once with ethanol and then redispersed in 100 µL MCH. To grow the Cd layer, the cQW solution was added to a 4 mL vial containing 500 µL ODE, 100 µL oleylamine, and 15 mg cadmium formate. The mixture was stirred at 150 °C for 3 minutes, following by centrifugation and decantation to remove excess solids. The cQWs were precipitated with ethanol and redispersed in 100 µL MCH. This completed one monolayer growth of CdS shell. The second monolayer was grown by repeating the same process.

The nanobeam cavity was designed for thin-film SiN on buffer SiO_2 with polymethyl methacrylate (PMMA) encapsulation. The refractive index of PMMA closely matches that of the

underlying SiO_2, which preserves the out-of-plane inversion symmetry.[164] This has been shown to enable high quality factor SiN nanobeam cavity designs[35,54]. Verification of the cavity design was implemented in the finite-difference time-domain (FDTD) solver from Lumerical. The simulation layout consisted of a SiN waveguide with elliptical holes, surrounded by a uniform PMMA/SiO_2 medium. The 220 nm thick SiN waveguide was set to an unperturbed elliptical hole period of 183 nm, a defect period of 175 nm, an elliptical hole major radius of 220 nm, a minor radius of 50 nm, and a waveguide width of 550 nm. The cavity defect was formed in the center by quadratically tapering the elliptical hole periodicity from the defect period to the unperturbed period over 10 periods on either side. Extra mirrors to strengthen the light confinement were formed by adding 15 more periods of unperturbed elliptical holes on either end. The resulting cavity mode electric field profile is shown in Figure 3.2a. This resulted in a theoretical quality of factor of ~10,000 and mode volume of ~2.1 $(\lambda/n)^3$.

The nanobeam cavity was fabricated using a 220 nm thick LPCVD SiN on 4 μm thermal SiO_2 on silicon wafer from Rogue Valley Microdevices. To define the pattern, ~300 nm thick ZEP520A positive-tone electron-beam lithography resist was spun-coat on the surface and patterned with a 100 kV electron-beam lithography system. The pattern was transferred to the underlying SiN layer using a plasma etch consisting of fluorine-based chemistry. Figure 3.2b shows a scanning electron micrograph of the nanobeam cavity centered on the defect region. In order to deterministically position ensembles of cQWs on the nanobeam cavities, windows in a cladding layer of PMMA were opened with a subsequent aligned electron-beam lithography step. This has been shown to increase the coupling efficacy of colloidal nanocrystals to nanobeam cavities by ensuring the cQWs pack into a thick film on top of the nanobeam cavity[93].

Before integrating the cQWs, the nanobeam cavities were first characterized using

transmission measurements since the nanobeam cavity is coupled to a SiN waveguide and grating couplers. A broadband laser was shined on one grating coupler, and the transmission spectrum was collected at the other grating coupler using a confocal multi-mode optical fiber. Figure 3.2c shows an example transmission spectrum of a nanobeam cavity. Although several modes are present, the results here focus on the coupling of the lowest order TE-mode. By fitting to a Lorentzian lineshape, the experimental quality factor is found to be ~2,400. The experimental quality factor is smaller than the simulated one, which is attributed to fabrication imperfections.

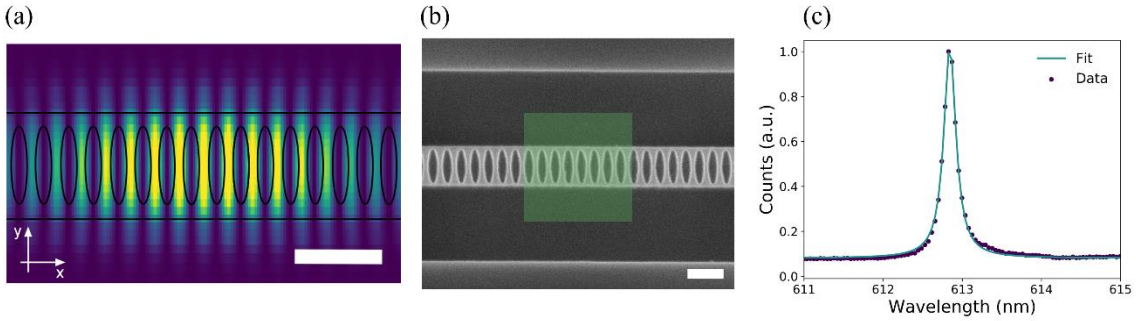

Figure 3.2 (a) The profile of the cavity mode electric field E_y from FDTD simulation. The scale bar is 500 nm. (b) Scanning electron micrograph of the nanobeam cavity defect region. The PMMA window is highlighted in green. The scale bar is 500 nm. (c) Nanobeam cavity transmission spectrum as measured by sending a broadband laser through the grating couplers without cQWs coupled to the cavity. The lowest order TE cavity mode is evidenced by a Lorentzian peak with quality factor ~ 2,400.

cQWs were integrated with the nanobeam cavities by drop-casting a hexane solution containing cQWs onto a chip containing many nanobeam cavities prepared with open PMMA windows. The devices were re-encapsulated with PMMA to cover the open windows. The coupling of cQWs was first confirmed by measuring the cavity-coupled photoluminescence (cavity-PL) spectrum. For all cavity-PL experiments, the chip was placed in a vacuum chamber to prevent degradation of the cQWs under laser excitation. A 445 nm continuous wave pump laser was shined on the cavity defect region containing cQWs using a 40x (0.6 NA) objective lens, and the cavity-PL spectrum was collected at a grating coupler to minimize background

from uncoupled cQWs. The cavity-PL spectrum for the nanobeam cavity considered in the rest of this work is shown in Figure 3.3a. By fitting this spectrum to a Lorentzian lineshape at high pump powers, a cQW-cavity coupled quality factor of ~830 is extracted. The degradation of the pristine nanobeam cavity quality factor indicates that the cQWs are coupled well to the cavity.

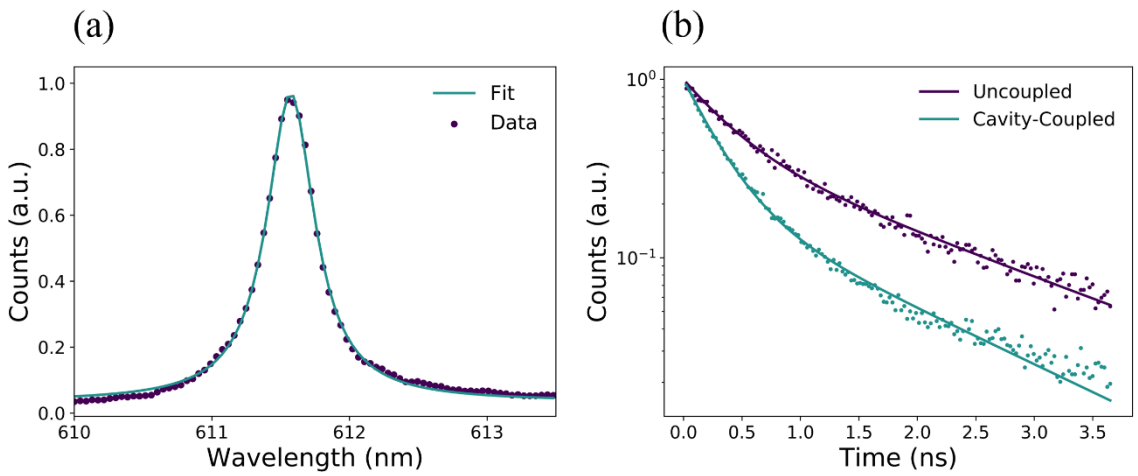

Figure 3.3 (a) The cavity-PL spectrum as measured by optically pumping the cQW PL and collecting through a grating coupler. The same cavity mode is presented. (b) Time-resolved PL data for both uncoupled and cavity-coupled cQWs. The solid lines represent biexponential decay fits to each data set.

Time-resolved measurements of the cavity-PL were performed to further confirm coupling of the cQWs to the nanobeam cavities because it is expected the nanobeam cavities will reduce the cQW spontaneous emission lifetime by the Purcell enhancement factor[165]. In the limit where the emitter linewidth is much broader than the cavity linewidth, this factor is given by:[28]

$$F_P = 1 + \frac{3\lambda^3 Q_{em}}{4\pi^2 n^3 V}\psi(r) \tag{3.1}$$

where λ is the cavity resonance wavelength, Q_{em} is the quality factor of the cQW PL, n is the refractive index of the cavity dielectric, V is the cavity mode volume, and $\psi(\boldsymbol{r})$ is the ratio of the cavity mode electric field intensity at the emitter's location to the global maximum. For this system, $Q_{em} \sim 34$ and $\psi(\boldsymbol{r})$ is 0.32 as the cQWs interact with the evanescent field on top of the nanobeam cavity. Therefore, the theoretical Purcell Enhancement $F_P \sim 1.4$.

The time-resolved PL was collected for both uncoupled and cavity-coupled cQWs using a pulsed pump laser (532 nm, 80 MHz repetition rate) and is shown in Figure 3.3b. The lifetime was extracted by fitting the time-resolved PL to a biexpontential decay model due to the presence of two radiative decay pathways in CdSe/CdS cQWs[166]. From these fits, fast and slow decay time constants 0.39 ns and 1.77 ns (0.27 ns and 1.39 ns), respectively, were extracted for uncoupled (cavity-coupled) cQWs. This corresponds to an average Purcell Enhancement of 1.3, which is slightly smaller than the theoretical prediction because not all the cQWs are coupled to the cavity mode electric field maximum.

To characterize the lasing behavior of the nanobeam cavity coupled to cQWs, power-dependent cavity-PL measurements were performed. The pumping power was monitored by a beam splitter in front of the objective lens and cavity-PL spectra were recorded at each pumping power. Figure 3.4a depicts the cavity-PL spectra collected at different pumping powers. This shows an evolution of the cavity mode from a weak mode dominated by the background uncoupled cQW PL to a clear cavity peak as the system transitions to the amplified spontaneous emission regime.

Figure 3.4b and 3.4d show the "light in-light out" curve i.e. the dependence of the cavity mode intensity, defined here as the integrated area under the cavity mode Lorentzian peak, on the pumping power, respectively plotted on log-log and linear-linear scale. These data were fitted to the laser rate equation:[167]

$$R_{\mathrm{ex}} = \frac{P}{\Gamma t_{\mathrm{c}}(1 + aP)}\left(\frac{1}{\beta} + aP\right) \tag{3.2}$$

where R_{ex} is the external pumping rate, P is the photon number in the cavity, Γ is the cavity confinement factor, t_c is the cavity lifetime, a is the efficiency of stimulated emission into the cavity mode, and β is the ratio of emission rate into the cavity mode against emission rates into

all modes. The lasing pump power threshold is commonly defined as the point in which the mean cavity photon number equals unity[168]. Therefore, Equation 3.2 predicts the lasing threshold occurs when the product $aP = 1$. According to the fit to Equation 3.2, the light in-light out curve displays a high β of 0.57, which results in a soft kink at the calculated pumping power threshold of 2.9 μW and is in line with similar reports[28].

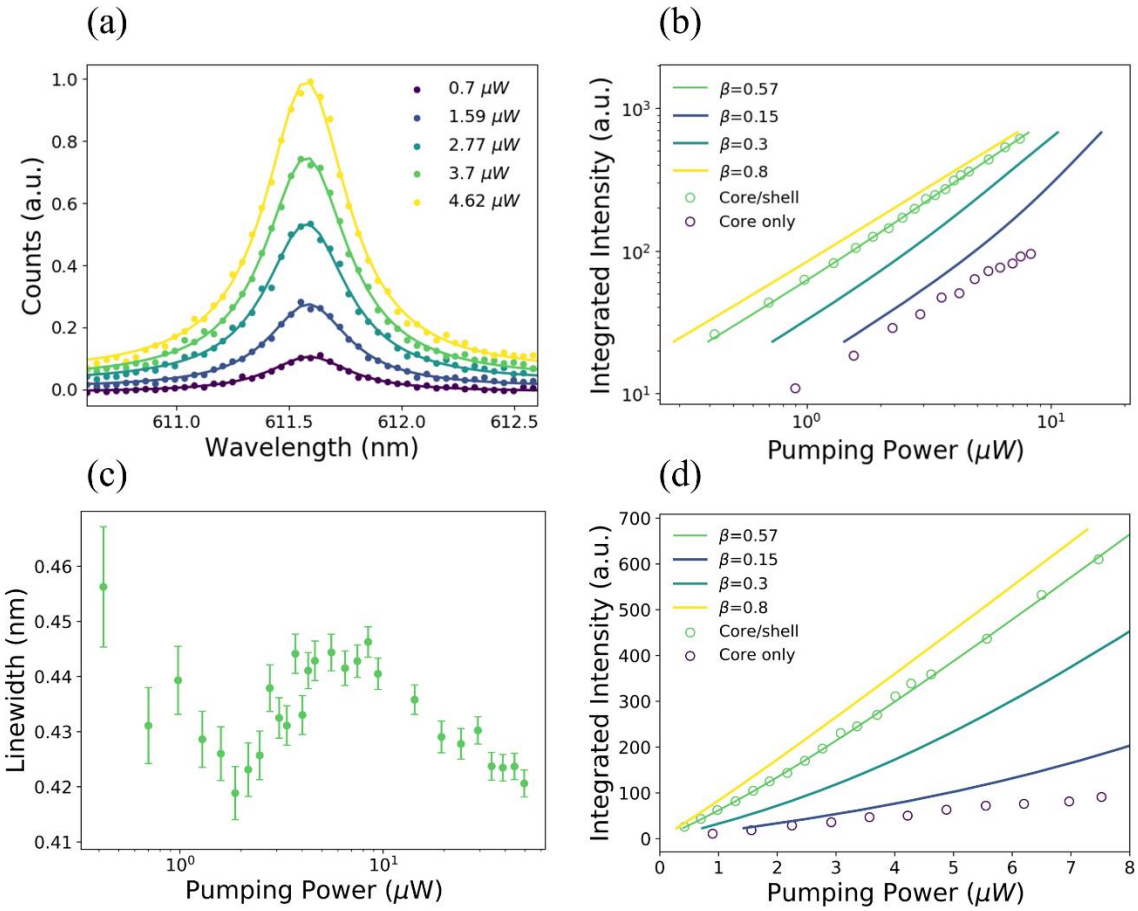

Figure 3.4 (a) Pumping power-dependent cavity-PL spectra. The solid lines represent Lorentzian fittings to the cavity modes at each pumping power. The cavity mode peak emerges as the pumping power surpasses the amplified spontaneous emission threshold near 2.9 μW. (b) The dependence of the area under the cavity mode peak as a function of pumping power plotted on a log-log scale. The curve has a soft kink at the pumping power threshold, which is indicative of high-β lasing. Plots of the solution to the laser rate equation with other values for β and experimental data for core only cQWs coupled to a similar nanobeam cavity are both shown. (c) The linewidth of the cavity mode peak as a function of pumping power from fitting to a Lorentzian lineshape plotted on a linear-log scale. Above the threshold, the linewidth decreases as a function of pumping power. The error bars represent the curve fitting error. (d) The same data shown in (b) but plotted on a linear-linear scale.

Figure 3.4b and 3.4d also depict a typical light in-light out curve for CdSe core-only cQWs coupled to a similar nanobeam cavity designed for spectral overlap with CdSe core-only cQWs. This curve shows weaker cQW-cavity coupling and no clear threshold, which suggests that the CdSe/CdS cQW core/shell morphology is essential for high gain. Optical gain in both core-only and core/shell cQWs originates primarily from biexcitons[159,162]. Core-only cQWs, in comparison to their core/shell counterparts, experience charge trapping that diminishes their PL quantum efficiency, broadens PL linewidth, and creates delayed emission due to unpassivated Se edge sites[169,170]. In addition to their intrinsic high susceptibility to surface defects and low stability, cQWs in thin films encounter a greater effective dielectric medium leading to decreased exciton binding energy[171]. This behavior results in more severe reduced radiative recombination, decreased PL quantum yield, and ultimately lower optical gain when compared to core/shell cQWs.

The dependence of the cavity mode linewidth as a function of pumping power was extracted by fitting each spectrum to a Lorentzian cavity mode and is shown in Figure 3.4c. This shows a linewidth of 0.458 nm at low pumping powers that narrows to 0.418 nm and re-broadens to 0.440 nm due to gain-index coupling below the predicted threshold[172]. As the pumping power crosses the predicted threshold, the linewidth monotonically decreases due to increasing coherence time in the cavity and suppression of the spontaneous emission. This linewidth behavior, in conjunction with the light in-light out curve, confirms that the cQW-nanobeam cavity system is behaving as a nanolaser.

A continuous wave optically pumped nanolaser based on hybrid integration of solution-processed CdSe/CdS core-shell cQWs and an on-substrate SiN nanobeam cavity was demonstrated. The amplified spontaneous emission onset threshold was calculated to be 2.9 μW.

Deterministic integration was utilized to maximize coupling of the colloidal gain material to the nanobeam cavity, and it was shown that core/shell cQWs generate greater optical gain than their core-only counterparts, enabling lasing. The wavelength range of similar devices could span the visible spectral range by controlling the cQW composition and modifying the periodicity of the nanobeam cavity elliptical holes[173]. As previously mentioned, similar nanobeam cavities integrated with core-only CdSe cQWs did not yield lasing. This suggests that the core-shell cQW morphology is essential for optical gain and that advancements in the cQW synthesis and chemical composition, for example by creating graded heterostructures, could further improve the lasing performance[174]. Optimization of active gain area by altering the PMMA window size could improve the lasing performance in future studies. Furthermore, by incorporating the nanobeam cavity with another resonator, deterministic positioning could be used to selectively apply gain material to a single cavity to module the gain-loss balance in the coupled cavity system[105]. Electrically pumped lasing of II-VI cQD light-emitting diodes has been recently demonstrated, which suggests electrically pumped lasing with II-VI cQWs may be possible[175].

3.2 Continuous-wave Infrared Nanolaser Using PbS QDs on a Silicon Nanobeam

Making a laser out of silicon is one of the paramount challenges in the field of photonics. However, the indirect bandgap of silicon fundamentally limits its possibility even just as an emitter. Over the last few decades, numerous alternative approaches have created CMOS-compatible lasers, and the most established way in both industry and academia is using hybrid integration of III-V compound semiconductors, i.e., InGaAs or InP, to a silicon substrate using wafer bonding or transfer printing.[176–179] However, there is a significant amount of cost associated with this hybrid integration procedure. Another approach is epitaxial growth of germanium on silicon, where the germanium itself has an indirect bandgap around 0.66 eV, but

becomes a direct band gap under tensile strain.[180,181] Elsewhere, researchers created several defect states inside the silicon and utilized them as an emitter and silicon as a host medium.[182,183] However, both approaches of Ge/Si and defect centers are facing difficulties as an industrially wide-spread platform due to the complicated fabrication procedure and probabilistic success rate.

Solution-processed materials, e.g., QDs, nanocrystals, or nanoplatelets in solvents, are rapidly growing platforms that have high stability and quantum yield, as well as a large degree of freedom for integration regardless of the substrate materials.[184,185] One major reason that two-dimensional materials are highlighted is their versatile scalability with transfer printing; however, solution-processed materials have larger-area scalability as they can be simply spread out, e.g., spin coated or drop casted, then dried for integration. Many recent works have leveraged solution-processed materials to demonstrate highly efficient light-emitting diodes,[186,187] sensors,[188,189] and lasers.[190,191] Nevertheless, a solution-processed silicon nanolaser has never been demonstrated yet.

Lead sulfide (PbS) QDs have a direct band gap in a wide range of near-infrared wavelengths from 800 to 2,200 nm, depending on the size of the QDs. Due to its high quantum yield, it has been widely used as both an efficient absorber and emitter in various optoelectronic fields.[192–195] In this work, we used PbS QDs immersed in a toluene solvent, which has a band gap energy of around 0.8 eV, as a gain medium for a silicon nanolaser. We fabricated a high quality-factor (Q-factor) nanobeam cavity and then deterministically positioned the PbS QDs at the center of the cavity mode region. To verify its lasing phenomenon, we directly excited the PbS QDs with a continuous-wave laser and an objective lens, then collected the cavity-coupled PL from the grating coupler. We adjusted the excitation laser power from 0 to 6 μW, and observed the cavity-coupled PL transition from spontaneous emission (SE) to amplified spontaneous

emission (ASE) and lasing due to significant linewidth narrowing, ~30%, and non-linear PL intensity profile along the excitation power increases.

Our nanolaser consists of a nanobeam cavity, which confines light in a small mode volume with a high Q-factor, and two orthogonal grating couplers, which extract in-plane light to free space for optical characterization. Since the two grating couplers are optimized for polarized light which are orthogonal to each other, we can measure transmission spectra from one grating to another to characterize the resonant wavelength and Q-factor of nanobeam cavity. When integrating the PbS QDs with the nanobeam cavity, we should be aware that the PbS QDs not only emit light but also absorb light. Therefore, having PbS QDs only near the cavity mode region and not along the waveguide and grating couplers can minimize unwanted absorption and scattering.[196] We patterned a PMMA window at the cavity mode maximum (Figure 3.5a), and then the coated PbS QDs on top of the window resulting in the deterministic positioning and coupling of the QDs to the nanobeam cavity. There are still a lot of QDs on top of the PMMA layer, but the large thickness of the PMMA layer, ~400 nm, isolates these QDs from the nanocavity mode. For the lasing experiment, we excited the QDs directly from the top by optical pumping with a 1480 nm continuous-wave laser using an objective lens of NA 0.65 and collected its photoluminescence out of the one grating coupler to measure the cavity-coupled emission.

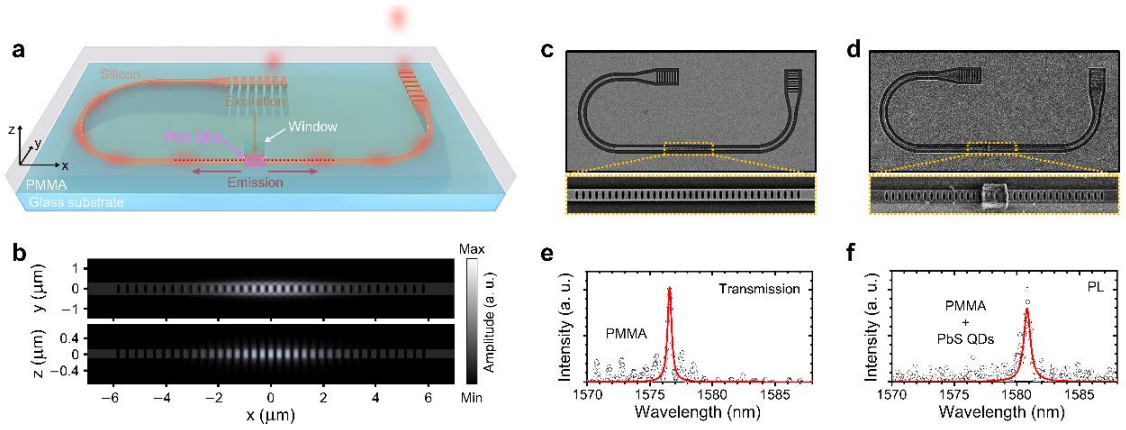

Figure 3.5 (a) Schematic of a deterministic positioning of PbS QDs on top of the nanobeam cavity mode using PMMA window and the emission propagation through the grating coupler. (b) Lateral and vertical mode profiles of the nanobeam cavity from the simulation. Shaded background structures represent the buried silicon nanobeam cavity in a glass. (c), (d) SEM images of the nanobeam cavity and orthogonal grating couplers before (c) and after (d) the PbS QDs integration, respectively. (e) (f) Transmission and PL spectra of the nanobeam cavity extracted from a grating coupler before (e) and after (f) the PbS QDs integration, respectively.

We designed the nanobeam cavity and the grating coupler using FDTD simulations. For lasing, stimulated emission needs to occur, and the gain from the active medium needs to exceed the cavity loss and material absorption. To achieve a low lasing threshold (~1 μW), we applied Gaussian modulation on the elliptical nanohole spacings and achieved a high Q-factor, greater than 10^5, from the simulation. We used a refractive index of the nanobeam cavity as 3.48, i.e., silicon, and the surrounding medium as 1.50, i.e., glass and PMMA, respectively. Figure 3.5b represents both lateral and vertical mode profiles of the confined electric field. We can see that the electric field is placed at the center of the nanobeam cavity with symmetry in both lateral and vertical directions due to the similar refractive index of the glass substrate and PMMA.

We implemented the simulated design to the physical device with following fabrication sequences: resist coating, electron-beam lithography, reactive ion etching, and resist removal. Scanning electron microscopy images of the fabricated nanobeam cavity, waveguide, and two orthogonal grating couplers are shown in Figure 3.5c. We put additional PMMA on top of the fabricated device and created a window at the center of the nanobeam cavity using electron-beam lithography. Then we spin-coated PbS QDs solution to place the QDs near the electric field

maximum of the nanobeam cavity. In the real device to measure the lasing phenomenon, we coated another PMMA and dried it at room temperature for about a day. However, to confirm the correct placement of PbS QDs, we dissolved a PMMA in acetone without sonication and measured SEM images of the PbS QDs with the device (Figure 3.5d). We can clearly observe the PbS QDs placed at the center of the nanobeam cavity following the shape of a rectangular PMMA window, even though some of the PbS QDs can be dissolved by acetone.

To characterize the fabricated device, we measured the transmission spectrum from one grating to another with a broadband light source. Figure 3.5e represents the transmission spectrum of one device that has a sharp peak at the cavity resonance. At this point, only PMMA is used to encapsulate the device and not the PbS QDs. From the spectrum, we can confirm that the resonant wavelength is around 1575 nm and the Q factor is about 4.4×10^3. After putting the PbS QDs solution on the PMMA window and encapsulating the whole device with another PMMA layer, we excited the PbS QDs directly from the top and measured the cavity-coupled emission extracted from one of the grating couplers. We can see that the resonant wavelength is now red shifted to ~1580 nm due to the higher refractive index of PbS QDs compared to PMMA, and the Q factor of the cavity is slightly reduced to about 3.0×10^3 due to the absorption from the QDs (Figure 3.5f).

We used a continuous-wave infrared laser to excite the PbS QDs placed at the center of the nanobeam cavity and measured the cavity-coupled PL extracted from the grating coupler. Here, we used a 1480 nm wavelength laser encountering a Stokes shift of about 75 nm. At the lasing regime, the gain from the active medium needs to be large enough to compensate for the cavity loss and material loss, and we can adjust the gain by changing the excitation power. Therefore, we adjust the power of the excitation laser to see the transition from spontaneous

emission, SE, to amplified spontaneous emission, ASE, and lasing.[197,198] Figure 3.6a represents the cavity-coupled PL spectra from one of the gratings while changing the excitation laser power from 0 to 6 μW. We notice the rapid growth of the PL intensity around an excitation power region of 2 to 3 μW, where the ASE occurs. On the other hand, observing a linewidth narrowing is one of the most promising features of the stimulated emission.[193,197–200] The linewidth is a more robust parameter than the measured intensity because the intensity is strongly affected by the slight misalignment. Figure 3.6b depicts a normalized PL spectra of the cavity-coupled PL at six different excitation powers, i.e., 0.3, 1.0, 1.6, 2.3, 3.0, 3.6 μW, and we notice linewidth of the emission is narrowing.

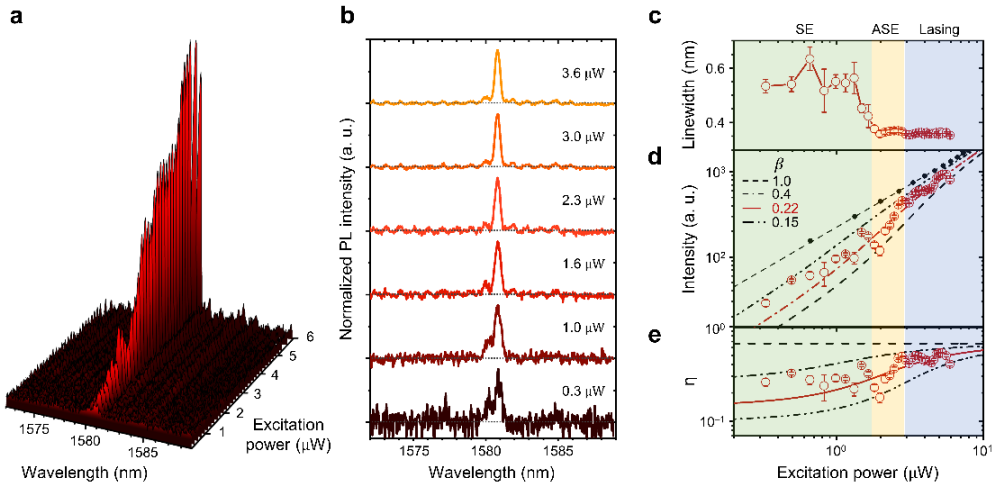

Figure 3.6 (a) Excitation power-dependent cavity-coupled PL spectra. (b) Normalized PL spectra of the PbS QDs coupled nanobeam cavity at six different excitation powers, i.e., 0.3, 1.0, 1.6, 2.3, 3.0, 3.6 μW. (c) Excitation power-dependent linewidth. (d) Excitation power-dependent PL peak intensity. The dotted lines indicate the calculation with respect to the different β values, 0.15, 0.22, 0.40, and 1.0. Black dots indicate the excitation power-dependent spontaneous emission for the PbS QDs uncoupled to the cavity. € Excitation power-dependent ratio between stimulated and spontaneous emission, η.

To explicitly analyze the spectra, we fitted the PL spectra at each excitation power with the Lorentzian equation. From the extracted parameters, we can divide the three excitation power regimes of SE, ASE, and lasing. First, and most importantly, the linewidth of the emission narrowed down significantly, about 0.2 nm or 30%, at the ASE regime due to the collective recombination of the excitons in PbS QDs (Figure 3.6c). By the definition of the stimulated

emission, multiple excitons having the same bandgap energy start to recombine simultaneously which results in the coherent emission. As a result of the collective recombination, we can observe the super-linear increase of PL intensity at the ASE regime, where the emission intensity grows more rapidly than the other regimes, i.e., SE and lasing. At higher excitation, collective recombination meets equilibrium, and the emission intensity with respect to the excitation power becomes linear again (Figure 3.6d). We analyze the intensity behavior of lasing according to the rate equation, Equation 3.2, resulting in the following relationship between the excitation power (P) and the PL intensity. Here, t_c value can be derived from the Q factor, $Q\lambda/2\pi c$, where the λ is resonant wavelength and c is the speed of light. In this case, the Q-factor is about 4.4×10^3 and λ is about 1580 nm which results in the t_c of about 3.69×10^{-12} sec. From the fitted graph, we can see that the measured data is matched when β is about 0.22, which is comparable to other nanolasers at the visible wavelength regime. Moreover, we can calculate the threshold excitation power for lasing by setting $aP = 1$ in Equation 3.2, and the result of 1.19 μW is also close to the starting point of the ASE regime.

On the contrary, spontaneous emission from the PbS QDs outside of the nanobeam cavity shows a clear linear relationship between the emission intensity and the excitation power. We integrated the PL intensities from 1579.5 to 1581.0 nm and displayed the relative intensities with respect to the excitation power as black dot in Figure 3.6d. Since the spontaneous emission without a cavity shows a clear linear relationship, we can define the ratio between the cavity-coupled PL intensity and cavity-uncoupled PL intensity (η) according to the excitation power. We can clearly observe the ratio, η, jumps from one level, ~0.15, to the upper level, ~0.5, during the ASE regime because of the super-linear increase of the cavity-coupled PL intensity (Figure 3.6e).

It is worth noting that the wavelength of the nanolaser can be adjusted by modulating the nanobeam cavity. By changing the size and period between elliptical holes, we can adjust the resonant wavelength of the nanobeam cavity. As a result, the cavity-coupled PL spectrum, i.e., lasing mode, has been adjusted accordingly. Figure 3.7a represents excitation power-dependent PL peak intensities of three different nanobeam cavities having three different resonant wavelengths. We fitted with Eq. (2) and the corresponding β and threshold power, $P_{threshold}$ are extracted as 0.24 and 0.89 μW, 0.88 and 2.15 μW, and 0.22 and 1.19 μW, respectively. Figure 3.7b represents the lasing spectra of three different devices, where the resonant wavelengths occur at around 1570, 1573, and 1580 nm.

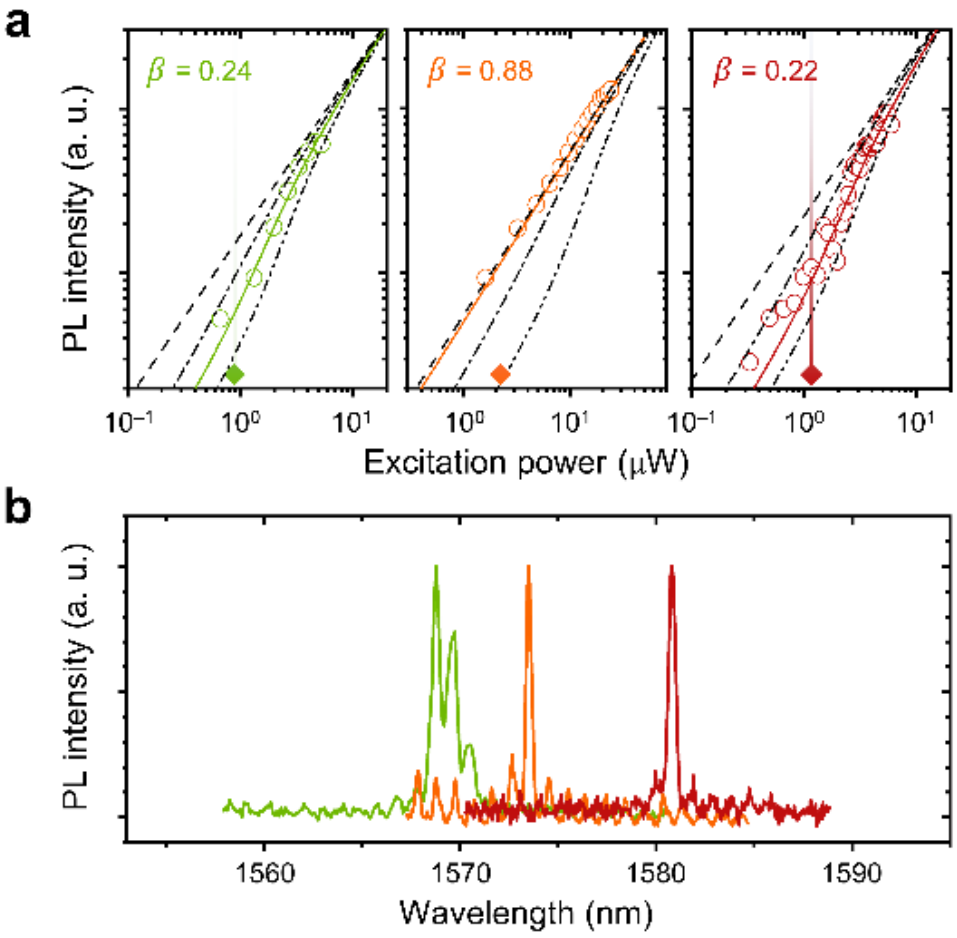

Figure 3.7 (a) Excitation power-dependent PL peak intensity and plot with different β values, 0.15, 0.40, and 1.0, for three different nanolaser devices coupled with PbS QDs. (b) PL spectra of three different nanolaser devices at lasing mode.

In conclusion, we have demonstrated a room-temperature continuous-wave lasing in a solution-processed silicon nanocavity for the first time, operating in the optical telecommunications window. We used commercially available solution-based PbS QDs as a gain medium and silicon nanobeam as a high-Q optical cavity. By patterning a PMMA window on top of the nanobeam cavity, and then spin-coating the PbS QDs, we can deterministically position the QDs at the cavity mode to enhance the coupling and minimize the propagation loss along the waveguide. We adjusted the power of the continuous-wave excitation laser from 0 to 6 μW, and characterized cavity-coupled PL emission changing from SE to ASE, and lasing – clarified by the linewidth narrowing, and super-linear intensity increment. We could also adjust the wavelength of the nanolaser by modulating the structural parameters of the nanobeam cavity and observe the lasing phenomena at three different wavelengths all in the optical telecommunications window. Our result can be a significant breakthrough as a scalable silicon nanolaser and paves the way for circuit-based universal photonic processors and interconnectors.

Chapter 4 Nanocavity-Enhanced Colloidal Quantum Dot Second-Harmonic Generation

The following chapter is based on a work written primarily by myself.[201]

Nonlinear optical phenomena are crucial to integrated photonics applications such as laser wavelength conversion and amplification and show promise as a mechanism for all-optical switching.[202–204] However, most foundry-compatible materials exhibit weak intrinsic nonlinearity, limiting their potential for low-power on-chip integration. Furthermore, a material's crystal structure must break inversion symmetry to have a finite second-order susceptibility. This precludes silicon and silicon compounds from second-order nonlinear optical processes such as second-harmonic generation (SHG), which finds applications in spectroscopy, frequency conversion, and frequency combs.[205–207] The emergence of low-dimensional materials has opened new routes to low-power nonlinear optics, especially second-order, owing to relaxed phase matching conditions and intrinsic broken inversion symmetries.[208,209] Among these materials, colloidal quantum dots (QDs) are a promising class of materials for on-chip nonlinear optics due to their tunability, strong nonlinearity, and ease of integration with photonic devices via recent developments in deterministic heterogeneous integration techniques.[6,54,55,58,210] Additionally, the large bulk second-order nonlinearities of II-VI elements commonly used in colloidal QDs, such as CdSe and CdS, indicates II-VI colloidal QDs hold promise for SHG.[211]

Nanocavity integration is critical to reducing the power thresholds for nonlinear optics by confining light in a small volume for an extended period.[212] Amongst low-dimensional materials, previous works have reported cavity-enhanced SHG from monolayers of transition metal

dichalcogenides,[213–215] while colloidal QDs remain unexplored for cavity-enhanced SHG. The most relevant reports have been limited to non-colloidal II-VI nanomaterials integrated plasmonic structures, with the highest cavity-enhancement factor ~1,000 in a CdS nanobelt coupled to an Au thin film.[29,216] Plasmonic structures are not favorable for low-power, scalable operations due to inherent absorptive losses from metal, and there are no reports of cavity-enhanced colloidal QD SHG in a dielectric nanocavity. Here, colloidal colossal CdSe/CdS QDs were integrated with a silicon nitride (SiN) nanobeam cavity, chosen for its high-quality factor, small mode volume, and compatibility with colloidal QD integration.[93] By comparing the colossal QD SHG generated from the cavity to that from QDs on an unpatterned substrate, we estimate a cavity-enhancement factor of ~ 3,040.

The nanobeam cavity, as depicted in Figure 4.1a, was designed according to previously established methods.[35] The cavity geometry consisted of a 330 nm thick and 650 nm wide SiN waveguide on buffer oxide with poly(methyl methacrylate) (PMMA) encapsulation. The cavity region was comprised of a one-dimensional array of elliptical holes with a major radius of 300 nm, a minor radius of 60 nm, and a period of 234 nm. Starting from the center, the period of the holes was quadratically tapered to 243 nm over 10 periods on both sides to gradually introduce the mirror region. An additional 20 holes of the same period were added to either side to increase the cavity mirror reflectivity. This design was verified in the Lumerical finite-difference time-domain (FDTD) solver and resulted in a theoretical quality factor, Q, of 40,000 and mode volume 2.9 $(\lambda/n)^3$, where λ and n are the resonant wavelength and refractive index of SiN, respectively. Figure 4.1b shows the simulated electric-field intensity profile of the targeted transverse-electric polarized cavity mode. This design was fabricated using 100 keV electron-

beam lithography and a fluorine-based dry etch chemistry according to previous protocols.[153] The cavity is coupled to a waveguide and grating couplers to facilitate characterization.

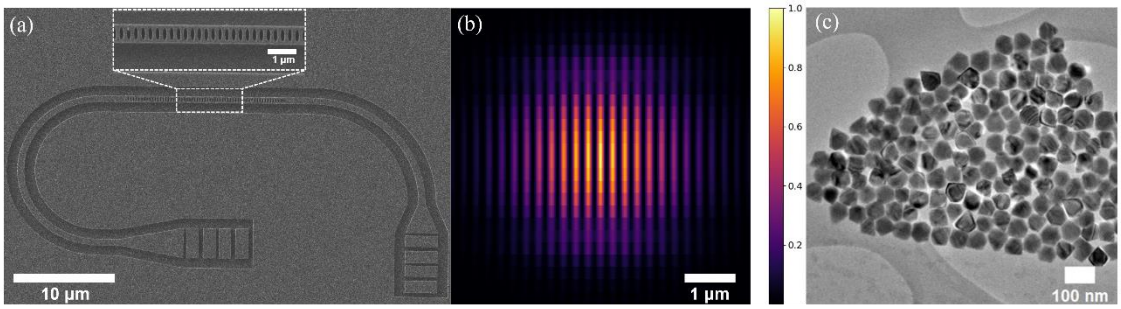

Figure 4.1 (a) SEM of a nanobeam cavity. Inset: magnified SEM of the cavity region. (b) Finite-difference time-domain simulation of the nanobeam cavity mode electric field intensity, $|E|^2$. (c) Transmission electron micrograph of the colossal CdSe/CdS QDs used in this work.

Colossal core/shell CdSe/CdS colloidal QDs were synthesized using a previously reported method.[56] First, wurtzite CdSe QD cores with an average particle diameter of 3.5 nm were prepared following an established method, where particle growth was terminated 45 seconds after the injection of the Se solution.[22] The QDs were purified by centrifugation twice using hexane as the solvent and methyl acetate as the antisolvent, then stored in hexane. The QD cores were shelled with 80 monolayers (MLs) of CdS using the stepwise shelling method in increments of 30, 50, and 80 MLs, without purification between steps.[56] The final product, CdSe QDs shelled with 80 CdS MLs, was purified by centrifugation with hexane to remove small CdS particles and unreacted precursors and was stored in hexane. The colossal QDs' morphology was analyzed by transmission electron microscopy, as depicted in Figure 4.1c, which indicates a hexagonal diamond shape with average height of 72 nm. Colossal QDs were integrated with the nanobeam cavities by drop-casting a solution containing many QDs on the cavity chip. After allowing the solution to dry, the chip was spin coated with PMMA to encapsulate the cavities cladded with colossal QDs.

The nanobeam cavity was first characterized using a confocal microscope setup. In the experimental geometry used herein, a pump laser was shined on one grating coupler and the light scattered out of plane was collected from the cavity region, all using a 40x (NA 0.6) objective lens. Figure 4.2a depicts the cavity spectrum measured from the nanobeam cavity considered in the rest of this work. By fitting to a Lorentzian lineshape, the cavity has a resonant wavelength 808.2 nm and $Q \sim 4{,}500$. Next, the SHG response of the colossal QDs was collected by shining a Ti:sapphire ultrafast pulsed pump laser (Spectra-Physics Tsunami HP) on an unpatterned section of the chip. By comparing the pump laser spectrum, Figure 4.2b, and the collected colossal QD SHG spectrum, Figure 4.2c, it is evident that there is a strong SHG response from the colossal QD film as the SHG central wavelength, linewidth, and Gaussian profile are all consistent with SHG pumped by the Ti:sapphire laser. Here, the average pump power was 30 mW as measured in front of the objective lens.

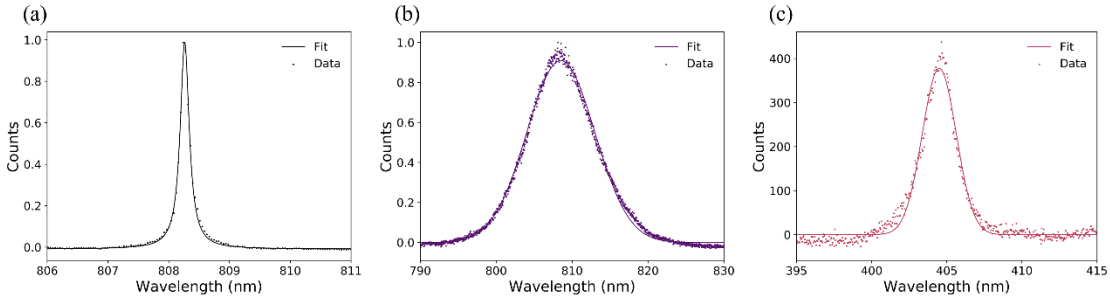

Figure 4.2 (a) Transmission spectrum of the nanobeam cavity as measured by shining the pump laser on a grating coupler and measuring the scattered light from the top. The fundamental mode has a resonant wavelength of 808.2 nm and linewidth 0.18 nm as determined by fitting to a Lorentzian lineshape. (b) Spectrum of the ultrafast pump laser centered at 808.7 nm with a Gaussian lineshape. (c) SHG spectrum of uncoupled QDs with 30 mW pump power centered at 404.4 nm. The central wavelength, linewidth, and Gaussian lineshape are consistent with SHG.

The cavity-coupled QD SHG was characterized using the same experimental geometry as before by shining the Ti:sapphire pump laser on a grating coupler and collecting the cavity-coupled QD SHG signal emitted out of plane. Figure 4.3a depicts a representative cavity-coupled QD SHG spectrum. The spectrum shows both Gaussian and Lorentzian components as

previously observed.[213] The Gaussian part is attributed to background uncoupled colossal QD SHG, and the Lorentzian part is attributed to the actual cavity-coupled QD SHG. Fitting to the Lorentzian component reveals the cavity mode is centered at 404.1 nm with a similar linewidth to the fundamental mode, which is consistent with cavity-coupled SHG.[214] The power series of the cavity-coupled QD SHG spectrum as a function of pump power is depicted in Figures 4.3b and 4.3c. In Figure 4.3c, the integrated counts are calculated by integrating only the Lorentzian part of each spectrum. The error bars were calculated according to one standard deviation error in each of the fits. The integrated counts follow a quadratic dependence on the pump power, as expected for a second-order nonlinear process.[217]

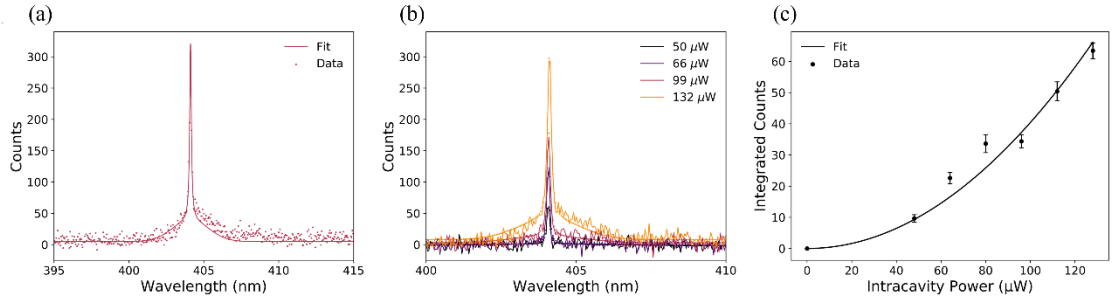

Figure 4.3 (a) Representative QD-cavity SHG spectrum. The spectrum is fitted to the sum of Gaussian and Lorentzian lineshapes to account for the background uncoupled SHG and cavity-coupled SHG, respectively. The cavity mode is centered at 404.1 nm. The Lorentzian lineshape and central wavelength confirm this signal originates from the fundamental cavity mode. (b) Plot of the QD-cavity SHG spectrum and fit with different intracavity powers. (c) Power series of the QD-cavity SHG intensity versus intracavity power as measured by integrating the Lorentzian portion of the spectral fitting at each pump power. Error bars were obtained from one standard deviation error of each Lorentzian fit. The power series follows a quadratic trend.

To calculate the strength of cavity enhancement of the colossal QD SHG, an estimate of the pump laser power coupled to the cavity was first calculated following a previously established method.[214] The intracavity power, P_{cav}, is calculated as:

$$P_{cav} = P \times t_w \times g \times f \tag{4.1}$$

where P is the nominal pump laser power, t_w is the coupling efficiency of the waveguide to the cavity, g is the grating coupler efficiency, and f is the spectral overlap of the cavity mode and

pump laser. From input-output relations, $t_w = 0.35$, whereas FDTD simulations give $g = 0.11$, and the overlap integral $f = 0.087$. The cavity enhancement factor, E, is then given as:

$$E = \frac{I_{cav}}{P_{cav}^2}\frac{P_{ref}^2}{I_{ref}} \tag{4.2}$$

where, respectively, I_{cav} and I_{ref} are the integrated counts for the cavity-coupled QD SHG and reference colossal QDs on an unpatterned section of the cavity chip, and P_{cav} and P_{ref} are the corresponding pump laser powers. By comparing the cavity-coupled QD SHG integrated counts for a nominal pump laser power of 40 mW (Figure 4.3c, $I_{cav} = 63$, $P_{cav} = 132$ μW) to that of the uncoupled colossal QD SHG (Figure 4.2c, $I_{ref} = 1070$, $P_{ref} = 30$ mW), the enhancement factor E ~ 3,040. This calculation assumes maximum experimental collection efficiency of the cavity-QD SHG, so it is therefore a lower bound of the true enhancement factor.

CdSe/CdS colloidal colossal QDs were integrated with a SiN nanobeam cavity and ~3,040 times cavity-enhancement of the intrinsic colossal QD SHG was demonstrated. This is, to the best of our knowledge, the first report of cavity-enhanced colloidal QD SHG from coupling to a dielectric nanocavity, which is expected to be more scalable than plasmonic devices. Furthermore, it has been demonstrated recently that colossal QDs can be deterministically integrated with photonic devices.[58] Future works could improve on this result by modifying both the QDs and the cavity design. Varying the QD core size is expected to have a trivial enhancement of the intrinsic QD SHG and other II-VI materials may offer stronger second-order susceptibilities.[218,26] Doubly-resonant cavities covering the fundamental and SHG wavelengths would further increase the cavity enhancement of the QD SHG.[219] This work is a step forward for low-power on-chip nonlinear optics via integration of novel materials.

Chapter 5 Near-Visible Topological Edge States in a Silicon Nitride Platform

The following chapter is based on a work written primarily by myself.[220]

Over the last two decades, topological photonics has emerged as an attractive platform to realize exotic physical models. Photonic analogues to the integer, spin, and valley quantum Hall effects as well as the Su-Schrieffer-Heeger model have all been demonstrated using arrays of ring resonators [221–223]. However, there are few demonstrations of such effects in photonic platforms operating at (near) visible wavelengths, primarily because they are often based on silicon photonics, which absorbs light of wavelengths below ~1000 nm. A few existing demonstrations in the visible regime have mostly been limited to topological photonic crystals and arrays of waveguides, which may not provide as versatile a platform as coupled ring resonators [224–226]. Implementing topological photonics in the (near) visible regime is attractive for two reasons. One, it is usually necessary to measure the spatial distribution of photons to fully characterize the topological nature of the system. In the infrared, this is hampered by poor imaging technology. In the (near) visible, one can employ silicon-based cameras with much higher resolution (larger number and smaller size of pixels). Two, (near) visible wavelength operation opens access to a large library of quantum emitters including two-dimensional semiconductors, colloidal semiconductor quantum dots, and thermal atomic vapors that are compatible with nanophotonics fabricated from CMOS-compatible materials [35,93,227]. Such emitters can extend the functionality of topological photonics by introducing single photon sources, optical gain, and large nonlinearities [23,24,28,48,213,228]. This would push topological photonics in new directions by

expanding access to non-Hermitian and nonlinear topological regimes [229–231]. Furthermore, recent demonstrations of visible frequency combs [232,233] and infrared topological frequency combs [234,235] highlights the potential of topological photonics for harnessing rich microcomb physics in the (near) visible regime.

In this work, topological edge states at near-visible wavelengths were demonstrated in a system consisting of a two-dimensional lattice of coupled silicon nitride (SiN) ring-resonators. Like previous demonstrations, a photonic analogue to the integer quantum Hall (IQH) Hamiltonian was implemented by introducing a synthetic magnetic field for photons that mimics the effect of a uniform out-of-plane magnetic field on charged particles confined to a two-dimensional lattice [221,236]. Such a system in solid-state is expected to show edge states with topological protection against disorder [237]. Indeed, edge states were observed in the SiN ring-resonator lattice that were robust over a broad spectral range and against fabrication disorder. This system provides a powerful platform for further study of exotic materials systems as a photonic analogue in the near-visible regime. Importantly, this wavelength regime could enable low-power optical nonlinearity through integration of quantum emitters [6,238].

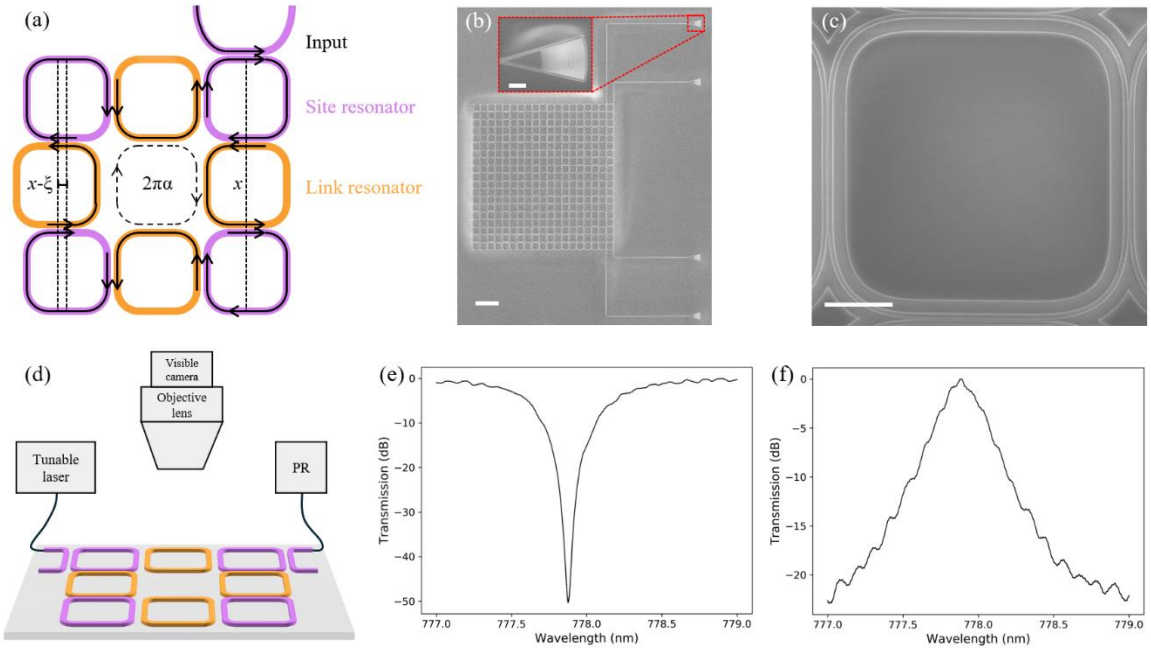

Figure 5.1 (a) Schematic of a single plaquette where the site resonators and link resonators are denoted in purple and orange, respectively. The black arrows trace the path of light launched from the input waveguide and traveling clockwise around the lattice. A photon traveling in a complete clockwise loop around the plaquette accumulates a phase shift $2\pi\alpha$. Each column across the lattice is increasingly horizontally translated by ζ such that the total path length difference gives a phase shift of $\pi/2$. (b) Scanning electron micrograph (SEM) of an example 10x10 ring-resonator array. Light is coupled to and from the lattice using waveguides coupled to four separate apodized grating couplers. Inset: zoomed-in micrograph of an apodized grating coupler. The scale bars for the full-size image and the inset are 100 μm and 10 μm, respectively. (c) SEM of a site-ring situated in a larger array. The scale bar is 10 μm. (d) Schematic of the experimental set-up. A tunable laser launches light into the chip, and the transmission spectrum is measured by a photoreceiver (PR). The spatial distribution of photons is monitored by a 10x objective lens and visible camera. (e-f) Transmission drop (e) and through (f) spectra for a single representative site resonator used in the array.

The topological system in this work, depicted in Figure 5.1a, is a two-dimensional square lattice of ring-resonators coupled to each other via an interspersed array of detuned "link-ring" resonators. A carefully chosen shift in the position of certain link-rings introduces a position and direction dependent optical path length difference, simulating the direction-dependent phase produced by the magnetic field in the IQH model [221,239,240]. As a result, the photons in the lattice of ring-resonators experience a synthetic magnetic field and obey the IQH tight-binding Hamiltonian:

$$H = \sum_{m} \omega_0 \, a_m^\dagger a_m - \sum_{m,n} J_{m,n} \left(a_m^\dagger a_n e^{-i\varphi_{m,n}} + a_n^\dagger a_m e^{+i\varphi_{m,n}} \right) \tag{5.1}$$

where $a_m^\dagger$ is the photon creation operator at site $m = (m_x, m_y)$, $J_{m,n}$ is the hopping rate between sites m, n, which has non-zero value for only nearest-neighbor sites in the lattice, and $\varphi_{m,n}$ is the hopping phase between sites m, n such that a photon traveling in a complete loop around a plaquette experiences a direction-dependent phase shift $\varphi = \pm\pi/2$.

The resulting spectrum consists of two edge bands separated by a bulk band. Each edge band has a set of topological edge states, confined to the edge of the lattice and propagating either clockwise (CW) or counterclockwise (CCW) around the lattice, depending on the band. Given that time-reversal symmetry is unbroken in the lattice, the lattice itself would simulate the quantum spin Hall Hamiltonian with the edge state propagation direction acting as a pseudospin degree of freedom. In practice, however, only one pseudospin is excited at a time, which results in pseudo time-reversal symmetry breaking so this lattice simulates the IQH Hamiltonian. Furthermore, these edge modes exhibit a linear dispersion relation in contrast with the modes of the bulk band, which are not spatially confined and do not have a well-defined momentum.

The two-dimensional lattices of coupled ring-resonators were designed for 220 nm thick stoichiometric SiN on a SiO_2/Si substrate without any top cladding. The waveguide width was set to 600 nm such that the waveguides confine only a single transverse-electric mode at the target near-visible wavelength of 780 nm. This operating wavelength was chosen due to the lasers available and can be readily extended to the visible spectrum. The resonators were implemented in a racetrack geometry wherein coupling between adjacent resonators occurs over straight sections and the 90° bends occur at the corners. This geometry was chosen to ensure strong optical mode overlap between neighboring resonators. For the lattice in this work, the coupling length, coupling gap, and bending radius were chosen to be 12 μm, 175 nm, and 12 μm,

respectively. Light was coupled to and from the chip using fully etched apodized grating couplers, which were designed to maximize the coupling efficiency while minimizing backscattering[241].

The pattern was transferred to the SiN using electron-beam lithography with ZEP520A positive-tone resist in conjunction with a low-pressure, low gas flow rate, fluorine-based plasma etch recipe designed to minimize sidewall roughness. All components of the devices, including grating couplers, were fully etched in the same step. Figure 5.1b depicts a scanning electron micrograph of an example 10×10 lattice. Light was coupled to and from the lattice via a pair of waveguides in an add-drop configuration that allowed for complete spectral characterization. On the same chip, a single site resonator associated with each two-dimensional lattice was also fabricated to characterize the component site-ring resonators, as depicted in Figure 5.1c.

To characterize the ring-resonator lattice, an array of optical fibers was utilized in conjunction with a tunable-wavelength laser (New Focus TLB-6712-P) and photoreceiver (New Focus 2051-FS) (Figure 5.1d). This enabled measurement of the transmission spectra in both CW and CCW input configurations without altering the alignment of the chip relative to the excitation and collection pathways. In parallel, the intensity distribution of photons in the lattice was measured by monitoring scattering losses in the waveguides and ring-resonators on a CMOS camera (Allied Vision Prosilica GT 1930; 1936×1216 pixels) with a 10x (NA 0.28) objective lens. This experimental scheme was first used to characterize the extrinsic waveguide-resonator coupling rate and the intrinsic resonator decay rate for a single resonator $J \approx 52$ GHz and $\kappa_{in} \approx 9.4$ GHz, respectively (Figures 5.1e and 5.1f). From these measurements, the intrinsic quality-factor is estimated to be Q ≈ 40,000.

Figure 5.2a depicts the transmission spectrum for the 8×8 ring-resonator lattice with CW site-ring input. The spectral ranges highlighted in purple and orange correspond to short and long edge states, respectively. These are evident in the intensity distribution of light scattered in the lattice (Figures 2b and 2c). Here, the short and long edge states are defined relative to the placements of the input waveguides and correspond to CW and CCW propagation around the lattice, respectively. The edge states propagate starting from the input waveguide at the top of the lattice and couple to the output waveguide at the bottom, which extinguishes the edge state. Two transmission peaks corresponding to two edge states are split by approximately $2J$ as expected for this system [237]. The short edge state has a higher transmission efficiency compared to the long one due to the shorter propagation distance hence less loss. Each of these edge states are well-confined to the edges, and the long edge state tightly routes around each corner owing to topologically protected transport.

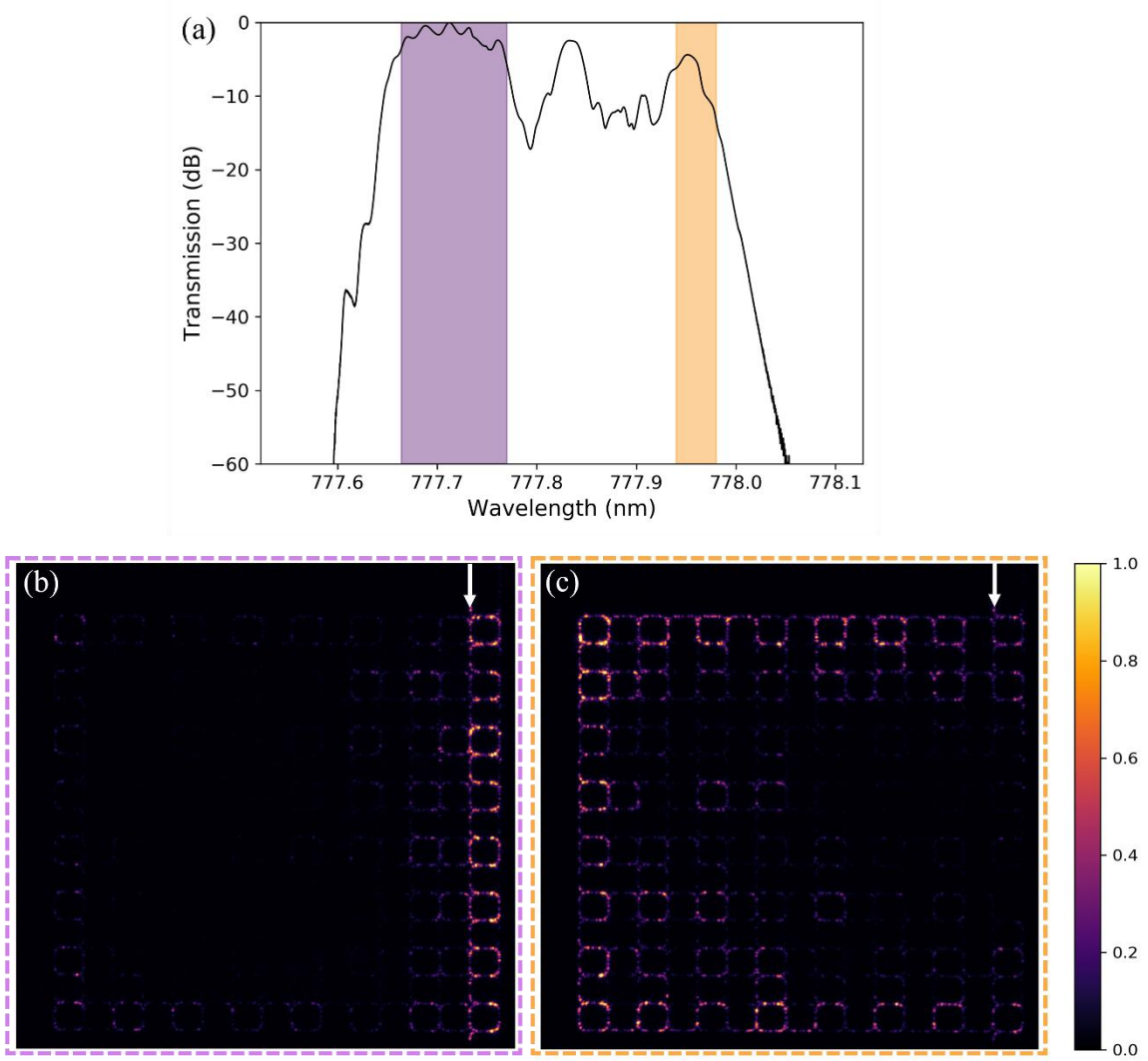

Figure 5.2 (a) Measured transmission spectrum of the 8x8 ring-resonator array with CW input. The purple and orange regions highlight the approximate spectral regions of the short and long edge states, respectively. (b, c) Optical images of the spatial distribution of light scattered in the lattice at 777.720 nm (b) and 777.961 nm (c). Here, the short and long edges are defined with respect to the location of the input waveguide. (b-c) The white arrows indicate the locations of the inputs.

These measurements were repeated for the same spectral range but instead with CCW site-ring input. This corresponds to pumping the lattice with light of an opposite pseudo-spin. Since the synthetic magnetic field in this photonic system does not break time-reversal symmetry, this reverses the behavior as compared to CW site-ring input. This is evident in the transmission spectrum depicted in Figure 5.3a wherein the purple and orange highlighted regions still correspond to short and long edge states, respectively, but the spectral locations of each edge

state are flipped relative to the central bulk state peak. The light again tightly routes around each corner and remains close to the edges (Figures 5.3b and 5.3c). In each case, some light leaks into the bulk owing to scattering at the lattice corners and fabrication imperfections such as sidewall roughness and variation in the waveguide width or gap. This is in line with experimental and theoretical results in previous works [221,236]. Fabrication imperfections are furthermore responsible for the discrepancy in localizations between CW and CCW site-ring inputs, since under time-reversal symmetry it is expected that the photon distributions should be identical. However, we emphasize that the topological edge states still demonstrate remarkable confinement as compared to true bulk states: for both input directions, each of the edge states maintains a similarity of its intensity distribution over a much broader bandwidth as compared to the bulk state.

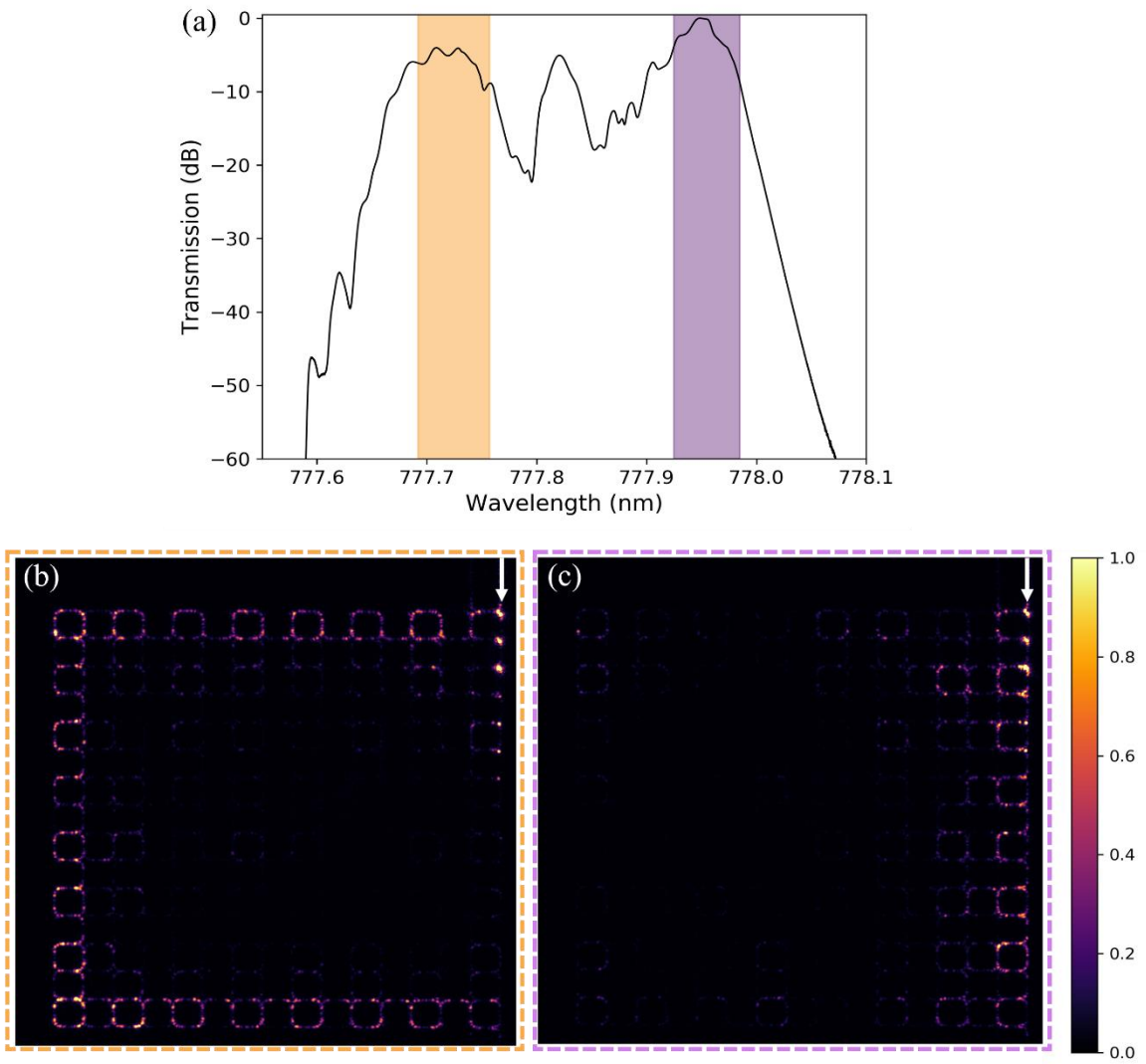

Figure 5.3 (a) Measured transmission spectrum of the 8x8 ring-resonator array with CCW input. The orange and purple regions highlight the approximate spectral regions of the long and short edge states, respectively. (b, c) Optical images of the spatial distribution of light scattered in the lattice at 777.739 nm (b) and 777.982 nm (c). (b-c) The white arrows indicate the locations of the inputs.

Additionally, an otherwise identical 8×8 ring-resonator array with an intentionally removed site resonator was fabricated on the same chip (Figure 5.4a). This is an extreme case of disorder and serves to illustrate the effect of topological protection in the edge states. Light was coupled into the ring-resonator lattice with CW site-ring input at the short edge band and tightly routed around the missing resonator with minimal scattering into the bulk over a bandwidth of ~71 pm (35 GHz) (Figures 5.4b-d). The bandwidth was established by monitoring the lattice

while tuning the input laser wavelength and noting the extreme wavelengths where the topological protection failed. This bandwidth is comparable with the unperturbed short edge band with CW site-ring input in Figure 5.2 and further confirms that the edge states in this system enjoy topological protection against disorder.

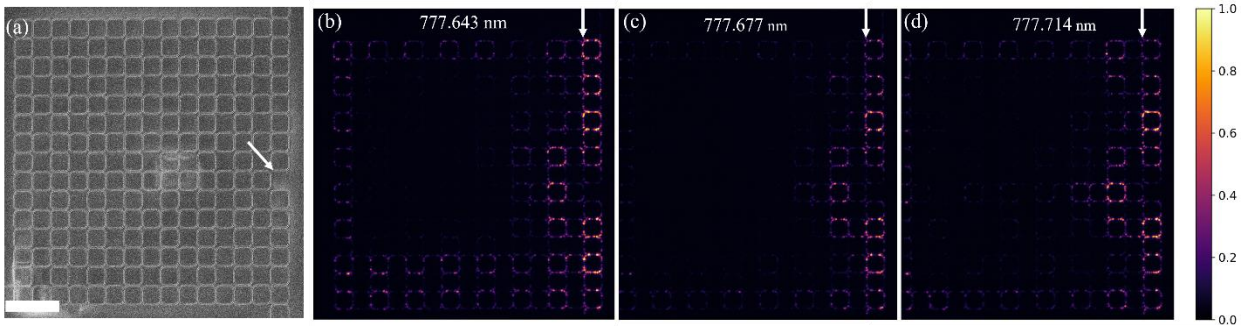

Figure 5.4 (a) Scanning electron micrograph of the 8×8 ring-resonator array with an intentionally removed site resonator. The white arrow indicates the location of the missing resonator. The scale bar is 100 μm. (b-d) Optical images of the spatial distribution of light scattered in the lattice at 777.643 nm (b), 777.677 nm (c), and 777.714 nm (d). The light in the short edge state tightly rounds around the defect with minimal scattering into the bulk. (b-d) The white arrows indicate the locations of the inputs.

Topological edge states at near-visible wavelengths were demonstrated in a two-dimensional lattice of coupled SiN ring-resonators. This platform leveraged near-visible regime imaging technology to capture high-resolution images of the distribution of scattered light in the system, illustrating the imaging advantage of the near-visible regime. If the scattered light is coherent, one could use high-resolution (near) visible regime imaging to obtain the phase information of the photonic states in each resonator. This could enable phase measurements of the topological states, which have so far been elusive in any platform. It is expected that fabrication disorder will mar the global topological order, an effect compounded by the shorter length of near-visible photonics as compared to infrared [222]. Therefore, process control is critical to achieve visible topological edge states in experiments, for which we developed high-quality SiN e-beam lithography and etching processes. Moreover, extension of topological photonics into near-visible wavelengths can enable visible wavelength topological frequency combs and

paves the way for studies of many-body systems mimicked by topological photonics coupled to visible wavelength emitters. In particular, this latter effort could benefit greatly from recent advances in deterministic positioning of colloidal emitters [54,55,93].

Chapter 6 Outlook

To conclude, this thesis covered the heterogeneous integration of colloidal QDs with photonic devices including scalable deterministic positioning techniques, on-chip nanolasers and second-harmonic generation, and near-infrared topological photonics. Some opportunities inspired by this thesis:

- Further experiments on cavity integration of colloidal QDs with different kinds of cavities. For example, bound state in the continuum (BIC) cavities are exceptionally high-Q metasurface-type cavities that have proven to enable low-power nonlinear optics[242] plus spectral and angular filtering.[243] These cavities use tunable symmetry breaking to controllably enable coupling of a previously dark mode to free space, giving fine control of the cavity Q-factor.[244] BIC cavities have remained unexplored for coupling single colloidal QDs for cavity-enhanced single photon emitters. Inverse-designed, topologically optimized cavities with ultrahigh confinement are also promising for colloidal QD coupling,[245] and single QD coupling plus Purcell enhancement should be explored. This effort would especially benefit from high-precision EHDIJ printing of single colloidal QDs.
- Colloidal QD integration with visible-wavelength topological photonics. The majority of topological photonics demonstrations focus on purely linear topological Hamiltonians such as the integer quantum Hall effect.[221] However, integrating gain material has been shown to enable exploration of nonlinear Hamiltonians such as the fractional quantum Hall effect.[229,230] Again, deterministic positioning to place colloidal QDs would be useful to integrate gain material only on select resonator sites to match the appropriate Hamiltonian and minimize extra losses.

Bibliography

(1) Rogers, C.; Piggott, A. Y.; Thomson, D. J.; Wiser, R. F.; Opris, I. E.; Fortune, S. A.; Compston, A. J.; Gondarenko, A.; Meng, F.; Chen, X.; Reed, G. T.; Nicolaescu, R. A Universal 3D Imaging Sensor on a Silicon Photonics Platform. *Nature* **2021**, *590* (7845), 256–261. https://doi.org/10.1038/s41586-021-03259-y.

(2) Qiang, X.; Zhou, X.; Wang, J.; Wilkes, C. M.; Loke, T.; O'Gara, S.; Kling, L.; Marshall, G. D.; Santagati, R.; Ralph, T. C.; Wang, J. B.; O'Brien, J. L.; Thompson, M. G.; Matthews, J. C. F. Large-Scale Silicon Quantum Photonics Implementing Arbitrary Two-Qubit Processing. *Nature Photon* **2018**, *12* (9), 534–539. https://doi.org/10.1038/s41566-018-0236-y.

(3) Arrazola, J. M.; Bergholm, V.; Brádler, K.; Bromley, T. R.; Collins, M. J.; Dhand, I.; Fumagalli, A.; Gerrits, T.; Goussev, A.; Helt, L. G.; Hundal, J.; Isacsson, T.; Israel, R. B.; Izaac, J.; Jahangiri, S.; Janik, R.; Killoran, N.; Kumar, S. P.; Lavoie, J.; Lita, A. E.; Mahler, D. H.; Menotti, M.; Morrison, B.; Nam, S. W.; Neuhaus, L.; Qi, H. Y.; Quesada, N.; Repingon, A.; Sabapathy, K. K.; Schuld, M.; Su, D.; Swinarton, J.; Száva, A.; Tan, K.; Tan, P.; Vaidya, V. D.; Vernon, Z.; Zabaneh, Z.; Zhang, Y. Quantum Circuits with Many Photons on a Programmable Nanophotonic Chip. *Nature* **2021**, *591* (7848), 54–60. https://doi.org/10.1038/s41586-021-03202-1.

(4) Pfeiffer, M. H. P.; Kordts, A.; Brasch, V.; Zervas, M.; Geiselmann, M.; Jost, J. D.; Kippenberg, T. J. Photonic Damascene Process for Integrated High-Q Microresonator Based Nonlinear Photonics. *Optica* **2016**, *3* (1), 20. https://doi.org/10.1364/OPTICA.3.000020.

(5) Kala, A.; Sharp, D.; Choi, M.; Manna, A.; Deshmukh, P.; Veetil, V. K.; Menon, V.; Pelton, M.; Waks, E.; Majumdar, A. Opportunities and Challenges of Solid-State Quantum Nonlinear Optics. arXiv November 10, 2024. https://doi.org/10.48550/arXiv.2411.06630.

(6) Chen, Y.; Sharp, D.; Saxena, A.; Nguyen, H.; Cossairt, B. M.; Majumdar, A. Integrated Quantum Nanophotonics with Solution-Processed Materials. *Adv Quantum Tech* **2021**, 2100078. https://doi.org/10.1002/qute.202100078.

(7) Churaev, M.; Wang, R. N.; Riedhauser, A.; Snigirev, V.; Blésin, T.; Möhl, C.; Anderson, M. H.; Siddharth, A.; Popoff, Y.; Drechsler, U.; Caimi, D.; Hönl, S.; Riemensberger, J.; Liu, J.; Seidler, P.; Kippenberg, T. J. A Heterogeneously Integrated Lithium Niobate-on-Silicon Nitride Photonic Platform. *Nat Commun* **2023**, *14* (1), 3499. https://doi.org/10.1038/s41467-023-39047-7.

(8) Park, H.; Zhang, C.; Tran, M. A.; Komljenovic, T. Heterogeneous Silicon Nitride Photonics. *Optica* **2020**, *7* (4), 336. https://doi.org/10.1364/OPTICA.391809.

(9) Rosser, D.; Fryett, T.; Saxena, A.; Ryou, A.; Majumdar, A. High-Precision Local Transfer of van Der Waals Materials on Nanophotonic Structures. *Opt. Mater. Express* **2020**, *10* (2), 645. https://doi.org/10.1364/OME.383255.

(10) Grotevent, M. J.; Hail, C. U.; Yakunin, S.; Dirin, D. N.; Thodkar, K.; Borin Barin, G.; Guyot-Sionnest, P.; Calame, M.; Poulikakos, D.; Kovalenko, M. V.; Shorubalko, I. Nanoprinted Quantum Dot–Graphene Photodetectors. *Advanced Optical Materials* **2019**, *7* (11), 1900019. https://doi.org/10.1002/adom.201900019.

(11) Liu, Y.; Li, F.; Xu, Z.; Zheng, C.; Guo, T.; Xie, X.; Qian, L.; Fu, D.; Yan, X. Efficient All-Solution Processed Quantum Dot Light Emitting Diodes Based on Inkjet Printing

Technique. *ACS Appl. Mater. Interfaces* **2017**, *9* (30), 25506–25512. https://doi.org/10.1021/acsami.7b05381.
(12) Pelton, M. Modified Spontaneous Emission in Nanophotonic Structures. *Nature Photon* **2015**, *9* (7), 427–435. https://doi.org/10.1038/nphoton.2015.103.
(13) Feynman, R. There's Plenty of Room at the Bottom. In *Feynman and computation*; CRC Press, 2018; pp 63–76.
(14) Griffiths, D. J. *Introduction to Quantum Mechanics*, Second edition.; Cambridge University Press: Cambridge, 2017.
(15) Von Klitzing, K. The Quantized Hall Effect. *Rev. Mod. Phys.* **1986**, *58* (3), 519–531. https://doi.org/10.1103/RevModPhys.58.519.
(16) Ekimov, A. I.; Efros, L.; Onushchenko, A. A. QUANTUM SIZE EFFECT IN SEMICONDUCTOR MICROCRYSTALS.
(17) Murray, C. B.; Norris, D. J.; Bawendi, M. G. Synthesis and Characterization of Nearly Monodisperse CdE (E = Sulfur, Selenium, Tellurium) Semiconductor Nanocrystallites. *J. Am. Chem. Soc.* **1993**, *115* (19), 8706–8715. https://doi.org/10.1021/ja00072a025.
(18) Baskoutas, S.; Terzis, A. F. Size-Dependent Band Gap of Colloidal Quantum Dots. *Journal of Applied Physics* **2006**, *99* (1), 013708. https://doi.org/10.1063/1.2158502.
(19) Bhattacharya, P. *Semiconductor Optoelectronic Devices*; Prentice Hall: Englewood Cliffs, NJ, 1994.
(20) *Quantum Dot Market Size, Share, Industry Report 2030*. MarketsandMarkets. https://www.marketsandmarkets.com/Market-Reports/quantum-dots-qd-market-694.html (accessed 2025-03-12).
(21) *Nobel Prize in Chemistry 2023*. NobelPrize.org. https://www.nobelprize.org/prizes/chemistry/2023/summary/ (accessed 2025-03-12).
(22) Cirillo, M.; Aubert, T.; Gomes, R.; Van Deun, R.; Emplit, P.; Biermann, A.; Lange, H.; Thomsen, C.; Brainis, E.; Hens, Z. "Flash" Synthesis of CdSe/CdS Core–Shell Quantum Dots. *Chem. Mater.* **2014**, *26* (2), 1154–1160. https://doi.org/10.1021/cm403518a.
(23) Utzat, H.; Sun, W.; Kaplan, A. E. K.; Krieg, F.; Ginterseder, M.; Spokoyny, B.; Klein, N. D.; Shulenberger, K. E.; Perkinson, C. F.; Kovalenko, M. V.; Bawendi, M. G. Coherent Single-Photon Emission from Colloidal Lead Halide Perovskite Quantum Dots. *Science* **2019**, *363* (6431), 1068–1072. https://doi.org/10.1126/science.aau7392.
(24) Proppe, A. H.; Berkinsky, D. B.; Zhu, H.; Šverko, T.; Kaplan, A. E. K.; Horowitz, J. R.; Kim, T.; Chung, H.; Jun, S.; Bawendi, M. G. Highly Stable and Pure Single-Photon Emission with 250 Ps Optical Coherence Times in InP Colloidal Quantum Dots. *Nat. Nanotechnol.* **2023**, *18* (9), 993–999. https://doi.org/10.1038/s41565-023-01432-0.
(25) Guzelturk, B.; Kelestemur, Y.; Gungor, K.; Yeltik, A.; Akgul, M. Z.; Wang, Y.; Chen, R.; Dang, C.; Sun, H.; Demir, H. V. Stable and Low-Threshold Optical Gain in CdSe/CdS Quantum Dots: An All-Colloidal Frequency Up-Converted Laser. *Adv. Mater.* **2015**, *27* (17), 2741–2746. https://doi.org/10.1002/adma.201500418.
(26) Zielinski, M.; Oron, D.; Chauvat, D.; Zyss, J. Second-Harmonic Generation from a Single Core/Shell Quantum Dot. *Small* **2009**, *5* (24), 2835–2840. https://doi.org/10.1002/smll.200900399.
(27) Jun, S.; Kim, J.; Choi, M.; Kim, B. S.; Park, J.; Kim, D.; Shin, B.; Cho, Y.-H. Ultrafast and Bright Quantum Emitters from the Cavity-Coupled Single Perovskite Nanocrystals. *ACS Nano* **2024**, *18* (2), 1396–1403. https://doi.org/10.1021/acsnano.3c06760.

(28) Yang, Z.; Pelton, M.; Fedin, I.; Talapin, D. V.; Waks, E. A Room Temperature Continuous-Wave Nanolaser Using Colloidal Quantum Wells. *Nat Commun* **2017**, *8* (1), 143. https://doi.org/10.1038/s41467-017-00198-z.
(29) Liu, X.; Zhang, Q.; Chong, W. K.; Yip, J. N.; Wen, X.; Li, Z.; Wei, F.; Yu, G.; Xiong, Q.; Sum, T. C. Cooperative Enhancement of Second-Harmonic Generation from a Single CdS Nanobelt-Hybrid Plasmonic Structure. *ACS Nano* **2015**, *9* (5), 5018–5026. https://doi.org/10.1021/nn5072045.
(30) *Photonic Crystals: Molding the Flow of Light*, 2nd ed.; Joannopoulos, J. D., Ed.; Princeton University Press: Princeton, 2008.
(31) Englund, D.; Majumdar, A.; Bajcsy, M.; Faraon, A.; Petroff, P.; Vučković, J. Ultrafast Photon-Photon Interaction in a Strongly Coupled Quantum Dot-Cavity System. *Phys. Rev. Lett.* **2012**, *108* (9), 093604. https://doi.org/10.1103/PhysRevLett.108.093604.
(32) Quan, Q.; Loncar, M. Deterministic Design of Wavelength Scale, Ultra-High Q Photonic Crystal Nanobeam Cavities. *Opt. Express* **2011**, *19* (19), 18529. https://doi.org/10.1364/OE.19.018529.
(33) Rosser, D.; Fryett, T.; Ryou, A.; Saxena, A.; Majumdar, A. Exciton–Phonon Interactions in Nanocavity-Integrated Monolayer Transition Metal Dichalcogenides. *npj 2D Mater Appl* **2020**, *4* (1), 20. https://doi.org/10.1038/s41699-020-0156-9.
(34) Scale Invariance. *Wikipedia*; 2024.
(35) Fryett, T. K.; Chen, Y.; Whitehead, J.; Peycke, Z. M.; Xu, X.; Majumdar, A. Encapsulated Silicon Nitride Nanobeam Cavity for Hybrid Nanophotonics. *ACS Photonics* **2018**, *5* (6), 2176–2181. https://doi.org/10.1021/acsphotonics.8b00036.
(36) Settineri, A.; Di Stefano, O.; Zueco, D.; Hughes, S.; Savasta, S.; Nori, F. Gauge Freedom, Quantum Measurements, and Time-Dependent Interactions in Cavity QED. *Phys. Rev. Research* **2021**, *3* (2), 023079. https://doi.org/10.1103/PhysRevResearch.3.023079.
(37) Zhang, W.; Serna, S.; Le Roux, X.; Vivien, L.; Cassan, E. Silicon Nanobeam Cavity for Ultra-Localized Light-Matter Interaction. *Opt. Lett.* **2017**, *42* (17), 3323. https://doi.org/10.1364/OL.42.003323.
(38) Pernice, W. H. P.; Xiong, C.; Schuck, C.; Tang, H. X. High-Q Aluminum Nitride Photonic Crystal Nanobeam Cavities. *Applied Physics Letters* **2012**, *100* (9), 091105. https://doi.org/10.1063/1.3690888.
(39) Chen, Y.; Miao, S.; Wang, T.; Zhong, D.; Saxena, A.; Chow, C.; Whitehead, J.; Gerace, D.; Xu, X.; Shi, S.-F.; Majumdar, A. Metasurface Integrated Monolayer Exciton Polariton. *Nano Lett.* **2020**, *20* (7), 5292–5300. https://doi.org/10.1021/acs.nanolett.0c01624.
(40) Flatten, L. C.; Christodoulou, S.; Patel, R. K.; Buccheri, A.; Coles, D. M.; Reid, B. P. L.; Taylor, R. A.; Moreels, I.; Smith, J. M. Strong Exciton–Photon Coupling with Colloidal Nanoplatelets in an Open Microcavity. *Nano Lett.* **2016**, *16* (11), 7137–7141. https://doi.org/10.1021/acs.nanolett.6b03433.
(41) Qiu, L.; Mandal, A.; Morshed, O.; Meidenbauer, M. T.; Girten, W.; Vamivakas, A. N.; Krauss, T. D. Molecular Polaritons Generated from Strong Coupling between CdSe Nanoplatelets and a Dielectric Optical Cavity. 12.
(42) Winkler, J. M.; Rabouw, F. T.; Rossinelli, A. A.; Jayanti, S. V.; McPeak, K. M.; Kim, D. K.; le Feber, B.; Prins, F.; Norris, D. J. Room-Temperature Strong Coupling of CdSe Nanoplatelets and Plasmonic Hole Arrays. *Nano Lett.* **2019**, *19* (1), 108–115. https://doi.org/10.1021/acs.nanolett.8b03422.

(43) Rosser, D.; Gerace, D.; Chen, Y.; Liu, Y.; Whitehead, J.; Ryou, A.; Andreani, L. C.; Majumdar, A. Dispersive Coupling between $MoSe_2$ and an Integrated Zero-Dimensional Nanocavity. *Opt. Mater. Express* **2022**, *12* (1), 59. https://doi.org/10.1364/OME.443536.
(44) Purcell, E. M. Spontaneous Emission Probabilities at Radio Frequencies. In *Confined Electrons and Photons*; Burstein, E., Weisbuch, C., Eds.; NATO ASI Series; Springer US: Boston, MA, 1995; Vol. 340, pp 839–839. https://doi.org/10.1007/978-1-4615-1963-8_40.
(45) Sakurai, J. J. *Modern Quantum Mechanics*, 3rd ed.; Cambridge University Press: Cambridge, 2020.
(46) Kavokin, A. V.; Baumberg, J.; Malpuech, G.; Laussy, F. P. *Microcavities*, Second edition.; Series on semiconductor science and technology; Oxford University Press: Oxford, 2017.
(47) Kleppner, D. Inhibited Spontaneous Emission. *Phys. Rev. Lett.* **1981**, *47* (4), 233–236. https://doi.org/10.1103/PhysRevLett.47.233.
(48) He, Z.; Chen, B.; Hua, Y.; Liu, Z.; Wei, Y.; Liu, S.; Hu, A.; Shen, X.; Zhang, Y.; Gao, Y.; Liu, J. CMOS Compatible High-Performance Nanolasing Based on Perovskite–SiN Hybrid Integration. *Advanced Optical Materials* **2020**, *8* (15), 2000453. https://doi.org/10.1002/adom.202000453.
(49) Gupta, S.; Waks, E. Spontaneous Emission Enhancement and Saturable Absorption of Colloidal Quantum Dots Coupled to Photonic Crystal Cavity. *Opt. Express* **2013**, *21* (24), 29612. https://doi.org/10.1364/OE.21.029612.
(50) Fong, C. F.; Yin, Y.; Chen, Y.; Rosser, D.; Xing, J.; Majumdar, A.; Xiong, Q. Silicon Nitride Nanobeam Enhanced Emission from All-Inorganic Perovskite Nanocrystals. *Opt. Express* **2019**, *27* (13), 18673. https://doi.org/10.1364/OE.27.018673.
(51) De Leon, N. P.; Shields, B. J.; Yu, C. L.; Englund, D. E.; Akimov, A. V.; Lukin, M. D.; Park, H. Tailoring Light-Matter Interaction with a Nanoscale Plasmon Resonator. *Phys. Rev. Lett.* **2012**, *108* (22), 226803. https://doi.org/10.1103/PhysRevLett.108.226803.
(52) Castelletto, S. A.; Scholten, R. E. Heralded Single Photon Sources: A Route towards Quantum Communication Technology and Photon Standards. *Eur. Phys. J. Appl. Phys.* **2008**, *41* (3), 181–194. https://doi.org/10.1051/epjap:2008029.
(53) Saxena, A.; Chen, Y.; Ryou, A.; Sevilla, C. G.; Xu, P.; Majumdar, A. Improving Indistinguishability of Single Photons from Colloidal Quantum Dots Using Nanocavities. *ACS Photonics* **2019**, *6* (12), 3166–3173. https://doi.org/10.1021/acsphotonics.9b01481.
(54) Cohen, T. A.; Sharp, D.; Kluherz, K. T.; Chen, Y.; Munley, C.; Anderson, R. T.; Swanson, C. J.; De Yoreo, J. J.; Luscombe, C. K.; Majumdar, A.; Gamelin, D. R.; Mackenzie, J. D. Direct Patterning of Perovskite Nanocrystals on Nanophotonic Cavities with Electrohydrodynamic Inkjet Printing. *Nano Lett.* **2022**, *22* (14), 5681–5688. https://doi.org/10.1021/acs.nanolett.2c00473.
(55) Nguyen, H. A.; Sharp, D.; Fröch, J. E.; Cai, Y.-Y.; Wu, S.; Monahan, M.; Munley, C.; Manna, A.; Majumdar, A.; Kagan, C. R.; Cossairt, B. M. Deterministic Quantum Light Arrays from Giant Silica-Shelled Quantum Dots. *ACS Appl. Mater. Interfaces* **2023**, *15* (3), 4294–4302. https://doi.org/10.1021/acsami.2c18475.
(56) Nguyen, H. A.; Hammel, B. F.; Sharp, D.; Kline, J.; Schwartz, G.; Harvey, S.; Nishiwaki, E.; Sandeno, S. F.; Ginger, D. S.; Majumdar, A.; Yazdi, S.; Dukovic, G.; Cossairt, B. M. Colossal Core/Shell CdSe/CdS Quantum Dot Emitters. *ACS Nano* **2024**, *18* (31), 20726–20739. https://doi.org/10.1021/acsnano.4c06961.
(57) Guymon, G. G.; Sharp, D.; Cohen, T. A.; Gibbs, S. L.; Manna, A.; Tzanetopoulos, E.; Gamelin, D. R.; Majumdar, A.; MacKenzie, J. D. Electrohydrodynamic Printing-Based

Heterointegration of Quantum Dots on Suspended Nanophotonic Cavities. *Adv Materials Technologies* **2024**, *9* (10), 2301921. https://doi.org/10.1002/admt.202301921.
(58) Guymon, G. G.; Nguyen, H. A.; Sharp, D.; Nguyen, T.; Lei, H.; Ginger, D. S.; Fu, K.-M. C.; Majumdar, A.; Cossairt, B. M.; MacKenzie, J. D. Deterministic Printing and Heterointegration of Single Colloidal Quantum Dot Photon Sources. arXiv January 10, 2025. https://doi.org/10.48550/arXiv.2501.04177.
(59) Choi, M.; Sharp, D.; Tang, A.; Rarick, H.; Saxena, A.; Manna, A.; Froech, J. E.; Ngyuen, H.; Cossairt, B.; Majumdar, A. Solution-Processed Quantum Dot Nanolaser Operating at Telecommunication Wavelength. In *Active Photonic Platforms (APP) 2024*; Subramania, G. S., Foteinopoulou, S., Eds.; SPIE: San Diego, United States, 2024; p 7. https://doi.org/10.1117/12.3027774.
(60) *Introduction to Microlithography*, 2. ed.; Thompson, L. F., Ed.; ACS professional reference book; American Chemical Soc: Washington, DC, 1994.
(61) Xia, Y.; Rogers, J. A.; Paul, K. E.; Whitesides, G. M. Unconventional Methods for Fabricating and Patterning Nanostructures. *Chem. Rev.* **1999**, *99* (7), 1823–1848. https://doi.org/10.1021/cr980002q.
(62) Kash, K.; Scherer, A.; Worlock, J. M.; Craighead, H. G.; Tamargo, M. C. Optical Spectroscopy of Ultrasmall Structures Etched from Quantum Wells. *Applied Physics Letters* **1986**, *49* (16), 1043–1045. https://doi.org/10.1063/1.97466.
(63) Senellart, P.; Solomon, G.; White, A. High-Performance Semiconductor Quantum-Dot Single-Photon Sources. *Nature Nanotech* **2017**, *12* (11), 1026–1039. https://doi.org/10.1038/nnano.2017.218.
(64) Suh, Y.-H.; Shin, D.-W.; Chun, Y. T. Micro-to-Nanometer Patterning of Solution-Based Materials for Electronics and Optoelectronics. *RSC Adv.* **2019**, *9* (65), 38085–38104. https://doi.org/10.1039/C9RA07514C.
(65) Tekin, E.; Smith, P. J.; Hoeppener, S.; van den Berg, A. M. J.; Susha, A. S.; Rogach, A. L.; Feldmann, J.; Schubert, U. S. Inkjet Printing of Luminescent CdTe Nanocrystal–Polymer Composites. *Adv Funct Materials* **2007**, *17* (1), 23–28. https://doi.org/10.1002/adfm.200600587.
(66) Wood, V.; Panzer, M. J.; Chen, J.; Bradley, M. S.; Halpert, J. E.; Bawendi, M. G.; Bulović, V. Inkjet-Printed Quantum Dot–Polymer Composites for Full-Color AC-Driven Displays. *Advanced Materials* **2009**, *21* (21), 2151–2155. https://doi.org/10.1002/adma.200803256.
(67) Lan, L.; Zou, J.; Jiang, C.; Liu, B.; Wang, L.; Peng, J. Inkjet Printing for Electroluminescent Devices: Emissive Materials, Film Formation, and Display Prototypes. *Front. Optoelectron.* **2017**, *10* (4), 329–352. https://doi.org/10.1007/s12200-017-0765-x.
(68) Nakao, H.; Murakami, T.; Hirahara, S.; Nagato, H.; Nomura, Y. Head Design for Novel Ink-Jet Printing Using Electrostatic Force. *print4fab* **1999**, *15* (1), 319–322. https://doi.org/10.2352/ISSN.2169-4451.1999.15.1.art00083_1.
(69) Park, J.-U.; Hardy, M.; Kang, S. J.; Barton, K.; Adair, K.; Mukhopadhyay, D. K.; Lee, C. Y.; Strano, M. S.; Alleyne, A. G.; Georgiadis, J. G.; Ferreira, P. M.; Rogers, J. A. High-Resolution Electrohydrodynamic Jet Printing. *Nature Mater* **2007**, *6* (10), 782–789. https://doi.org/10.1038/nmat1974.
(70) Kim, B. H.; Onses, M. S.; Lim, J. B.; Nam, S.; Oh, N.; Kim, H.; Yu, K. J.; Lee, J. W.; Kim, J.-H.; Kang, S.-K.; Lee, C. H.; Lee, J.; Shin, J. H.; Kim, N. H.; Leal, C.; Shim, M.; Rogers, J. A. High-Resolution Patterns of Quantum Dots Formed by Electrohydrodynamic Jet

Printing for Light-Emitting Diodes. *Nano Lett.* **2015**, *15* (2), 969–973. https://doi.org/10.1021/nl503779e.
(71) Li, H.; Duan, Y.; Shao, Z.; Zhang, G.; Li, H.; Huang, Y.; Yin, Z. High-Resolution Pixelated Light Emitting Diodes Based on Electrohydrodynamic Printing and Coffee-Ring-Free Quantum Dot Film. *Adv Materials Technologies* **2020**, *5* (10), 2000401. https://doi.org/10.1002/admt.202000401.
(72) Brossard, F. S. F.; Pecunia, V.; Ramsay, A. J.; Griffiths, J. P.; Hugues, M.; Sirringhaus, H. Inkjet-Printed Nanocavities on a Photonic Crystal Template. *Advanced Materials* **2017**, *29* (47), 1704425. https://doi.org/10.1002/adma.201704425.
(73) Aellen, M.; Rossinelli, A. A.; Keitel, R. C.; Brechbühler, R.; Antolinez, F. V.; Cui, J.; Norris, D. J. Reconsidering the Design of Planar Plasmonic Lasers: Gain, Gap Layers, and Mode Competition. arXiv January 14, 2021. https://doi.org/10.48550/arXiv.2101.05881.
(74) Kress, S. J. P.; Richner, P.; Jayanti, S. V.; Galliker, P.; Kim, D. K.; Poulikakos, D.; Norris, D. J. Near-Field Light Design with Colloidal Quantum Dots for Photonics and Plasmonics. *Nano Lett.* **2014**, *14* (10), 5827–5833. https://doi.org/10.1021/nl5026997.
(75) Kress, S. J. P.; Cui, J.; Rohner, P.; Kim, D. K.; Antolinez, F. V.; Zaininger, K.-A.; Jayanti, S. V.; Richner, P.; McPeak, K. M.; Poulikakos, D.; Norris, D. J. A Customizable Class of Colloidal-Quantum-Dot Spasers and Plasmonic Amplifiers. *Sci. Adv.* **2017**, *3* (9), e1700688. https://doi.org/10.1126/sciadv.1700688.
(76) Kress, S. J. P.; Antolinez, F. V.; Richner, P.; Jayanti, S. V.; Kim, D. K.; Prins, F.; Riedinger, A.; Fischer, M. P. C.; Meyer, S.; McPeak, K. M.; Poulikakos, D.; Norris, D. J. Wedge Waveguides and Resonators for Quantum Plasmonics. *Nano Lett.* **2015**, *15* (9), 6267–6275. https://doi.org/10.1021/acs.nanolett.5b03051.
(77) Hail, C. U.; Höller, C.; Matsuzaki, K.; Rohner, P.; Renger, J.; Sandoghdar, V.; Poulikakos, D.; Eghlidi, H. Nanoprinting Organic Molecules at the Quantum Level. *Nat Commun* **2019**, *10* (1), 1880. https://doi.org/10.1038/s41467-019-09877-5.
(78) Huang, C.-Y.; Zou, C.; Mao, C.; Corp, K. L.; Yao, Y.-C.; Lee, Y.-J.; Schlenker, C. W.; Jen, A. K. Y.; Lin, L. Y. $CsPbBr_3$ Perovskite Quantum Dot Vertical Cavity Lasers with Low Threshold and High Stability. *ACS Photonics* **2017**, *4* (9), 2281–2289. https://doi.org/10.1021/acsphotonics.7b00520.
(79) Park, Y.-S.; Guo, S.; Makarov, N. S.; Klimov, V. I. Room Temperature Single-Photon Emission from Individual Perovskite Quantum Dots. *ACS Nano* **2015**, *9* (10), 10386–10393. https://doi.org/10.1021/acsnano.5b04584.
(80) Crane, M. J.; Jacoby, L. M.; Cohen, T. A.; Huang, Y.; Luscombe, C. K.; Gamelin, D. R. Coherent Spin Precession and Lifetime-Limited Spin Dephasing in CsPbBr3 Perovskite Nanocrystals. *Nano Lett.* **2020**, *20* (12), 8626–8633. https://doi.org/10.1021/acs.nanolett.0c03329.
(81) Rainò, G.; Becker, M. A.; Bodnarchuk, M. I.; Mahrt, R. F.; Kovalenko, M. V.; Stöferle, T. Superfluorescence from Lead Halide Perovskite Quantum Dot Superlattices. *Nature* **2018**, *563* (7733), 671–675. https://doi.org/10.1038/s41586-018-0683-0.
(82) Cherniukh, I.; Rainò, G.; Stöferle, T.; Burian, M.; Travesset, A.; Naumenko, D.; Amenitsch, H.; Erni, R.; Mahrt, R. F.; Bodnarchuk, M. I.; Kovalenko, M. V. Perovskite-Type Superlattices from Lead Halide Perovskite Nanocubes. *Nature* **2021**, *593* (7860), 535–542. https://doi.org/10.1038/s41586-021-03492-5.
(83) Palazon, F.; Akkerman, Q. A.; Prato, M.; Manna, L. X-Ray Lithography on Perovskite Nanocrystals Films: From Patterning with Anion-Exchange Reactions to Enhanced

Stability in Air and Water. *ACS Nano* **2016**, *10* (1), 1224–1230. https://doi.org/10.1021/acsnano.5b06536.
(84) Minh, D. N.; Eom, S.; Nguyen, L. A. T.; Kim, J.; Sim, J. H.; Seo, C.; Nam, J.; Lee, S.; Suk, S.; Kim, J.; Kang, Y. Perovskite Nanoparticle Composite Films by Size Exclusion Lithography. *Advanced Materials* **2018**, *30* (39), 1802555. https://doi.org/10.1002/adma.201802555.
(85) Pan, J.-A.; Ondry, J. C.; Talapin, D. V. Direct Optical Lithography of CsPbX3 Nanocrystals via Photoinduced Ligand Cleavage with Postpatterning Chemical Modification and Electronic Coupling. *Nano Lett.* **2021**, *21* (18), 7609–7616. https://doi.org/10.1021/acs.nanolett.1c02249.
(86) Duan, M.; Feng, Z.; Wu, Y.; Yin, Y.; Hu, Z.; Peng, W.; Li, D.; Chen, S.; Lee, C.; Lien, A. Inkjet-Printed Micrometer-Thick Patterned Perovskite Quantum Dot Films for Efficient Blue-to-Green Photoconversion. *Adv Materials Technologies* **2019**, *4* (12), 1900779. https://doi.org/10.1002/admt.201900779.
(87) Liu, J.; Shabbir, B.; Wang, C.; Wan, T.; Ou, Q.; Yu, P.; Tadich, A.; Jiao, X.; Chu, D.; Qi, D.; Li, D.; Kan, R.; Huang, Y.; Dong, Y.; Jasieniak, J.; Zhang, Y.; Bao, Q. Flexible, Printable Soft-X-Ray Detectors Based on All-Inorganic Perovskite Quantum Dots. *Advanced Materials* **2019**, *31* (30), 1901644. https://doi.org/10.1002/adma.201901644.
(88) Altintas, Y.; Torun, I.; Yazici, A. F.; Beskazak, E.; Erdem, T.; Serdar Onses, M.; Mutlugun, E. Multiplexed Patterning of Cesium Lead Halide Perovskite Nanocrystals by Additive Jet Printing for Efficient White Light Generation. *Chemical Engineering Journal* **2020**, *380*, 122493. https://doi.org/10.1016/j.cej.2019.122493.
(89) Yakunin, S.; Chaaban, J.; Benin, B. M.; Cherniukh, I.; Bernasconi, C.; Landuyt, A.; Shynkarenko, Y.; Bolat, S.; Hofer, C.; Romanyuk, Y. E.; Cattaneo, S.; Pokutnyi, S. I.; Schaller, R. D.; Bodnarchuk, M. I.; Poulikakos, D.; Kovalenko, M. V. Radiative Lifetime-Encoded Unicolour Security Tags Using Perovskite Nanocrystals. *Nat Commun* **2021**, *12* (1), 981. https://doi.org/10.1038/s41467-021-21214-3.
(90) Rainò, G.; Landuyt, A.; Krieg, F.; Bernasconi, C.; Ochsenbein, S. T.; Dirin, D. N.; Bodnarchuk, M. I.; Kovalenko, M. V. Underestimated Effect of a Polymer Matrix on the Light Emission of Single CsPbBr3 Nanocrystals. *Nano Lett.* **2019**, *19* (6), 3648–3653. https://doi.org/10.1021/acs.nanolett.9b00689.
(91) Baranov, D.; Fieramosca, A.; Yang, R. X.; Polimeno, L.; Lerario, G.; Toso, S.; Giansante, C.; Giorgi, M. D.; Tan, L. Z.; Sanvitto, D.; Manna, L. Aging of Self-Assembled Lead Halide Perovskite Nanocrystal Superlattices: Effects on Photoluminescence and Energy Transfer. *ACS Nano* **2021**, *15* (1), 650–664. https://doi.org/10.1021/acsnano.0c06595.
(92) Cohen, T. A.; Huang, Y.; Bricker, N. A.; Juhl, C. S.; Milstein, T. J.; MacKenzie, J. D.; Luscombe, C. K.; Gamelin, D. R. Modular Zwitterion-Functionalized Poly(Isopropyl Methacrylate) Polymers for Hosting Luminescent Lead Halide Perovskite Nanocrystals. *Chem. Mater.* **2021**, *33* (10), 3779–3790. https://doi.org/10.1021/acs.chemmater.1c00902.
(93) Chen, Y.; Ryou, A.; Friedfeld, M. R.; Fryett, T.; Whitehead, J.; Cossairt, B. M.; Majumdar, A. Deterministic Positioning of Colloidal Quantum Dots on Silicon Nitride Nanobeam Cavities. *Nano Lett.* **2018**, *18* (10), 6404–6410. https://doi.org/10.1021/acs.nanolett.8b02764.
(94) Frank, I. W.; Deotare, P. B.; McCutcheon, M. W.; Lončar, M. Programmable Photonic Crystal Nanobeam Cavities. *Opt. Express* **2010**, *18* (8), 8705. https://doi.org/10.1364/OE.18.008705.

(95) Vlaskin, V. A.; Barrows, C. J.; Erickson, C. S.; Gamelin, D. R. Nanocrystal Diffusion Doping. *J. Am. Chem. Soc.* **2013**, *135* (38), 14380–14389. https://doi.org/10.1021/ja4072207.
(96) Hanifi, D. A.; Bronstein, N. D.; Koscher, B. A.; Nett, Z.; Swabeck, J. K.; Takano, K.; Schwartzberg, A. M.; Maserati, L.; Vandewal, K.; Van De Burgt, Y.; Salleo, A.; Alivisatos, A. P. Redefining Near-Unity Luminescence in Quantum Dots with Photothermal Threshold Quantum Yield. *Science* **2019**, *363* (6432), 1199–1202. https://doi.org/10.1126/science.aat3803.
(97) Geiregat, P.; Allan, G.; Hens, Z.; Delerue, C. Single-Exciton Optical Gain in Semiconductor Nanocrystals: Positive Role of Electron-Phonon Coupling. *Phys. Rev. B* **2016**, *93* (11), 115416. https://doi.org/10.1103/PhysRevB.93.115416.
(98) Lim, J.; Park, Y.-S.; Klimov, V. I. Optical Gain in Colloidal Quantum Dots Achieved with Direct-Current Electrical Pumping. *Nature Mater* **2018**, *17* (1), 42–49. https://doi.org/10.1038/nmat5011.
(99) Jung, H.; Ahn, N.; Klimov, V. I. Prospects and Challenges of Colloidal Quantum Dot Laser Diodes. *Nat. Photon.* **2021**, *15* (9), 643–655. https://doi.org/10.1038/s41566-021-00827-6.
(100) Walsh, K. M.; Pressler, K.; Crane, M. J.; Gamelin, D. R. Ferromagnetism and Spin-Polarized Luminescence in Lead-Free CsEuCl3 Perovskite Nanocrystals and Thin Films. *ACS Nano* **2022**, *16* (2), 2569–2576. https://doi.org/10.1021/acsnano.1c09257.
(101) De Siena, M. C.; Creutz, S. E.; Regan, A.; Malinowski, P.; Jiang, Q.; Kluherz, K. T.; Zhu, G.; Lin, Z.; De Yoreo, J. J.; Xu, X.; Chu, J.-H.; Gamelin, D. R. Two-Dimensional van Der Waals Nanoplatelets with Robust Ferromagnetism. *Nano Lett.* **2020**, *20* (3), 2100–2106. https://doi.org/10.1021/acs.nanolett.0c00102.
(102) Pressler, K.; Snoeren, T. J.; Walsh, K. M.; Gamelin, D. R. Magnetic Amplification at Yb3+ "Designer Defects" in the van Der Waals Ferromagnet CrI3. *Nano Lett.* **2023**, *23* (4), 1320–1326. https://doi.org/10.1021/acs.nanolett.2c04533.
(103) Milstein, T. J.; Kroupa, D. M.; Gamelin, D. R. Picosecond Quantum Cutting Generates Photoluminescence Quantum Yields Over 100% in Ytterbium-Doped $CsPbCl_3$ Nanocrystals. *Nano Lett.* **2018**, *18* (6), 3792–3799. https://doi.org/10.1021/acs.nanolett.8b01066.
(104) Khan, M.; Babinec, T.; McCutcheon, M. W.; Deotare, P.; Lončar, M. Fabrication and Characterization of High-Quality-Factor Silicon Nitride Nanobeam Cavities. *Opt. Lett.* **2011**, *36* (3), 421. https://doi.org/10.1364/OL.36.000421.
(105) Hodaei, H.; Miri, M.-A.; Heinrich, M.; Christodoulides, D. N.; Khajavikhan, M. Parity-Time-Symmetric Microring Lasers. *Science* **2014**, *346* (6212), 975–978. https://doi.org/10.1126/science.1258480.
(106) Zhang, S.; Yong, Z.; Zhang, Y.; He, S. Parity-Time Symmetry Breaking in Coupled Nanobeam Cavities. *Sci Rep* **2016**, *6* (1), 24487. https://doi.org/10.1038/srep24487.
(107) Wei, W.-Q.; He, A.; Yang, B.; Wang, Z.-H.; Huang, J.-Z.; Han, D.; Ming, M.; Guo, X.; Su, Y.; Zhang, J.-J.; Wang, T. Monolithic Integration of Embedded III-V Lasers on SOI. *Light Sci Appl* **2023**, *12* (1), 84. https://doi.org/10.1038/s41377-023-01128-z.
(108) Madsen, L. S.; Laudenbach, F.; Askarani, M. Falamarzi.; Rortais, F.; Vincent, T.; Bulmer, J. F. F.; Miatto, F. M.; Neuhaus, L.; Helt, L. G.; Collins, M. J.; Lita, A. E.; Gerrits, T.; Nam, S. W.; Vaidya, V. D.; Menotti, M.; Dhand, I.; Vernon, Z.; Quesada, N.; Lavoie, J. Quantum Computational Advantage with a Programmable Photonic Processor. *Nature* **2022**, *606* (7912), 75–81. https://doi.org/10.1038/s41586-022-04725-x.

(109) Wang, H.; Qin, J.; Ding, X.; Chen, M.-C.; Chen, S.; You, X.; He, Y.-M.; Jiang, X.; You, L.; Wang, Z.; Schneider, C.; Renema, J. J.; Höfling, S.; Lu, C.-Y.; Pan, J.-W. Boson Sampling with 20 Input Photons and a 60-Mode Interferometer in a 1 0 14 -Dimensional Hilbert Space. *Phys. Rev. Lett.* **2019**, *123* (25), 250503. https://doi.org/10.1103/PhysRevLett.123.250503.
(110) Majumdar, A.; Rundquist, A.; Bajcsy, M.; Dasika, V. D.; Bank, S. R.; Vučković, J. Design and Analysis of Photonic Crystal Coupled Cavity Arrays for Quantum Simulation. *Phys. Rev. B* **2012**, *86* (19), 195312. https://doi.org/10.1103/PhysRevB.86.195312.
(111) Michler, P.; Imamoğlu, A.; Mason, M. D.; Carson, P. J.; Strouse, G. F.; Buratto, S. K. Quantum Correlation among Photons from a Single Quantum Dot at Room Temperature. *Nature* **2000**, *406* (6799), 968–970. https://doi.org/10.1038/35023100.
(112) Chandrasekaran, V.; Tessier, M. D.; Dupont, D.; Geiregat, P.; Hens, Z.; Brainis, E. Nearly Blinking-Free, High-Purity Single-Photon Emission by Colloidal InP/ZnSe Quantum Dots. *Nano Lett.* **2017**, *17* (10), 6104–6109. https://doi.org/10.1021/acs.nanolett.7b02634.
(113) Morozov, S.; Pensa, E. L.; Khan, A. H.; Polovitsyn, A.; Cortés, E.; Maier, S. A.; Vezzoli, S.; Moreels, I.; Sapienza, R. Electrical Control of Single-Photon Emission in Highly Charged Individual Colloidal Quantum Dots. *Sci. Adv.* **2020**, *6* (38), eabb1821. https://doi.org/10.1126/sciadv.abb1821.
(114) Lin, X.; Dai, X.; Pu, C.; Deng, Y.; Niu, Y.; Tong, L.; Fang, W.; Jin, Y.; Peng, X. Electrically-Driven Single-Photon Sources Based on Colloidal Quantum Dots with near-Optimal Antibunching at Room Temperature. *Nat Commun* **2017**, *8* (1), 1132. https://doi.org/10.1038/s41467-017-01379-6.
(115) Xu, X.; Jin, S. Strong Coupling of Single Quantum Dots with Low-Refractive-Index/High-Refractive-Index Materials at Room Temperature. *Sci. Adv.* **2020**, *6* (47), eabb3095. https://doi.org/10.1126/sciadv.abb3095.
(116) Cui, Y.; Björk, M. T.; Liddle, J. A.; Sönnichsen, C.; Boussert, B.; Alivisatos, A. P. Integration of Colloidal Nanocrystals into Lithographically Patterned Devices. *Nano Lett.* **2004**, *4* (6), 1093–1098. https://doi.org/10.1021/nl049488i.
(117) Yadav, R. K.; Liu, W.; Li, R.; Odom, T. W.; Agarwal, G. S.; Basu, J. K. Room-Temperature Coupling of Single Photon Emitting Quantum Dots to Localized and Delocalized Modes in a Plasmonic Nanocavity Array. *ACS Photonics* **2021**, *8* (2), 576–584. https://doi.org/10.1021/acsphotonics.0c01635.
(118) Eich, A.; Spiekermann, T. C.; Gehring, H.; Sommer, L.; Bankwitz, J. R.; Schrinner, P. P. J.; Preuß, J. A.; Michaelis de Vasconcellos, S.; Bratschitsch, R.; Pernice, W. H. P.; Schuck, C. Single-Photon Emission from Individual Nanophotonic-Integrated Colloidal Quantum Dots. *ACS Photonics* **2022**, acsphotonics.1c01493. https://doi.org/10.1021/acsphotonics.1c01493.
(119) Zhang, Q.; Dang, C.; Urabe, H.; Wang, J.; Sun, S.; Nurmikko, A. Large Ordered Arrays of Single Photon Sources Based on II–VI Semiconductor Colloidal Quantum Dot. *Opt. Express* **2008**, *16* (24), 19592. https://doi.org/10.1364/OE.16.019592.
(120) Kim, J.-H.; Aghaeimeibodi, S.; Carolan, J.; Englund, D.; Waks, E. Hybrid Integration Methods for On-Chip Quantum Photonics. *Optica* **2020**, *7* (4), 291. https://doi.org/10.1364/OPTICA.384118.
(121) Davanco, M.; Liu, J.; Sapienza, L.; Zhang, C.-Z.; De Miranda Cardoso, J. V.; Verma, V.; Mirin, R.; Nam, S. W.; Liu, L.; Srinivasan, K. Heterogeneous Integration for On-Chip

Quantum Photonic Circuits with Single Quantum Dot Devices. *Nat Commun* **2017**, *8* (1), 889. https://doi.org/10.1038/s41467-017-00987-6.
(122) Kolchin, P.; Pholchai, N.; Mikkelsen, M. H.; Oh, J.; Ota, S.; Islam, M. S.; Yin, X.; Zhang, X. High Purcell Factor Due To Coupling of a Single Emitter to a Dielectric Slot Waveguide. *Nano Lett.* **2015**, *15* (1), 464–468. https://doi.org/10.1021/nl5037808.
(123) Kagan, C. R.; Bassett, L. C.; Murray, C. B.; Thompson, S. M. Colloidal Quantum Dots as Platforms for Quantum Information Science. *Chem. Rev.* **2021**, *121* (5), 3186–3233. https://doi.org/10.1021/acs.chemrev.0c00831.
(124) Nann, T.; Mulvaney, P. Single Quantum Dots in Spherical Silica Particles. *Angew Chem Int Ed* **2004**, *43* (40), 5393–5396. https://doi.org/10.1002/anie.200460752.
(125) Ma, Y.; Li, Y.; Ma, S.; Zhong, X. Highly Bright Water-Soluble Silica Coated Quantum Dots with Excellent Stability. *J. Mater. Chem. B* **2014**, *2* (31), 5043–5051. https://doi.org/10.1039/C4TB00458B.
(126) Hu, X.; Zrazhevskiy, P.; Gao, X. Encapsulation of Single Quantum Dots with Mesoporous Silica. *Ann Biomed Eng* **2009**, *37* (10), 1960–1966. https://doi.org/10.1007/s10439-009-9660-y.
(127) Goftman, V. V.; Aubert, T.; Ginste, D. V.; Van Deun, R.; Beloglazova, N. V.; Hens, Z.; De Saeger, S.; Goryacheva, I. Yu. Synthesis, Modification, Bioconjugation of Silica Coated Fluorescent Quantum Dots and Their Application for Mycotoxin Detection. *Biosensors and Bioelectronics* **2016**, *79*, 476–481. https://doi.org/10.1016/j.bios.2015.12.079.
(128) Aubert, T.; Soenen, S. J.; Wassmuth, D.; Cirillo, M.; Van Deun, R.; Braeckmans, K.; Hens, Z. Bright and Stable CdSe/CdS@SiO2 Nanoparticles Suitable for Long-Term Cell Labeling. *ACS Appl. Mater. Interfaces* **2014**, *6* (14), 11714–11723. https://doi.org/10.1021/am502367b.
(129) Huang, Y.; Cohen, T. A.; Sperry, B. M.; Larson, H.; Nguyen, H. A.; Homer, M. K.; Dou, F. Y.; Jacoby, L. M.; Cossairt, B. M.; Gamelin, D. R.; Luscombe, C. K. Organic Building Blocks at Inorganic Nanomaterial Interfaces. *Mater. Horiz.* **2022**, *9* (1), 61–87. https://doi.org/10.1039/D1MH01294K.
(130) Shulevitz, H. J.; Huang, T.-Y.; Xu, J.; Neuhaus, S. J.; Patel, R. N.; Choi, Y. C.; Bassett, L. C.; Kagan, C. R. Template-Assisted Self-Assembly of Fluorescent Nanodiamonds for Scalable Quantum Technologies. *ACS Nano* **2022**, *16* (2), 1847–1856. https://doi.org/10.1021/acsnano.1c09839.
(131) Greybush, N. J.; Pacheco-Peña, V.; Engheta, N.; Murray, C. B.; Kagan, C. R. Plasmonic Optical and Chiroptical Response of Self-Assembled Au Nanorod Equilateral Trimers. *ACS Nano* **2019**, *13* (2), 1617–1624. https://doi.org/10.1021/acsnano.8b07619.
(132) Chen, Y.; Vela, J.; Htoon, H.; Casson, J. L.; Werder, D. J.; Bussian, D. A.; Klimov, V. I.; Hollingsworth, J. A. "Giant" Multishell CdSe Nanocrystal Quantum Dots with Suppressed Blinking. *J. Am. Chem. Soc.* **2008**, *130* (15), 5026–5027. https://doi.org/10.1021/ja711379k.
(133) Gong, K.; Kelley, D. F. Lattice Strain Limit for Uniform Shell Deposition in Zincblende CdSe/CdS Quantum Dots. *J. Phys. Chem. Lett.* **2015**, *6* (9), 1559–1562. https://doi.org/10.1021/acs.jpclett.5b00566.
(134) Pahomi, T. E.; Cheche, T. O. Strain Influence on Optical Absorption of Giant Semiconductor Colloidal Quantum Dots. *Chemical Physics Letters* **2014**, *612*, 33–38. https://doi.org/10.1016/j.cplett.2014.07.078.

(135) Rafipoor, M.; Dupont, D.; Tornatzky, H.; Tessier, M. D.; Maultzsch, J.; Hens, Z.; Lange, H. Strain Engineering in InP/(Zn,Cd)Se Core/Shell Quantum Dots. *Chem. Mater.* **2018**, *30* (13), 4393–4400. https://doi.org/10.1021/acs.chemmater.8b01789.
(136) Chen, O.; Zhao, J.; Chauhan, V. P.; Cui, J.; Wong, C.; Harris, D. K.; Wei, H.; Han, H.-S.; Fukumura, D.; Jain, R. K.; Bawendi, M. G. Compact High-Quality CdSe–CdS Core–Shell Nanocrystals with Narrow Emission Linewidths and Suppressed Blinking. *Nature Mater* **2013**, *12* (5), 445–451. https://doi.org/10.1038/nmat3539.
(137) Yin, Y.; Lu, Y.; Gates, B.; Xia, Y. Template-Assisted Self-Assembly: A Practical Route to Complex Aggregates of Monodispersed Colloids with Well-Defined Sizes, Shapes, and Structures. *J. Am. Chem. Soc.* **2001**, *123* (36), 8718–8729. https://doi.org/10.1021/ja011048v.
(138) Mehraeen, S.; Asbahi, M.; Fuke, W.; Yang, J. K. W.; Cao, J.; Tan, M. C. Directed Self-Assembly of Sub-10 Nm Particles: Role of Driving Forces and Template Geometry in Packing and Ordering. *Langmuir* **2015**, *31* (31), 8548–8557. https://doi.org/10.1021/acs.langmuir.5b01696.
(139) Asbahi, M.; Mehraeen, S.; Wang, F.; Yakovlev, N.; Chong, K. S. L.; Cao, J.; Tan, M. C.; Yang, J. K. W. Large Area Directed Self-Assembly of Sub-10 Nm Particles with Single Particle Positioning Resolution. *Nano Lett.* **2015**, *15* (9), 6066–6070. https://doi.org/10.1021/acs.nanolett.5b02291.
(140) Nguyen, H. A.; Dixon, G.; Dou, F. Y.; Gallagher, S.; Gibbs, S.; Ladd, D. M.; Marino, E.; Ondry, J. C.; Shanahan, J. P.; Vasileiadou, E. S.; Barlow, S.; Gamelin, D. R.; Ginger, D. S.; Jonas, D. M.; Kanatzidis, M. G.; Marder, S. R.; Morton, D.; Murray, C. B.; Owen, J. S.; Talapin, D. V.; Toney, M. F.; Cossairt, B. M. Design Rules for Obtaining Narrow Luminescence from Semiconductors Made in Solution. *Chem. Rev.* **2023**, *123* (12), 7890–7952. https://doi.org/10.1021/acs.chemrev.3c00097.
(141) Galliker, P.; Schneider, J.; Eghlidi, H.; Kress, S.; Sandoghdar, V.; Poulikakos, D. Direct Printing of Nanostructures by Electrostatic Autofocussing of Ink Nanodroplets. *Nat Commun* **2012**, *3* (1), 890. https://doi.org/10.1038/ncomms1891.
(142) Choi, J.-H.; Wang, H.; Oh, S. J.; Paik, T.; Sung, P.; Sung, J.; Ye, X.; Zhao, T.; Diroll, B. T.; Murray, C. B.; Kagan, C. R. Exploiting the Colloidal Nanocrystal Library to Construct Electronic Devices. *Science* **2016**, *352* (6282), 205–208. https://doi.org/10.1126/science.aad0371.
(143) Olshansky, J. H.; Harvey, S. M.; Pennel, M. L.; Krzyaniak, M. D.; Schaller, R. D.; Wasielewski, M. R. Using Photoexcited Core/Shell Quantum Dots To Spin Polarize Appended Radical Qubits. *J. Am. Chem. Soc.* **2020**, *142* (31), 13590–13597. https://doi.org/10.1021/jacs.0c06073.
(144) Hetsch, F.; Zhao, N.; Kershaw, S. V.; Rogach, A. L. Quantum Dot Field Effect Transistors. *Materials Today* **2013**, *16* (9), 312–325. https://doi.org/10.1016/j.mattod.2013.08.011.
(145) Shibata, K.; Yoshida, M.; Hirakawa, K.; Otsuka, T.; Bisri, S. Z.; Iwasa, Y. Single PbS Colloidal Quantum Dot Transistors. *Nat Commun* **2023**, *14* (1), 7486. https://doi.org/10.1038/s41467-023-43343-7.
(146) Chang, J.; Gao, J.; Esmaeil Zadeh, I.; Elshaari, A. W.; Zwiller, V. Nanowire-Based Integrated Photonics for Quantum Information and Quantum Sensing. *Nanophotonics* **2023**, *12* (3), 339–358. https://doi.org/10.1515/nanoph-2022-0652.

(147) Kovalenko, M. V.; Protesescu, L.; Bodnarchuk, M. I. Properties and Potential Optoelectronic Applications of Lead Halide Perovskite Nanocrystals. *Science* **2017**, *358* (6364), 745–750. https://doi.org/10.1126/science.aam7093.
(148) Shamsi, J.; Rainò, G.; Kovalenko, M. V.; Stranks, S. D. To Nano or Not to Nano for Bright Halide Perovskite Emitters. *Nat. Nanotechnol.* **2021**, *16* (11), 1164–1168. https://doi.org/10.1038/s41565-021-01005-z.
(149) Yun, H. J.; Lim, J.; Roh, J.; Neo, D. C. J.; Law, M.; Klimov, V. I. Solution-Processable Integrated CMOS Circuits Based on Colloidal CuInSe2 Quantum Dots. *Nat Commun* **2020**, *11* (1), 5280. https://doi.org/10.1038/s41467-020-18932-5.
(150) Cao, W.; Chern, M.; Dennis, A. M.; Brown, K. A. Measuring Nanoparticle Polarizability Using Fluorescence Microscopy. *Nano Lett.* **2019**, *19* (8), 5762–5768. https://doi.org/10.1021/acs.nanolett.9b02402.
(151) Limonov, M. F.; Rybin, M. V.; Poddubny, A. N.; Kivshar, Y. S. Fano Resonances in Photonics. *Nature Photon* **2017**, *11* (9), 543–554. https://doi.org/10.1038/nphoton.2017.142.
(152) Berkinsky, D. B.; Proppe, A. H.; Utzat, H.; Krajewska, C. J.; Sun, W.; Šverko, T.; Yoo, J. J.; Chung, H.; Won, Y.-H.; Kim, T.; Jang, E.; Bawendi, M. G. Narrow Intrinsic Line Widths and Electron–Phonon Coupling of InP Colloidal Quantum Dots. *ACS Nano* **2023**, *17* (4), 3598–3609. https://doi.org/10.1021/acsnano.2c10237.
(153) Sharp, D.; Lin, R.; Nguyen, H.; Manna, A.; Rarick, H.; Munley, C.; Cho, W.; Talapin, D.; Cossairt, B.; Majumdar, A. Nanolaser Using Colloidal Quantum Wells Deterministically Integrated on a Nanocavity. *ACS Photonics* **2024**, *11* (6), 2465–2470. https://doi.org/10.1021/acsphotonics.4c00377.
(154) Ma, R.-M.; Oulton, R. F. Applications of Nanolasers. *Nature Nanotech* **2019**, *14* (1), 12–22. https://doi.org/10.1038/s41565-018-0320-y.
(155) Wang, Y.; Ta, V. D.; Leck, K. S.; Tan, B. H. I.; Wang, Z.; He, T.; Ohl, C.-D.; Demir, H. V.; Sun, H. Robust Whispering-Gallery-Mode Microbubble Lasers from Colloidal Quantum Dots. *Nano Lett.* **2017**, *17* (4), 2640–2646. https://doi.org/10.1021/acs.nanolett.7b00447.
(156) Yang, X.; Li, B. Laser Emission from Ring Resonators Formed by a Quantum-Dot-Doped Single Polymer Nanowire. *ACS Macro Lett.* **2014**, *3* (12), 1266–1270. https://doi.org/10.1021/mz500663t.
(157) Montanarella, F.; Urbonas, D.; Chadwick, L.; Moerman, P. G.; Baesjou, P. J.; Mahrt, R. F.; Van Blaaderen, A.; Stöferle, T.; Vanmaekelbergh, D. Lasing Supraparticles Self-Assembled from Nanocrystals. *ACS Nano* **2018**, *12* (12), 12788–12794. https://doi.org/10.1021/acsnano.8b07896.
(158) Wang, K.; Sun, W.; Li, J.; Gu, Z.; Xiao, S.; Song, Q. Unidirectional Lasing Emissions from $CH_3NH_3PbBr_3$ Perovskite Microdisks. *ACS Photonics* **2016**, *3* (6), 1125–1130. https://doi.org/10.1021/acsphotonics.6b00209.
(159) Grim, J. Q.; Christodoulou, S.; Di Stasio, F.; Krahne, R.; Cingolani, R.; Manna, L.; Moreels, I. Continuous-Wave Biexciton Lasing at Room Temperature Using Solution-Processed Quantum Wells. *Nature Nanotech* **2014**, *9* (11), 891–895. https://doi.org/10.1038/nnano.2014.213.
(160) Baghani, E.; O'Leary, S. K.; Fedin, I.; Talapin, D. V.; Pelton, M. Auger-Limited Carrier Recombination and Relaxation in CdSe Colloidal Quantum Wells. *J. Phys. Chem. Lett.* **2015**, *6* (6), 1032–1036. https://doi.org/10.1021/acs.jpclett.5b00143.

(161) Pelton, M. Carrier Dynamics, Optical Gain, and Lasing with Colloidal Quantum Wells. *J. Phys. Chem. C* **2018**, *122* (20), 10659–10674. https://doi.org/10.1021/acs.jpcc.7b12629.
(162) She, C.; Fedin, I.; Dolzhnikov, D. S.; Dahlberg, P. D.; Engel, G. S.; Schaller, R. D.; Talapin, D. V. Red, Yellow, Green, and Blue Amplified Spontaneous Emission and Lasing Using Colloidal CdSe Nanoplatelets. *ACS Nano* **2015**, *9* (10), 9475–9485. https://doi.org/10.1021/acsnano.5b02509.
(163) Hazarika, A.; Fedin, I.; Hong, L.; Guo, J.; Srivastava, V.; Cho, W.; Coropceanu, I.; Portner, J.; Diroll, B. T.; Philbin, J. P.; Rabani, E.; Klie, R.; Talapin, D. V. Colloidal Atomic Layer Deposition with Stationary Reactant Phases Enables Precise Synthesis of "Digital" II–VI Nano-Heterostructures with Exquisite Control of Confinement and Strain. *J. Am. Chem. Soc.* **2019**, *141* (34), 13487–13496. https://doi.org/10.1021/jacs.9b04866.
(164) Beadie, G.; Brindza, M.; Flynn, R. A.; Rosenberg, A.; Shirk, J. S. Refractive Index Measurements of Poly(Methyl Methacrylate) (PMMA) from 04–16 Mm. *Appl. Opt.* **2015**, *54* (31), F139. https://doi.org/10.1364/AO.54.00F139.
(165) Meldrum, A.; Bianucci, P.; Marsiglio, F. Modification of Ensemble Emission Rates and Luminescence Spectra for Inhomogeneously Broadened Distributions of Quantum Dots Coupled to Optical Microcavities. *Opt. Express* **2010**, *18* (10), 10230. https://doi.org/10.1364/OE.18.010230.
(166) Kunneman, L. T.; Schins, J. M.; Pedetti, S.; Heuclin, H.; Grozema, F. C.; Houtepen, A. J.; Dubertret, B.; Siebbeles, L. D. A. Nature and Decay Pathways of Photoexcited States in CdSe and CdSe/CdS Nanoplatelets. *Nano Lett.* **2014**, *14* (12), 7039–7045. https://doi.org/10.1021/nl503406a.
(167) Wu, S.; Buckley, S.; Schaibley, J. R.; Feng, L.; Yan, J.; Mandrus, D. G.; Hatami, F.; Yao, W.; Vučković, J.; Majumdar, A.; Xu, X. Monolayer Semiconductor Nanocavity Lasers with Ultralow Thresholds. *Nature* **2015**, *520* (7545), 69–72. https://doi.org/10.1038/nature14290.
(168) Bjork, G.; Yamamoto, Y. Analysis of Semiconductor Microcavity Lasers Using Rate Equations. *IEEE Journal of Quantum Electronics* **1991**, *27* (11), 2386–2396. https://doi.org/10.1109/3.100877.
(169) Hinterding, S. O. M.; Salzmann, B. B. V.; Vonk, S. J. W.; Vanmaekelbergh, D.; Weckhuysen, B. M.; Hutter, E. M.; Rabouw, F. T. Single Trap States in Single CdSe Nanoplatelets. *ACS Nano* **2021**, *15* (4), 7216–7225. https://doi.org/10.1021/acsnano.1c00481.
(170) Rodà, C.; Di Giacomo, A.; Tasende Rodríguez, L. C.; M, C. S.; Leemans, J.; Hens, Z.; Geiregat, P.; Moreels, I. Colloidal CdSe/CdS Core/Crown Nanoplatelets for Efficient Blue Light Emission and Optical Amplification. *Nano Lett.* **2023**, *23* (8), 3224–3230. https://doi.org/10.1021/acs.nanolett.2c05061.
(171) Shin, A. J.; Hossain, A. A.; Tenney, S. M.; Tan, X.; Tan, L. A.; Foley, J. J.; Atallah, T. L.; Caram, J. R. Dielectric Screening Modulates Semiconductor Nanoplatelet Excitons. *J. Phys. Chem. Lett.* **2021**, *12* (20), 4958–4964. https://doi.org/10.1021/acs.jpclett.1c00624.
(172) Björk, G.; Karlsson, A.; Yamamoto, Y. On the Linewidth of Microcavity Lasers. *Appl. Phys. Lett.* **1992**, *60* (3), 304–306. https://doi.org/10.1063/1.106693.
(173) Cho, W.; Kim, S.; Coropceanu, I.; Srivastava, V.; Diroll, B. T.; Hazarika, A.; Fedin, I.; Galli, G.; Schaller, R. D.; Talapin, D. V. Direct Synthesis of Six-Monolayer (1.9 Nm) Thick Zinc-Blende CdSe Nanoplatelets Emitting at 585 Nm. *Chem. Mater.* **2018**, *30* (20), 6957–6960. https://doi.org/10.1021/acs.chemmater.8b02489.

(174) Zhang, Q.; Zhu, Y.; Niu, P.; Lao, C.; Yao, Y.; Liu, W.; Yang, Q.-F.; Chu, S.; Gao, Y. Low-Threshold Single-Mode Microlasers from Green CdSe/CdSeS Core/Alloyed-Crown Nanoplatelets. *ACS Photonics* **2023**, acsphotonics.3c00018. https://doi.org/10.1021/acsphotonics.3c00018.
(175) Ahn, N.; Livache, C.; Pinchetti, V.; Jung, H.; Jin, H.; Hahm, D.; Park, Y.-S.; Klimov, V. I. Electrically Driven Amplified Spontaneous Emission from Colloidal Quantum Dots. *Nature* **2023**, *617* (7959), 79–85. https://doi.org/10.1038/s41586-023-05855-6.
(176) Kumar, R.; Su, G.-L.; Huang, D.; Soon, C. Y.; Okitsu, M.; Davis, J.; Pham, T.; Mahalingam, H.; Hakami, M.; Sikder, K.; Wu, C.; O'Brien, W.; Bowles, A.; Gold, D.; Du, H.; Jones, R.; Rong, H. Fully Integrated Tunable III-V/Si Laser with on-Chip SOA. *J. Lightwave Technol.* **2024**, 1–6. https://doi.org/10.1109/JLT.2024.3361080.
(177) Bian, Y.; Ramachandran, K.; Wu, Z.-J.; Hedrick, B.; Dezfulian, K. K.; Houghton, T.; Nummy, K.; Fisher, D.; Hirokawa, T.; Donegan, K.; Afzal, F. O.; Esopi, M.; Karra, V.; Lee, W. S.; Sorbara, M.; Lubguban, J.; Cho, J. K.; Cao, R.; Ding, H.; Chandran, S.; Rakowski, M.; Aboketaf, A.; Krishnamurthy, S.; Mills, S.; Peng, B.; Pepper, J.; Deka, S.; Feng, W.; Rishton, S.; Boudreau, M.; Logan, D.; Hickey, R.; Gomes, P. C.; Murray, K.; Dewanjee, A.; Riggs, D.; Robson, N.; Melville, I.; Augur, R.; Fox, R.; Gupta, V.; Yu, A.; Giewont, K.; Pellerin, J.; Letavic, T. 3D Integrated Laser Attach Technology on a 300-Mm Monolithic CMOS Silicon Photonics Platform. *IEEE J. Select. Topics Quantum Electron.* **2023**, 1–19. https://doi.org/10.1109/JSTQE.2023.3238290.
(178) Crosnier, G.; Sanchez, D.; Bouchoule, S.; Monnier, P.; Beaudoin, G.; Sagnes, I.; Raj, R.; Raineri, F. Hybrid Indium Phosphide-on-Silicon Nanolaser Diode. *Nature Photon* **2017**, *11* (5), 297–300. https://doi.org/10.1038/nphoton.2017.56.
(179) Lee, J.; Karnadi, I.; Kim, J. T.; Lee, Y.-H.; Kim, M.-K. Printed Nanolaser on Silicon. *ACS Photonics* **2017**, *4* (9), 2117–2123. https://doi.org/10.1021/acsphotonics.7b00488.
(180) Bao, S.; Kim, D.; Onwukaeme, C.; Gupta, S.; Saraswat, K.; Lee, K. H.; Kim, Y.; Min, D.; Jung, Y.; Qiu, H.; Wang, H.; Fitzgerald, E. A.; Tan, C. S.; Nam, D. Low-Threshold Optically Pumped Lasing in Highly Strained Germanium Nanowires. *Nat Commun* **2017**, *8* (1), 1845. https://doi.org/10.1038/s41467-017-02026-w.
(181) Wirths, S.; Geiger, R.; Von Den Driesch, N.; Mussler, G.; Stoica, T.; Mantl, S.; Ikonic, Z.; Luysberg, M.; Chiussi, S.; Hartmann, J. M.; Sigg, H.; Faist, J.; Buca, D.; Grützmacher, D. Lasing in Direct-Bandgap GeSn Alloy Grown on Si. *Nature Photon* **2015**, *9* (2), 88–92. https://doi.org/10.1038/nphoton.2014.321.
(182) Redjem, W.; Zhiyenbayev, Y.; Qarony, W.; Ivanov, V.; Papapanos, C.; Liu, W.; Jhuria, K.; Al Balushi, Z. Y.; Dhuey, S.; Schwartzberg, A.; Tan, L. Z.; Schenkel, T.; Kanté, B. All-Silicon Quantum Light Source by Embedding an Atomic Emissive Center in a Nanophotonic Cavity. *Nat Commun* **2023**, *14* (1), 3321. https://doi.org/10.1038/s41467-023-38559-6.
(183) Redjem, W.; Durand, A.; Herzig, T.; Benali, A.; Pezzagna, S.; Meijer, J.; Kuznetsov, A. Yu.; Nguyen, H. S.; Cueff, S.; Gérard, J.-M.; Robert-Philip, I.; Gil, B.; Caliste, D.; Pochet, P.; Abbarchi, M.; Jacques, V.; Dréau, A.; Cassabois, G. Single Artificial Atoms in Silicon Emitting at Telecom Wavelengths. *Nat Electron* **2020**, *3* (12), 738–743. https://doi.org/10.1038/s41928-020-00499-0.
(184) Liu, M.; Yazdani, N.; Yarema, M.; Jansen, M.; Wood, V.; Sargent, E. H. Colloidal Quantum Dot Electronics. *Nat Electron* **2021**, *4* (8), 548–558. https://doi.org/10.1038/s41928-021-00632-7.

(185) Dey, A.; Ye, J.; De, A.; Debroye, E.; Ha, S. K.; Bladt, E.; Kshirsagar, A. S.; Wang, Z.; Yin, J.; Wang, Y.; Quan, L. N.; Yan, F.; Gao, M.; Li, X.; Shamsi, J.; Debnath, T.; Cao, M.; Scheel, M. A.; Kumar, S.; Steele, J. A.; Gerhard, M.; Chouhan, L.; Xu, K.; Wu, X.; Li, Y.; Zhang, Y.; Dutta, A.; Han, C.; Vincon, I.; Rogach, A. L.; Nag, A.; Samanta, A.; Korgel, B. A.; Shih, C.-J.; Gamelin, D. R.; Son, D. H.; Zeng, H.; Zhong, H.; Sun, H.; Demir, H. V.; Scheblykin, I. G.; Mora-Seró, I.; Stolarczyk, J. K.; Zhang, J. Z.; Feldmann, J.; Hofkens, J.; Luther, J. M.; Pérez-Prieto, J.; Li, L.; Manna, L.; Bodnarchuk, M. I.; Kovalenko, M. V.; Roeffaers, M. B. J.; Pradhan, N.; Mohammed, O. F.; Bakr, O. M.; Yang, P.; Müller-Buschbaum, P.; Kamat, P. V.; Bao, Q.; Zhang, Q.; Krahne, R.; Galian, R. E.; Stranks, S. D.; Bals, S.; Biju, V.; Tisdale, W. A.; Yan, Y.; Hoye, R. L. Z.; Polavarapu, L. State of the Art and Prospects for Halide Perovskite Nanocrystals. *ACS Nano* **2021**, *15* (7), 10775–10981. https://doi.org/10.1021/acsnano.0c08903.

(186) Kim, J. S.; Heo, J.-M.; Park, G.-S.; Woo, S.-J.; Cho, C.; Yun, H. J.; Kim, D.-H.; Park, J.; Lee, S.-C.; Park, S.-H.; Yoon, E.; Greenham, N. C.; Lee, T.-W. Ultra-Bright, Efficient and Stable Perovskite Light-Emitting Diodes. *Nature* **2022**, *611* (7937), 688–694. https://doi.org/10.1038/s41586-022-05304-w.

(187) Kim, T.; Kim, K.-H.; Kim, S.; Choi, S.-M.; Jang, H.; Seo, H.-K.; Lee, H.; Chung, D.-Y.; Jang, E. Efficient and Stable Blue Quantum Dot Light-Emitting Diode. *Nature* **2020**, *586* (7829), 385–389. https://doi.org/10.1038/s41586-020-2791-x.

(188) Liu, J.; Liu, P.; Chen, D.; Shi, T.; Qu, X.; Chen, L.; Wu, T.; Ke, J.; Xiong, K.; Li, M.; Song, H.; Wei, W.; Cao, J.; Zhang, J.; Gao, L.; Tang, J. A Near-Infrared Colloidal Quantum Dot Imager with Monolithically Integrated Readout Circuitry. *Nat Electron* **2022**, *5* (7), 443–451. https://doi.org/10.1038/s41928-022-00779-x.

(189) Liu, J.; Liu, P.; Shi, T.; Ke, M.; Xiong, K.; Liu, Y.; Chen, L.; Zhang, L.; Liang, X.; Li, H.; Lu, S.; Lan, X.; Niu, G.; Zhang, J.; Fei, P.; Gao, L.; Tang, J. Flexible and Broadband Colloidal Quantum Dots Photodiode Array for Pixel-Level X-Ray to near-Infrared Image Fusion. *Nat Commun* **2023**, *14* (1), 5352. https://doi.org/10.1038/s41467-023-40620-3.

(190) Park, Y.-S.; Roh, J.; Diroll, B. T.; Schaller, R. D.; Klimov, V. I. Colloidal Quantum Dot Lasers. *Nat Rev Mater* **2021**, *6* (5), 382–401. https://doi.org/10.1038/s41578-020-00274-9.

(191) Jung, H.; Ahn, N.; Klimov, V. I. Prospects and Challenges of Colloidal Quantum Dot Laser Diodes. *Nat. Photon.* **2021**, *15* (9), 643–655. https://doi.org/10.1038/s41566-021-00827-6.

(192) Taghipour, N.; Dalmases, M.; Whitworth, G. L.; Dosil, M.; Othonos, A.; Christodoulou, S.; Liga, S. M.; Konstantatos, G. Colloidal Quantum Dot Infrared Lasers Featuring Sub-Single-Exciton Threshold and Very High Gain. *Advanced Materials* **2023**, *35* (1), 2207678. https://doi.org/10.1002/adma.202207678.

(193) Whitworth, G. L.; Dalmases, M.; Taghipour, N.; Konstantatos, G. Solution-Processed PbS Quantum Dot Infrared Laser with Room-Temperature Tunable Emission in the Optical Telecommunications Window. *Nat. Photon.* **2021**, *15* (10), 738–742. https://doi.org/10.1038/s41566-021-00878-9.

(194) Nima Taghipour; Guy L. Whitworth; Andreas Othonos; Mariona Dalmases; Santanu Pradhan; Yongjie Wang; Gaurav Kumar; Gerasimos Konstantatos. Low-Threshold Highly Stable Colloidal Quantum Dot Short-Wave Infrared Laser. *Advanced Materials* **2021**.

(195) Christodoulou, S.; Ramiro, I.; Othonos, A.; Figueroba, A.; Dalmases, M.; Özdemir, O.; Pradhan, S.; Itskos, G.; Konstantatos, G. Single-Exciton Gain and Stimulated Emission

Across the Infrared Telecom Band from Robust Heavily Doped PbS Colloidal Quantum Dots. *Nano Lett.* **2020**, *20* (8), 5909–5915. https://doi.org/10.1021/acs.nanolett.0c01859.
(196) Chen, Y.; Ryou, A.; Friedfeld, M. R.; Fryett, T.; Whitehead, J.; Cossairt, B. M.; Majumdar, A. Deterministic Positioning of Colloidal Quantum Dots on Silicon Nitride Nanobeam Cavities. *Nano Lett.* **2018**, *18* (10), 6404–6410. https://doi.org/10.1021/acs.nanolett.8b02764.
(197) Sung, J.; Shin, D.; Cho, H.; Lee, S. W.; Park, S.; Kim, Y. D.; Moon, J. S.; Kim, J.-H.; Gong, S.-H. Room-Temperature Continuous-Wave Indirect-Bandgap Transition Lasing in an Ultra-Thin WS2 Disk. *Nat. Photon.* **2022**. https://doi.org/10.1038/s41566-022-01085-w.
(198) Strauf, S.; Hennessy, K.; Rakher, M. T.; Choi, Y.-S.; Badolato, A.; Andreani, L. C.; Hu, E. L.; Petroff, P. M.; Bouwmeester, D. Self-Tuned Quantum Dot Gain in Photonic Crystal Lasers. *Phys. Rev. Lett.* **2006**, *96* (12), 127404. https://doi.org/10.1103/PhysRevLett.96.127404.
(199) Wu, S.; Buckley, S.; Schaibley, J. R.; Feng, L.; Yan, J.; Mandrus, D. G.; Hatami, F.; Yao, W.; Vučković, J.; Majumdar, A.; Xu, X. Monolayer Semiconductor Nanocavity Lasers with Ultralow Thresholds. *Nature* **2015**, *520* (7545), 69–72. https://doi.org/10.1038/nature14290.
(200) Yang, Z.; Pelton, M.; Fedin, I.; Talapin, D. V.; Waks, E. A Room Temperature Continuous-Wave Nanolaser Using Colloidal Quantum Wells. *Nat Commun* **2017**, *8* (1), 143. https://doi.org/10.1038/s41467-017-00198-z.
(201) Sharp, D.; Kala, A.; Rarick, H.; Nguyen, H. A.; Skytte, E.; Cossairt, B. M.; Majumdar, A. Nanocavity-Enhanced Second-Harmonic Generation from Colossal Quantum Dots. arXiv March 5, 2025. https://doi.org/10.48550/arXiv.2503.03072.
(202) Witzens, J.; Baehr-Jones, T.; Hochberg, M. On-Chip OPOs. *Nature Photon* **2010**, *4* (1), 10–12. https://doi.org/10.1038/nphoton.2009.243.
(203) Riemensberger, J.; Kuznetsov, N.; Liu, J.; He, J.; Wang, R. N.; Kippenberg, T. J. A Photonic Integrated Continuous-Travelling-Wave Parametric Amplifier. *Nature* **2022**, *612* (7938), 56–61. https://doi.org/10.1038/s41586-022-05329-1.
(204) Trivedi, R.; Khankhoje, U. K.; Majumdar, A. Cavity-Enhanced Second-Order Nonlinear Photonic Logic Circuits. *Phys. Rev. Applied* **2016**, *5* (5), 054001. https://doi.org/10.1103/PhysRevApplied.5.054001.
(205) Heinz, T. F.; Chen, C. K.; Ricard, D.; Shen, Y. R. Spectroscopy of Molecular Monolayers by Resonant Second-Harmonic Generation. *Phys. Rev. Lett.* **1982**, *48* (7), 478–481. https://doi.org/10.1103/PhysRevLett.48.478.
(206) Lu, J.; Li, M.; Zou, C.-L.; Al Sayem, A.; Tang, H. X. Toward 1% Single-Photon Anharmonicity with Periodically Poled Lithium Niobate Microring Resonators. *Optica* **2020**, *7* (12), 1654. https://doi.org/10.1364/OPTICA.403931.
(207) Ozawa, A.; Rauschenberger, J.; Gohle, Ch.; Herrmann, M.; Walker, D. R.; Pervak, V.; Fernandez, A.; Graf, R.; Apolonski, A.; Holzwarth, R.; Krausz, F.; Hänsch, T. W.; Udem, Th. High Harmonic Frequency Combs for High Resolution Spectroscopy. *Phys. Rev. Lett.* **2008**, *100* (25), 253901. https://doi.org/10.1103/PhysRevLett.100.253901.
(208) Seyler, K. L.; Schaibley, J. R.; Gong, P.; Rivera, P.; Jones, A. M.; Wu, S.; Yan, J.; Mandrus, D. G.; Yao, W.; Xu, X. Electrical Control of Second-Harmonic Generation in a WSe2 Monolayer Transistor. *Nature Nanotech* **2015**, *10* (5), 407–411. https://doi.org/10.1038/nnano.2015.73.

(209) Laktaev, I. D.; Saidzhonov, B. M.; Vasiliev, R. B.; Smirnov, A. M.; Butov, O. V. Second Harmonic Generation in Colloidal CdSe/CdS Nanoplatelets. *Results in Physics* **2020**, *19*, 103503. https://doi.org/10.1016/j.rinp.2020.103503.
(210) Guymon, G. G.; Sharp, D.; Cohen, T. A.; Gibbs, S. L.; Manna, A.; Tzanetopoulos, E.; Gamelin, D. R.; Majumdar, A.; MacKenzie, J. D. Electrohydrodynamic Printing-Based Heterointegration of Quantum Dots on Suspended Nanophotonic Cavities. *Adv Materials Technologies* **2024**, *9* (10), 2301921. https://doi.org/10.1002/admt.202301921.
(211) Sutherland, R. L. *Handbook of Nonlinear Optics*, 0 ed.; CRC Press, 2003. https://doi.org/10.1201/9780203912539.
(212) Ye, J.; Lynn, T. W. Applications of Optical Cavities in Modern Atomic, Molecular, and Optical Physics. In *Advances In Atomic, Molecular, and Optical Physics*; Elsevier, 2003; Vol. 49, pp 1–83. https://doi.org/10.1016/S1049-250X(03)80003-4.
(213) Fryett, T. K.; Seyler, K. L.; Zheng, J.; Liu, C.-H.; Xu, X.; Majumdar, A. Silicon Photonic Crystal Cavity Enhanced Second-Harmonic Generation from Monolayer WSe $_2$. *2D Mater.* **2016**, *4* (1), 015031. https://doi.org/10.1088/2053-1583/4/1/015031.
(214) Rarick, H.; Kala, A.; Pumulo, S.; Manna, A.; Sharp, D.; Munley, C.; Xu, X.; Majumdar, A. Enhanced Second-Harmonic Generation in a Monolayer Tungsten Diselenide Integrated Silicon Nitride Nanocavity. *ACS Photonics* **2024**, acsphotonics.4c01029. https://doi.org/10.1021/acsphotonics.4c01029.
(215) Day, J. K.; Chung, M.-H.; Lee, Y.-H.; Menon, V. M. Microcavity Enhanced Second Harmonic Generation in 2D MoS_2. *Opt. Mater. Express* **2016**, *6* (7), 2360. https://doi.org/10.1364/OME.6.002360.
(216) Linnenbank, H.; Grynko, Y.; Förstner, J.; Linden, S. Second Harmonic Generation Spectroscopy on Hybrid Plasmonic/Dielectric Nanoantennas. *Light Sci Appl* **2016**, *5* (1), e16013–e16013. https://doi.org/10.1038/lsa.2016.13.
(217) Logan, A. D.; Gould, M.; Schmidgall, E. R.; Hestroffer, K.; Lin, Z.; Jin, W.; Majumdar, A.; Hatami, F.; Rodriguez, A. W.; Fu, K.-M. C. 400%/W Second Harmonic Conversion Efficiency in 14 Mm-Diameter Gallium Phosphide-on-Oxide Resonators. *Opt. Express* **2018**, *26* (26), 33687. https://doi.org/10.1364/OE.26.033687.
(218) Jacobsohn, M.; Banin, U. Size Dependence of Second Harmonic Generation in CdSe Nanocrystal Quantum Dots. *J. Phys. Chem. B* **2000**, *104* (1), 1–5. https://doi.org/10.1021/jp9925076.
(219) Minkov, M.; Gerace, D.; Fan, S. Doubly Resonant $\chi^{(2)}$ Nonlinear Photonic Crystal Cavity Based on a Bound State in the Continuum. *Optica* **2019**, *6* (8), 1039. https://doi.org/10.1364/OPTICA.6.001039.
(220) Sharp, D.; Flower, C.; Jalali Mehrabad, M.; Manna, A.; Rarick, H.; Chen, R.; Hafezi, M.; Majumdar, A. Near-Visible Topological Edge States in a Silicon Nitride Platform. *Opt. Mater. Express* **2024**, *14* (6), 1596. https://doi.org/10.1364/OME.524958.
(221) Hafezi, M.; Mittal, S.; Fan, J.; Migdall, A.; Taylor, J. M. Imaging Topological Edge States in Silicon Photonics. *Nature Photon* **2013**, *7* (12), 1001–1005. https://doi.org/10.1038/nphoton.2013.274.
(222) Saxena, A.; Chen, Y.; Fang, Z.; Majumdar, A. Photonic Topological Baths for Quantum Simulation. *ACS Photonics* **2022**, *9* (2), 682–687. https://doi.org/10.1021/acsphotonics.1c01751.

(223) Choi, J.-H.; Hayenga, W. E.; Liu, Y. G. N.; Parto, M.; Bahari, B.; Christodoulides, D. N.; Khajavikhan, M. Room Temperature Electrically Pumped Topological Insulator Lasers. *Nat Commun* **2021**, *12* (1), 3434. https://doi.org/10.1038/s41467-021-23718-4.
(224) Liu, P.; Zeng, H.; Czaplewski, D. A.; Stern, N. P. Low Index Contrast Valley Hall Topological Photonics for Robust Transport in the Visible Spectrum. *ACS Photonics* **2022**, *9* (3), 922–928. https://doi.org/10.1021/acsphotonics.1c01741.
(225) Liu, W.; Hwang, M.; Ji, Z.; Wang, Y.; Modi, G.; Agarwal, R. Z $_2$ Photonic Topological Insulators in the Visible Wavelength Range for Robust Nanoscale Photonics. *Nano Lett.* **2020**, *20* (2), 1329–1335. https://doi.org/10.1021/acs.nanolett.9b04813.
(226) El Hassan, A.; Kunst, F. K.; Moritz, A.; Andler, G.; Bergholtz, E. J.; Bourennane, M. Corner States of Light in Photonic Waveguides. *Nat. Photonics* **2019**, *13* (10), 697–700. https://doi.org/10.1038/s41566-019-0519-y.
(227) Ritter, R.; Gruhler, N.; Pernice, W. H. P.; Kübler, H.; Pfau, T.; Löw, R. Coupling Thermal Atomic Vapor to an Integrated Ring Resonator. *New J. Phys.* **2016**, *18* (10), 103031. https://doi.org/10.1088/1367-2630/18/10/103031.
(228) Walther, V.; Johne, R.; Pohl, T. Giant Optical Nonlinearities from Rydberg Excitons in Semiconductor Microcavities. *Nat Commun* **2018**, *9* (1), 1309. https://doi.org/10.1038/s41467-018-03742-7.
(229) Nasari, H.; Pyrialakos, G. G.; Christodoulides, D. N.; Khajavikhan, M. Non-Hermitian Topological Photonics. *Opt. Mater. Express* **2023**, *13* (4), 870. https://doi.org/10.1364/OME.483361.
(230) Smirnova, D.; Leykam, D.; Chong, Y.; Kivshar, Y. Nonlinear Topological Photonics. *Applied Physics Reviews* **2020**, *7* (2), 021306. https://doi.org/10.1063/1.5142397.
(231) Jalali Mehrabad, M.; Mittal, S.; Hafezi, M. Topological Photonics: Fundamental Concepts, Recent Developments, and Future Directions. *Phys. Rev. A* **2023**, *108* (4), 040101. https://doi.org/10.1103/PhysRevA.108.040101.
(232) Lee, S. H.; Oh, D. Y.; Yang, Q.-F.; Shen, B.; Wang, H.; Yang, K. Y.; Lai, Y.-H.; Yi, X.; Li, X.; Vahala, K. Towards Visible Soliton Microcomb Generation. *Nat Commun* **2017**, *8* (1), 1295. https://doi.org/10.1038/s41467-017-01473-9.
(233) Roy, A.; Ledezma, L.; Costa, L.; Gray, R.; Sekine, R.; Guo, Q.; Liu, M.; Briggs, R. M.; Marandi, A. Visible-to-Mid-IR Tunable Frequency Comb in Nanophotonics. *Nat Commun* **2023**, *14* (1), 6549. https://doi.org/10.1038/s41467-023-42289-0.
(234) Mittal, S.; Moille, G.; Srinivasan, K.; Chembo, Y. K.; Hafezi, M. Topological Frequency Combs and Nested Temporal Solitons. *Nat. Phys.* **2021**, *17* (10), 1169–1176. https://doi.org/10.1038/s41567-021-01302-3.
(235) Flower, C. J.; Mehrabad, M. J.; Xu, L.; Moille, G.; Suarez-Forero, D. G.; Chembo, Y.; Srinivasan, K.; Mittal, S.; Hafezi, M. Observation of Topological Frequency Combs. arXiv January 27, 2024. http://arxiv.org/abs/2401.15547 (accessed 2024-02-21).
(236) Mittal, S.; Fan, J.; Faez, S.; Migdall, A.; Taylor, J. M.; Hafezi, M. Topologically Robust Transport of Photons in a Synthetic Gauge Field. *Phys. Rev. Lett.* **2014**, *113* (8), 087403. https://doi.org/10.1103/PhysRevLett.113.087403.
(237) Hofstadter, D. R. Energy Levels and Wave Functions of Bloch Electrons in Rational and Irrational Magnetic Fields. *Phys. Rev. B* **1976**, *14* (6), 2239–2249. https://doi.org/10.1103/PhysRevB.14.2239.

(238) Almutlaq, J.; Liu, Y.; Mir, W. J.; Sabatini, R. P.; Englund, D.; Bakr, O. M.; Sargent, E. H. Engineering Colloidal Semiconductor Nanocrystals for Quantum Information Processing. *Nat. Nanotechnol.* **2024**. https://doi.org/10.1038/s41565-024-01606-4.
(239) Hafezi, M.; Demler, E. A.; Lukin, M. D.; Taylor, J. M. Robust Optical Delay Lines with Topological Protection. *Nature Phys* **2011**, *7* (11), 907–912. https://doi.org/10.1038/nphys2063.
(240) Mittal, S.; Goldschmidt, E. A.; Hafezi, M. A Topological Source of Quantum Light. *Nature* **2018**, *561* (7724), 502–506. https://doi.org/10.1038/s41586-018-0478-3.
(241) Marchetti, R.; Lacava, C.; Khokhar, A.; Chen, X.; Cristiani, I.; Richardson, D. J.; Reed, G. T.; Petropoulos, P.; Minzioni, P. High-Efficiency Grating-Couplers: Demonstration of a New Design Strategy. *Sci Rep* **2017**, *7* (1), 16670. https://doi.org/10.1038/s41598-017-16505-z.
(242) Anthur, A. P.; Zhang, H.; Paniagua-Dominguez, R.; Kalashnikov, D. A.; Ha, S. T.; Maß, T. W. W.; Kuznetsov, A. I.; Krivitsky, L. Continuous Wave Second Harmonic Generation Enabled by Quasi-Bound-States in the Continuum on Gallium Phosphide Metasurfaces. *Nano Lett.* **2020**, *20* (12), 8745–8751. https://doi.org/10.1021/acs.nanolett.0c03601.
(243) Csányi, E.; Liu, Y.; Rezaei, S. D.; Lee, H. Y. L.; Tjiptoharsono, F.; Mahfoud, Z.; Gorelik, S.; Zhao, X.; Lim, L. J.; Zhu, D. Engineering Perovskite Emissions via Optical Quasi-Bound-States-in-the-Continuum. *arXiv preprint arXiv:2306.14229* **2023**.
(244) Hsu, C. W.; Zhen, B.; Stone, A. D.; Joannopoulos, J. D.; Soljačić, M. Bound States in the Continuum. *Nat Rev Mater* **2016**, *1* (9), 16048. https://doi.org/10.1038/natrevmats.2016.48.
(245) Abutoama, M.; Christiansen, R. E.; Dubré, A. H.; Xiong, M.; Mørk, J.; Kristensen, P. T. Fabrication and Characterization of Shape- and Topology-Optimized Optical Cavities with Deep Sub-Wavelength Confinement for Interfacing with Colloidal Quantum Dots. 2025. https://doi.org/10.2139/ssrn.5141835.